CUKUROVA UNIVERSITY
INSTITUTE OF NATURAL AND APPLIED SCIENCES

MSc THESIS

Determination of Impact and Flexural Behaviors of Carbon Fiber Reinforced Composites with Various Micro Channel Section Geometry

Oğuzhan TÜRKGENÇ

Mechanical Engineering Department

January, 2026

CUKUROVA UNIVERSITY
INSTITUTE OF NATURAL AND APPLIED SCIENCES

MSc THESIS APPROVAL

Determination of Impact and Flexural Behaviors of Carbon Fiber Reinforced Composites with Various Micro Channel Section Geometry

---

Oğuzhan TÜRKGENÇ

Mechanical Engineering Department

This Master’s Thesis was evaluated by the following Jury Members on 25/12/2025 and was approved by unanimity of votes.

Jury : Prof. Dr. Necdet GEREN (Advisor) …………

: Prof. Dr. Erinç ULUDAMAR …………

: Assoc. Prof. Dr. Çağrı UZAY …………

This Thesis was written in the Department of Mechanical Engineering Institute of Natural and Applied Sciences.

Thesis Number:

Prof. Dr. Sadık DİNÇER
Director
Institute of Natural and Applied Sciences

This work was supported by the Unit of Scientific Research Project Department
Project ID: FYL-2024-16942

CONTENTS

CUKUROVA UNIVERSITY
INSTITUTE OF NATURAL AND APPLIED SCIENCES

MSc THESIS

Determination of Impact and Flexural Behaviors of Carbon Fiber Reinforced Composites with Various Micro Channel Section Geometry

Oğuzhan TÜRKGENÇ

Advisor: Prof. Dr. Necdet GEREN

Department of Mechanical Engineering

ABSTRACT

In this thesis study, the effect of embedded microchannels serving functions such as thermal management, self-healing and damage detection in smart/multi-functional composite applications on the mechanical performance of carbon fiber reinforced polymer (CFRP) laminates has been investigated in terms of channel cross-section geometry. Reference test specimens without channels (NC) were compared with reference test specimens which have circular (CC), square (SC), hexagonal (HC), and star-shaped (StC) channels; behaviour under bending load was evaluated using a three-point bending test according to ASTM D790, while behaviour under impact load was evaluated using a 30 J low-velocity drop weight test according to ASTM D7136. In order to quantitatively relate geometry to the mechanical results, cross-sections of reference specimens were scanned using a coordinate measuring machine (CMM) and modelled in CAD software to calculate section properties. The results indicate that microchannel integration does not completely compromise performance under suitable production conditions; however, the damage initiation threshold and propagation characteristics change significantly as the cross-section becomes angled or complex. In terms of equivalent bending rigidity (S_B), the highest increase compared to the NC (non-channelled) reference sample was observed in the circular-channelled (CC) reference sample (+68.1%). The absence of sharp corners in the circular cross-section limits stress concentrations, ensuring a more homogeneous load transfer and explaining the observed trend. In addition, circular geometry can offer advantages in terms of preserving fiber continuity, as it can cause lower local fiber deviation compared to sharp-edged channel geometries during manufacturing. While peak forces followed a similar pattern in impact tests, the absorbed energy was found to be lower in all channelled groups compared to NC (non-channelled test specimens). However, post-impact visual examinations have shown that the discontinuities created by micro-channels can divert the path of damage propagation, thereby limiting damage propagation in the thickness direction to a certain extent and contributing to the damage remaining more localised.

Keywords: Smart composites, Embedded micro-channels, CFRP composites, Bending test, Impact test

ÇUKUROVA ÜNİVERSİTESİ
FEN BİLİMLERİ ENSTİTÜSÜ

YÜKSEK LİSANS TEZİ

Çeşitli Mikro Kanal Kesit Geometrilerine Sahip Karbon Elyaf Takviyeli Kompozitlerin Darbe ve Eğilme Davranışlarının Belirlenmesi

Oğuzhan TÜRKGENÇ

Danışman: Prof. Dr. Necdet GEREN

Makine Mühendisliği Anabilim Dalı

ÖZ

Bu tez çalışmasında, akıllı/çok işlevli kompozit uygulamalarında termal yönetim, kendi kendini onarma ve hasar algılama gibi işlevlere hizmet eden gömülü mikro-kanalların karbon elyaf takviyeli polimer (KETP) kompozitlerin mekanik performansı üzerindeki etkisi, kanal geometrisi açısından incelenmiştir. Kanal içermeyen (NC) referans test numunesi ile dairesel (CC), kare (SC), altıgen (HC) ve yıldız (StC) formunda kanallara sahip referans test numuneleri karşılaştırılmış; eğilme davranışı ASTM D790'a göre üç nokta eğilme testi, darbe davranışı ise ASTM D7136'ya göre 30 J düşük hızlı ağırlık düşürme testi ile değerlendirilmiştir. Geometrinin mekanik sonuçlarla nicel olarak ilişkilendirilebilmesi için grup davranışını en iyi temsil eden referans numunelere ait kesitler koordinat ölçüm cihazı (CMM) ile taranmış ve CAD ortamında modellenerek kesit özellikleri hesaplanmıştır. Sonuçlar, uygun üretim koşullarında mikro-kanal entegrasyonunun performansı tamamen kayba uğratmadığını; ancak kesitin açılı veya karmaşık hale gelmesiyle hasar başlangıç eşiği ve yayılım karakterinin belirgin biçimde değiştiğini göstermiştir. Eşdeğer eğilme rijitliği (S_B) açısından, NC (kanalsız) referans numuneye kıyasla en yüksek artış dairesel kanallı (CC) referans numunede gözlenmiştir (+%68.1). Dairesel kesitte keskin (açılı) köşelerin bulunmaması, gerilme yığılmalarını sınırlandırarak daha homojen bir yük aktarımı sağlamakta ve gözlenen eğilimi açıklamaktadır. Buna ek olarak dairesel geometri, imalat sırasında keskin köşeli (açılı) kanal geometrilerine kıyasla daha düşük yerel lif sapmasına neden olduğundan, lif sürekliliğinin korunması açısından avantaj sunmaktadır. Darbe testlerinde tepe kuvvetler benzer karakterde seyrederken, soğurulan enerjinin tüm kanallı gruplarda NC'ye (kanalsız test numuneleri) göre daha düşük olduğu görülmüştür. Buna karşın darbe sonrası görsel incelemeler, mikro-kanalların oluşturduğu süreksizliklerin hasar yayılım yolunu saptırarak kalınlık doğrultusundaki hasar yayılımını belirli ölçüde sınırlayabildiğini ve hasarın daha lokal kalmasına katkı sağlayabildiğini göstermiştir.

Anahtar Kelimeler: Akıllı kompozitler, Gömülü mikro kanallar, KETP kompozitler, Eğilme testi, Darbe testi

GENİŞLETİLMİŞ ÖZET

Kompozit malzemeler, yüksek özgül dayanım ve rijitlikleri sayesinde havacılık, otomotiv ve enerji gibi sektörlerde yapısal hafifletme hedeflerine güçlü bir yanıt vermektedir. Bununla birlikte güncel mühendislik beklentileri, kompozitlerden yalnızca yük taşıyan "pasif" elemanlar olmalarını değil; aynı zamanda ısıl yönetim, hasar tespiti ve kendini onarma gibi ek işlevleri de yerine getirebilen "çok fonksiyonlu" sistemlere dönüşmelerini talep etmektedir. Bu amaçla biyolojik damar ağlarından ilham alan gömülü mikro kanal yaklaşımları, kompozit içinde akışkan taşınmasına olanak sağlayarak aktif soğutma veya iyileştirici ajan dolaşımı gibi fonksiyonları mümkün kılmaktadır. Ancak laminat içinde kanal veya boşluk oluşturulması, yerel gerilme dağılımını değiştirerek delaminasyon ve lif kırılması gibi hasar mekanizmalarını tetikleyebilmekte; dolayısıyla kanalın yalnızca varlığı değil, kanal kesit geometrisi de yapısal güvenilirlik açısından kritik hale gelmektedir.

Bu tez çalışmasının amacı; farklı kanal geometrilerine sahip karbon elyaf takviyeli polimer (KETP) kompozitlerin eğilme ve düşük hızlı darbe testleri altında davranışlarını karşılaştırmalı olarak incelemek ve çok fonksiyonlu kompozit tasarımlar için kanal geometrisi seçiminde kullanılabilecek deneysel bir değerlendirme zemini oluşturmaktır. Bu amaçla dairesel (CC), kare (SC), altıgen (HC) ve yıldız (StC) kesitli mikro kanallara sahip numuneler ile kanal içermeyen (NC) referans numuneler aynı malzeme sistemi ve benzer üretim koşulları altında hazırlanarak karşılaştırılmıştır.

Üretim yönteminin seçimi, kanalların laminat içerisine hedeflenen konumda ve istenilen geometrik formda entegre edilebilmesi ve laminat içindeki boşluk oluşumunun kontrol edilebilmesi gereklilikleriyle doğrudan ilişkilidir. Test numuneleri, 400 g/m² twill dokuma karbon elyaf kumaş ve epoksi esaslı matris sistemi kullanılarak üretilmiştir. Kanal geometrisinin kürleme süreci boyunca korunması ve laminat içindeki boşluk oluşumunun kontrol edilebilmesi açısından üretim yöntemi kritik öneme sahiptir. Vakum torbalama ile gerçekleştirilen ön üretimlerde hedeflenen kanal geometrisi yeterli doğrulukta elde edilemediğinden, her kanal geometrisine özel olarak tasarlanan MDF kalıplar kullanılarak sıcak pres yöntemi uygulanmıştır. Kürleme işlemi, 60 °C'de 4 saat süreyle gerçekleştirilmiş ve laminat üzerine yaklaşık 3 bar etkin basınç uygulanmıştır.

Mikro kanalların oluşturulmasında, çıkarılabilir çekirdek (core) yaklaşımı kapsamında PA-6 (poliamid/naylon) monofilamentler kullanılmıştır. Laminasyon sırasında monofilamentler 8. ve 9. elyaf katmanı arasına yerleştirilmiş; kürleme tamamlandıktan sonra yapıdan çekilerek laminat içerisinde hedeflenen kesit geometrisine sahip sürekli yapıda mikro kanallar içeren 10 katmanlı laminatlar elde edilmiştir. Monofilamentlerin sıcaklık dayanımı ve boyutsal kararlılığı kanal formunun korunmasına katkı sağlamış; epoksi ile düşük yüzey etkileşimi ve soğuma sırasında oluşan büzülme farkı ise monofilamentlerin yapıya zarar vermeden uzaklaştırılmasını kolaylaştırmıştır. Geometriler arası karşılaştırılabilirliği artırmak amacıyla kanal kesit alanlarının mümkün olduğunca yakın seçilmesine dikkat edilmiş; tedarik kısıtları nedeniyle yıldız kesitli kanalın diğerlerine göre daha küçük alanlı olabileceği kabul edilmiştir. Üretim aşamasında monofilamentlerin kaymasını ve yer değiştirmesini sınırlandırmak üzere uygun sabitleme ve hizalama şablonları kullanılmış; böylece kanalın laminat içinde hedeflenen konumda ve geometrik formda oluşması amaçlanmıştır.

Kanal geometrisinin etkisini sistematik biçimde değerlendirebilmek amacıyla dört farklı kanal geometrisi seçilmiştir: dairesel (CC), kare (SC), altıgen (HC) ve yıldız (StC) kesitli mikrovasküler kanallar. Bu geometriler, köşe sayısı, köşe keskinliği ve geometrik karmaşıklık düzeyi bakımından farklılaştığı için gerilme yığılması ve hasar başlama eğiliminin geometriye bağlı olarak nasıl değiştiğinin incelenmesine imkân tanımaktadır. Karşılaştırmalı analiz için kanal içermeyen (referans) kompozit numuneler de üretilmiş ve tüm sonuçlar referans numuneler üzerinden normalize edilerek yorumlanmıştır. Böylece aynı malzeme sistemi ve üretim koşulları altında, yalnızca kanal geometrisinin mekanik davranışa etkisi daha net biçimde ortaya konmuştur.

Mekanik davranışın değerlendirilmesinde iki temel yükleme senaryosu kullanılmıştır. İlk aşamada ASTM D790 standardına uygun üç noktalı eğilme testleri uygulanmış ve yük-sehim eğrileri kaydedilmiştir. Bu eğriler üzerinden elastik bölge eğimi (başlangıç rijitliği), eğilme modülleri, eşdeğer eğilme rijitliği (S_B), maksimum yük taşıma kapasitesi ve maksimum yük sonrası davranış karakteri analiz edilmiştir. Elastik bölge eğimi, kanal varlığının ve kanal kesitinin eğilme rijitliği üzerindeki etkisini nicel olarak karşılaştırmak için temel bir parametre olarak kullanılmıştır. İkinci aşamada ASTM D7136 standardı çerçevesinde düşük hızlı ağırlık düşürme testleri gerçekleştirilmiş; darbe sırasında yük-yer değiştirme, yük-zaman ve enerji-zaman verileri kullanılarak tepe kuvvet, soğurulan enerji ve temas süresine ilişkin göstergeler değerlendirilmiştir. Her iki test türü sonrasında numuneler görsel olarak incelenmiş ve hasar mekanizmaları (matris çatlağı, lif hasarı ve delaminasyon gibi) kanal tipine bağlı olarak karşılaştırılmıştır.

Deneysel bulguların kesit geometrisiyle nicel biçimde ilişkilendirilebilmesi amacıyla, seçilen temsili (referans) numunelerin gerçek numune kesitleri koordinat ölçüm makinesi (CMM) ile taranmış ve CAD ortamında modellenmiştir. Kanal geometrisindeki değişim, numunenin etkin kesit özelliklerini ve dolayısıyla eğilme rijitliğini doğrudan etkilediğinden, elde edilen kesit modelleri üzerinden referans test numunelerinin alan atalet momenti (I) hesaplanmış; böylece farklı kanal geometrilerinin eğilme rijitliğine etkisi nicel olarak ortaya konmuştur. Bu veriler, eğilme testlerinden elde edilen eğilme modülleriyle birlikte kullanılarak kanal içermeyen referans laminata göre boyutsuz bir "eğilme şekil faktörü" tanımlanmış ve farklı kanal geometrilrine sahip kesitlerin etkinliği karşılaştırmalı olarak yorumlanmıştır. Böylece yalnızca maksimum yük gibi tekil çıktılar yerine, geometri-temelli bir karşılaştırma metriği ile tasarım odaklı bir değerlendirme yapılmıştır.

Eğilme test sonuçları bütüncül olarak değerlendirildiğinde, gömülü mikro kanalların uygun üretim ve yerleşim koşulları altında mekanik performansı tamamen kayba uğratmadığı; ancak kanal geometrisinin açılı (köşeli) veya karmaşık hale gelmesiyle hasar başlangıç eşiği ve hasar yayılım karakterinin belirgin biçimde değiştiği görülmüştür. Dairesel kesitli kanallar, başlangıç rijitliği ve maksimum yük taşıma kapasitesi bakımından referans laminata en yakın ve en dengeli davranışı sergilemiştir. Eşdeğer eğilme rijitliği (S_B) bakımından kanalsız (NC) referansa göre artışın CC'de %68.1 ile en yüksek düzeyde gerçekleşmesi; SC'de %53.8, HC'de %41.9 ve StC'de %33.7 ile daha sınırlı kalması, kanal geometrisinin rijitlik etkinliğini belirgin biçimde yönlendirdiğini göstermiştir. Dairesel geometride keskin köşe bulunmaması nedeniyle gerilme yığılmalarının sınırlanması ve yük transferinin daha homojen gerçekleşmesi, bu sonucu açıklayan temel etkenler olarak değerlendirilmiştir. Kare ve altıgen kanallı numunelerde, kanal köşelerinde gelişen gerilme yoğunlaşmaları yük-sehim eğrileride lineer-elastik bölgeden daha erken sapmalara ve delaminasyon eğiliminin artmasına neden olmuştur. Yıldız kesitli kanallara sahip numunelerde çoklu ve keskin köşe etkisi belirginleşmiş; buna bağlı olarak rijitlik etkinliği azalmış ve hasar daha erken başlamış, sonuçta eğilme performansının olumsuz etkilendiği gözlenmiştir. Bu gözlemler, kanal alanları benzer düzeylerde olsa dahi, kanalın kesit geometrisinin mekanik davranışı belirgin biçimde yönlendirebildiğini göstermektedir.

Düşük hızlı ağırlık düşürme testleri ASTM D7136 standardına uygun olarak 30 J darbe enerjisinde gerçekleştirilmiş; sonuçlar yük–zaman, enerji–zaman ve yük–yer değiştirme eğrileri üzerinden tepe kuvvet, soğurulan enerji ve toplam yer değiştirme gibi parametreler yardımıyla değerlendirilmiştir. Tüm gruplarda yükün ilk milisaniyelerde hızla artarak tepe değere ulaştığı ve temas süresince azalarak sıfıra yaklaştığı; enerji–zaman eğrilerinin ise temas sonunda numunenin soğurduğu toplam enerjiyi temsil eden bir limit değere yaklaştığı gözlenmiştir. Enerji–zaman eğrileri, açılı (köşeli) geometrilerde hasarın daha erken tetiklenmesine bağlı olarak enerji yutma mekanizmasının farklı bir karakter sergilediğini desteklemiştir. Buna karşın soğurulan enerji değerleri geometriye daha duyarlı olup tüm kanallı gruplarda NC'ye göre daha düşük seviyelerde gerçekleşmiştir (NC > StC ≈ HC > CC > SC); bu durum mikro kanal entegrasyonunun ve kanal geometrisinin darbe altında toplam enerji soğurma kapasitesini etkileyebildiğine işaret etmektedir. Hasar incelemeleri, kanallı numunelerde darbe yüzeyindeki hasar izlerinin benzer seviyelerde olduğunu; ancak karşı yüzlerde hasarın daha sınırlı kaldığını ve kanal geometrisinde belirgin bir bozulma oluşmadığını ortaya koymuştur. Buna karşılık kanal içermeyen referans numunede her iki yüzde daha belirgin hasar izleri görülmüştür. Bu bulgu, literatürde bildirilen sonuçlarla uyumlu olarak, kanalların oluşturduğu süreksizliklerin hasar yayılım yolunu saptırarak veya çatlak uçlarını kısmen körelterek hasarın kalınlık boyunca yayılımını azaltabildiğini düşündürmektedir.

Çalışmanın sonuçları, mikro kanal kesit geometrisinin karbon elyaf takviyeli polimer (KETP) kompozitlerde rijitlik, hasar gelişimi ve delaminasyon eğilimi üzerinde belirleyici olduğunu ortaya koymuştur. Dairesel kesitli kanallar, gerilme yığılmalarını sınırlayarak mekanik performansı en iyi koruyan ve yapısal açıdan daha güvenli seçenek olarak öne çıkmıştır. Buna karşılık açılı (köşeli) kanallarda, keskin geçiş bölgelerinde oluşan yerel gerilme yoğunlaşmaları yük–sehim eğrisinin lineer-elastik bölgeden daha düşük yük-sehim seviyelerinde sapmasına (eğimde erken kırılma/azalma) yol açarak daha erken doğrusal olmayan davranışın başlamasına ve delaminasyon eğiliminin artmasına neden olmuştur. Bununla birlikte bu geometriler, akış/ısı transfer yüzeyini artırma gibi işlevsel avantajlar sağlayabilmekte; ancak yapısal performansın öncelikli olduğu tasarımlarda bu kazanımlar, artan hasar riski ile birlikte değerlendirilmelidir. Çoklu keskin geçişler içeren karmaşık kanal kesitlerinde (örneğin yıldız) ise bu etki daha baskın hale gelmiş; rijitlik etkinliğinin azalması ve hasarın daha erken başlamasıyla birlikte eğilme performansının olumsuz etkilendiği görülmüştür.

ACKNOWLEDGEMENTS

Firstly, I would like to express my sincere gratitude to my supervisor, Prof. Dr. Necdet GEREN, for his valuable guidance, expertise, constructive feedback, and continuous support throughout the preparation of this thesis. Prof. Dr. GEREN's office door and phone were always open to me whenever I needed his advice. His insight and encouragement were invaluable in shaping the direction and quality of this thesis work.

Besides my supervisor, I would like to express my sincere gratitude to Assist. Prof. Dr. Durmuş Can ACER, Research Assistant Orhun Cem GÖKCİLER and Research Assistant Mehmet Burak İBEKÇİ, for their support and helpful discussions. Also, I wish to thank Technician Sefa MERAL for his help in the preparation of the test specimens required in experimental studies.

I would like to express my appreciation to Prof. Dr. Erinç ULUDAMAR and Assoc. Prof. Dr. Çağrı UZAY as the jury members of my thesis.

In addition, I would like to thank Unit of Scientific Research Projects Department (BAP) for their financial support.

Finally, I am deeply grateful to my family for their unwavering support throughout my education. Their patience, understanding and encouragement during each stage of this thesis were invaluable, and their moral support played a significant role in bringing this work to completion.

LIST OF TABLES

LIST OF FIGURES

1. INTRODUCTION

1.1. General Overview to Composites

There is no single, universally accepted definition of composite materials, and definitions found in the literature different from each other. However, it is widely accepted that composites consist of at least two distinct phases. Basically, composite materials can be defined as artificially produced materials created by combining two or more constituents at the macroscopic level in such a way that each component retains its own identity, while their combined properties meet specific performance requirements. Typically, they consist of a relatively weak matrix phase reinforced with a dispersed strengthening phase. The reinforcement and matrix do not merge at the atomic level; instead, they remain distinct and inert with respect to each other, allowing the individual constituents to be identified under microscopic examination(Sönmez & Şatır, 2009). Although composites exhibit homogeneous behaviour on a macroscopic scale, they are microscopically heterogeneous, which distinguishes them from alloys.

Reinforcements used in composites may have different structural properties, and their primary role is to carry the applied loads and improve the stiffness and strength of the matrix. The matrix, in turn, serves to protect the usually brittle reinforcement elements from external and environmental influences, transfer applied loads to the reinforcement phase, and hold the entire composite structure together.

1.1.1. Brief History of Composites

Nature has been producing composites for millions of years, and therefore the history of composites is perhaps as old as life on earth itself. Most plant parts have embedded fiber structures for improved mechanical properties. However, composites have only been produced by humans for the last 2,000 years. Since ancient times, people have attempted to strengthen brittle materials by adding fibers of animal or plant origin. The most common and oldest known example of this is adobe brick. Straw and straw mixed with mud gave this material strength and allowed humans to build strong shelters. Japanese samurai produced swords using laminated metals in the fifteenth century. War technologies have always been places where new materials are frequently used. To overcome the problem of bows breaking after a certain force, common in standard western bows, the mongols eliminated this problem by using animal tendons with different fiber orientations in the flexing sections of the bow (Hull, 1998). An ancient example of the use of composites can be given from Egypt. Amphorae of varying colors and thicknesses from the 1st Dynasty reveal that thin glass fibers were being produced in Egypt as early as 1600 BC (H. Y. Ersoy, 2001).

Although composite materials have been used for various purposes since ancient times, the widespread use of what are now called modern composites can be attributed to the coincidental discovery of fiberglass in 1930 by an engineer working at Owens Corning, and its subsequent sale in the United States in 1937. Initially produced by extruding molten glass, these fiberglass fibers were used as insulation, but their use in structural products was not long in coming. The development of the fiberglass production process led to the development of composites during World War II. The combination of fiberglass and plastics led to the creation of an incredibly strong material called FRP. In its early stages of development, this material was used in the construction of aircraft radomes. Military applications of polymer matrix composites (PMCs) during World War II led to large-scale commercial use after the war, particularly in the marine industry, in the late 1940s and early 1950s. The first commercial boat hull was introduced in 1946. Rapid growth in composite science and technology occurred in the United States and Europe during the 1950s. The composites industry began to mature in the 1970s. During this period, DuPont introduced aramid fiber, known as Kevlar. Carbon fiber production also began during this period. Many high-performance composites were produced with these fibers. Composite materials have proven themselves as workable engineering materials and are now quite common, especially in structural applications. They have gained widespread acceptance, and composite materials are replacing traditional materials wherever possible. Today, the aircraft, automobile, marine, sports, electronics, chemical, and medical industries are highly dependent on FRPs. Today, composite technology is constantly evolving with the development of nanoreinforcements, new matrix materials, manufacturing methods, design software, and more. Energy conservation is a major concern in today's world. The operating efficiency of any machine can be increased by using lightweight materials. Wind energy is currently one of the primary energy sources in many countries. Giant windmill blades are manufactured from polymer composites. There's no doubt that composites will continue to play a significant role in energy conservation/production in the modern world.

1.1.2. Classifications of The Composites

In order to better understand the properties, advantages and disadvantages, production methods and usage areas of composites, it may be necessary to classify them under certain headings. Composite materials can be systematically classified according to the characteristics of the reinforcement phase, including its shape (fibers, whiskers, or particles), size (continuous or short), orientation (unidirectional, bidirectional, multidirectional, or random), distribution within the matrix (William D. Callister, 2018) (Figure 1.1.) and the type of the matrix. This classification provides a background for understanding how different reinforcement types and their placement and orientation within the matrix directly influence the overall mechanical, thermal, and physical properties of the composite.

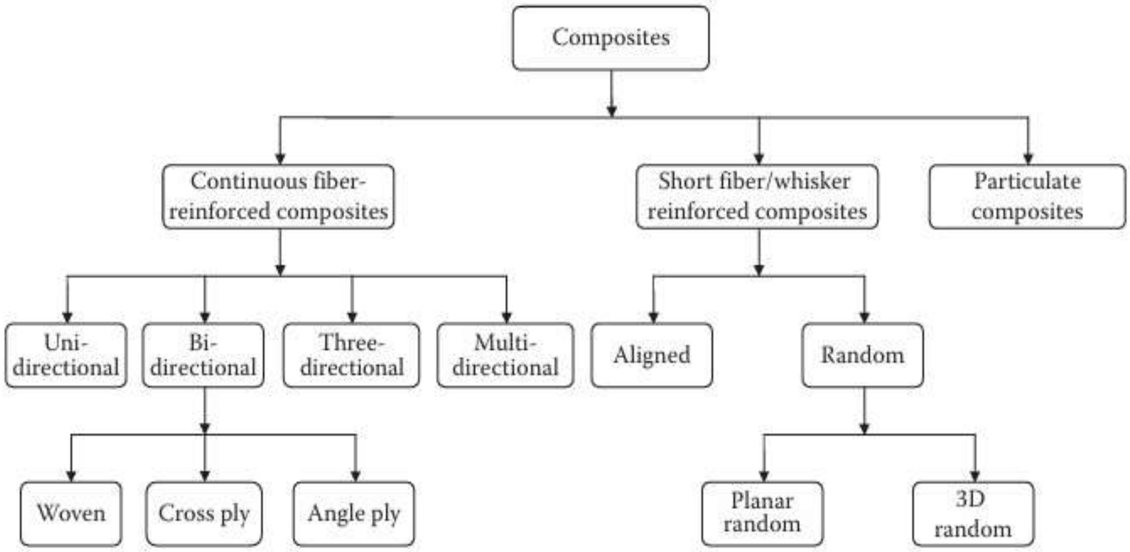

Figure 1.1. Classification of composites based on dispersed phase (William D. Callister, 2018)

Based on Reinforcement Form

Reinforcements are typically categorized as fibers**,** whiskers**,** or particulates, each serving different structural functions (Fig. 1.1). Fiber-reinforced composites (FRCs) are the most significant category due to their superior specific strength and stiffness. In such systems, fibers carry most of the applied load, while the matrix provides cohesion, transfers stresses, and protects the fibers from environmental effects. The overall performance depends on the fiber orientation, volume fraction, and interfacial bonding quality.

Also;

- Continuous fibers offer maximum strength along one direction but cause anisotropy.
- Discontinuous or randomly oriented fibers lead to more isotropic behavior but lower strength (Balasubramanian, 2014).

Whisker and particle-reinforced composites are generally used to increase wear resistance, dimensional stability, and thermal resistance rather than achieve high tensile strength. Also, it should be known that the reinforcement efficiency goes down from continuous fiber to particle for tensile modulus (Figure 1.2). Whiskers theoretically offer very high strength due to their perfect crystal structure, but their use is limited due to production costs and orientation difficulties. Particulate reinforcements such as SiC and Al_2O_3, on the other hand, are dispersed in the matrix as uniformly sized particles and improve the material's hardness, wear resistance, and thermal stability. However, their contribution to load-carrying capacity is low.

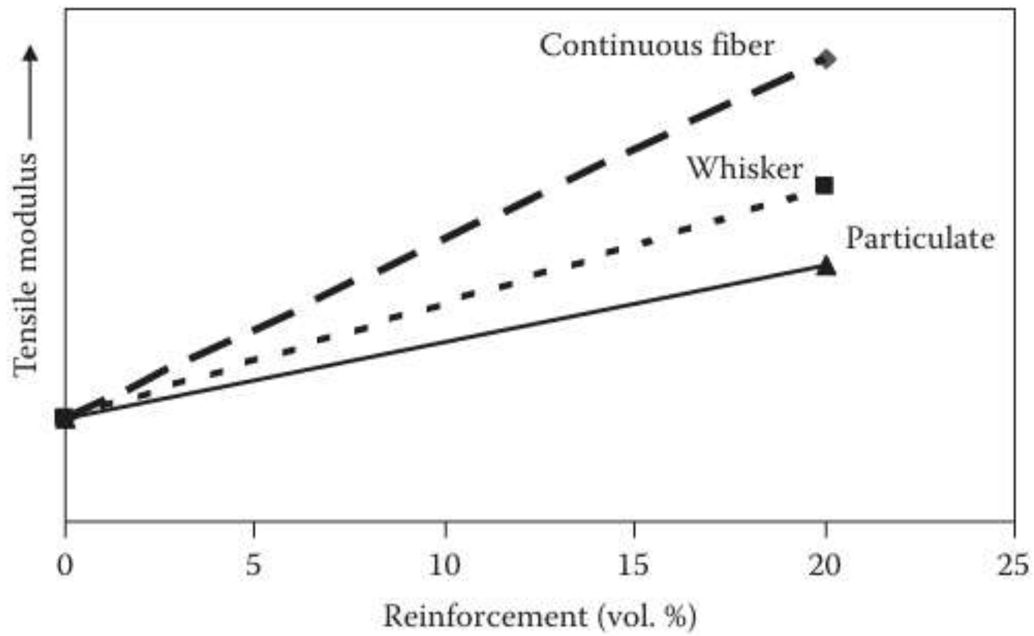

Figure 1.2. Tensile modulus as a function of reinforcement volume fraction for continuous fiber, whisker, and particulate-reinforced composites (Balasubramanian, 2014)

Based on Matrix Type

Composites can also be classified based on the type of matrix material, which strongly influences their thermal stability, density, and manufacturing method (Ikhmayies, 2024). In general, they are grouped into three main categories: polymer, metal, and ceramic matrix composites. Each type offers distinct processing characteristics and performance advantages depending on the intended application.

The matrix phase plays a crucial role in determining not only the mechanical behavior but also the processing conditions of the composite system. During fabrication, the matrix may undergo chemical or physical transformations such as curing, melting, or sintering, depending on its material type. Consequently, the manufacturing method is largely dictated by the matrix: polymers are commonly processed through curing or melt techniques, metals through casting or powder metallurgy, and ceramics via high-temperature sintering.

Briefly, in composite materials, the matrix phase plays a crucial role in determining the service temperature range, the chemical resistance and production method. The primary types of matrix systems are categorized and summarized in the Table 1.1 below.

Table 1.1. Type of matrix, working conditions and application areas

Matrix Type	Abbreviation	Key Advantages	Key Disadvantages and Application Fields	Applications
Polymer Matrix Composites	PMC (FRPs)	Low density, easy processing, high corrosion resistance.	Lower thermal resistance and rigidity (Comparatively). (**Focus of the Thesis**)	Aerospace, automotive, sports
Metal Matrix Composites	MMC	High-temperature resistance, high toughness, good electrical conductivity.	High density, high manufacturing cost.	Defense, engines, brake rotors
Ceramic Matrix Composites	CMC	Very high temperature and wear resistance, high rigidity.	Low toughness, difficult processability, and high cost.	Turbines, armor, space systems

In summary, the classification of composite materials reflects the main concept behind their design. This concept is based on combining strong reinforcements with tough and flexible matrices to achieve a balance between strength, stiffness, and durability. Of all types, fiber-reinforced polymer composites (FRPs) are the most common and the focus of this thesis because they offer high mechanical performance, low weight, and ease of fabrication. Also, understanding how the reinforcement and matrix work together is crucial for the development of smart composite systems, including microchanneled structures that can offer additional functions such as enhanced thermal control.

1.1.3. Production Methods of Composite Materials

Each material varies in terms of its chemical, physical, and mechanical properties, as well as manufacturability. Therefore, when transforming a material into a product, it is necessary to select production methods appropriate to its properties. A production technique suitable for one material may not be suitable for another. Because composite materials are formed by combining two or more different materials, their production methods differ from those of other types of materials. For example, while metals are suitable for machining, composite materials are generally not suitable for this method due to the risk of damage to their reinforcement elements (Scwartz, 1997). Furthermore, since composite materials are subdivided into metal, polymer, and ceramic matrix materials, the production techniques for each group also differ.

Production Methods of Metal Matrix Composites

The production methods of metal-matrix composites can be broadly categorized into two main groups: liquid-phase and solid-phase techniques. In liquid-phase methods, ceramic particles are generally incorporated into a metal matrix using various techniques. The wettability and physical properties of the ceramic material selected as reinforcement are crucial in the production of such composites. Because many ceramic reinforcement materials cannot be adequately wetted by the metal melt, they undergo specific pretreatments prior to production. Commonly used methods in the manufacture of metal-matrix composites include liquid metal impregnation, stir casting (or forge casting), pressure infiltration, liquid metal mixing, semi-solid mixing, plasma spraying, powder metallurgy, and hot pressing (H. Y. Ersoy, 2001; Şahin, 2000).

Production Methods of Ceramic Matrix Composites

Polymers reinforced with reinforcement elements are widely used as composite materials. However, due to their hydrocarbon-based nature, these materials are not suitable for use at high temperatures. Metal-matrix composites are generally preferred over polymer-matrix composites in applications requiring high temperatures, while ceramic-matrix composites offer a strong alternative to metal-matrix composites due to their light weight and high oxidation resistance.

While ceramic materials possess high hardness and modulus of elasticity, they exhibit limiting properties such as low toughness, high brittleness, and low elongation at break. Furthermore, despite their ability to operate at high temperatures, they are susceptible to thermal shock.

In ceramics, which can be reinforced with continuous or discontinuous reinforcement elements, the type of reinforcement not only determines the material's mechanical properties but also determines the choice of production methods. The methods commonly used in the production of ceramic matrix composites include melt (tape) casting, molten-matrix hot pressing, injection molding, chemical vapor deposition (CVD) and infiltration, powder metallurgy, and chemical reaction bonding.

Production Methods of Polymer Matrix Composites

The production of polymer matrix composites is based on the principle of mixing reinforcement elements with the matrix material using appropriate techniques and curing and hardening the polymer-based matrix under specific temperature and pressure conditions. The quality of the final product depends on the accurate control of pressure, temperature, and time parameters during the polymerization process. Furthermore, as with metal matrix composites, the adequate wetting of the reinforcement by the matrix and the homogeneous distribution of the reinforcement elements within the matrix are important factors directly affecting production quality.

Production methods for polymer matrix composites are generally divided into two main groups: open molding and closed molding. While hand lay-up and spraying methods are among the most commonly used open molding techniques, press molding, transfer molding, resin infusion, vacuum molding, autoclave method, filament winding, pultrusion, centrifugal method, resin injection, and reaction injection molding are frequently preferred among closed molding techniques (Biron, 2007; H. Y. Ersoy, 2001; Scwartz, 1997).

Various methods which mentioned like above are available for composite material manufacturing. Initially, the vacuum bagging method was attempted due to its low cost and relatively easy applicability in this study. However, the initial samples produced by this method demonstrated difficulties, specifically the inability to achieve the required precision in the microchannel geometries (Figure 1.3) and insufficient surface quality for reliable structural testing. Consequently, it was determined that the hot press molding technique would be more appropriate for this study. This method was ultimately selected for its capability to achieve a high fiber volume fraction, low void content, and, critically, more accurate control over the embedded microchannel geometry through the use of specially designed molds. This method allows for the production of composites with high structural integrity and precise dimensions by pressing pre-arranged carbon fiber fabrics and different channel templates under controlled temperature and pressure conditions. The resulting high density and homogeneity ensure that the Carbon Fiber Reinforced Polymer (CFRP) specimens which have various microchannel cross-section geometries, possess the high structural integrity required for reliable impact and flexural testing. Images of the samples produced using hot pressing are presented in Section 3.

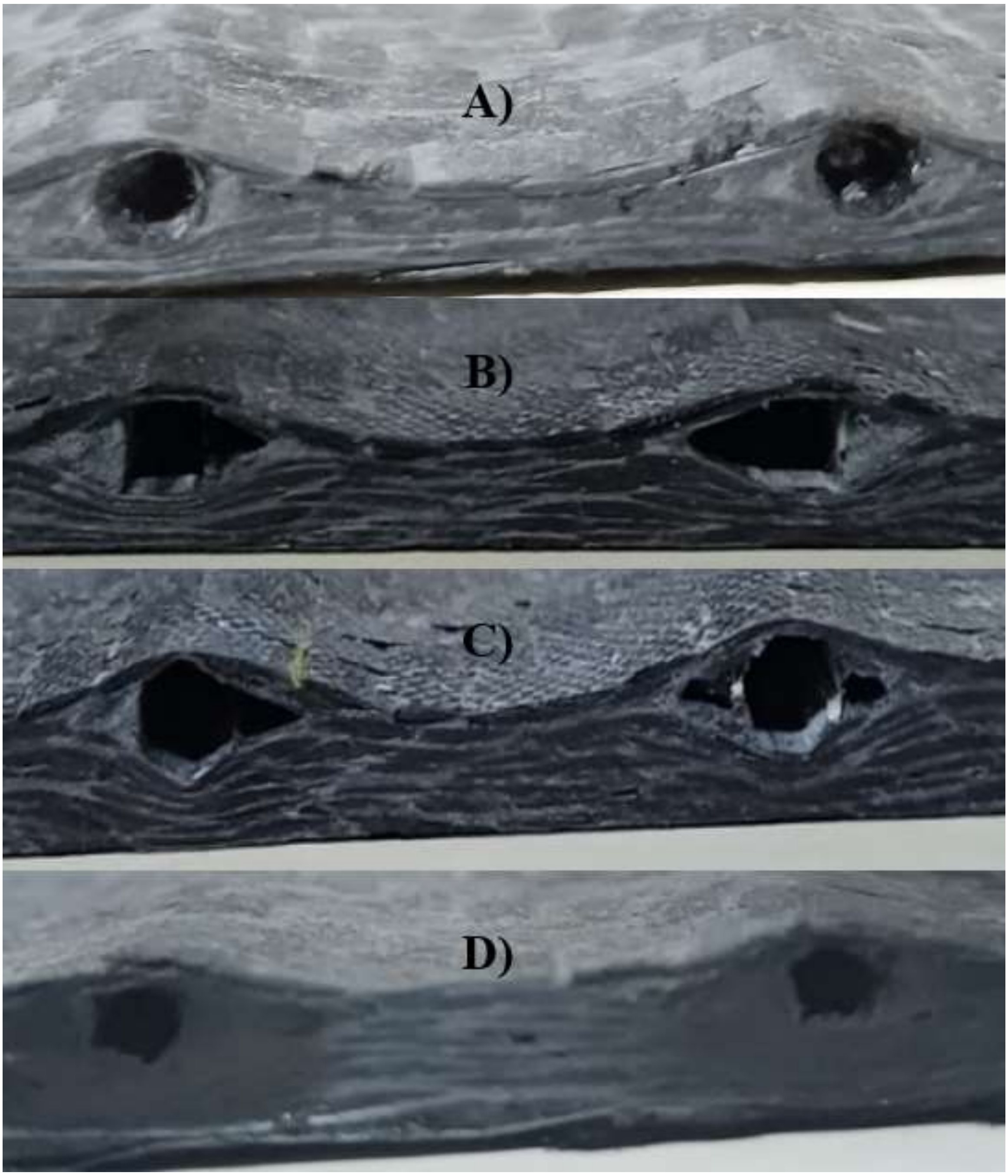

Figure 1.3. Cross-sectional images of pre-samples produced by vacuum bagging; microchannel voids, geometric deviations and observed void formations: (A) Circular channelled sample, (B) Square channelled sample, (C) Hexagonal channelled sample, (D) Star channelled sample

1.1.4. Advantages of Composites

The advantages of composite materials, particularly fiber-reinforced composites (FRCs), are clearly visible in their specific strength and stiffness values compared to traditional engineering materials. As shown in Figure 1.4, carbon fiber-reinforced polymers (CFRPs) and glass fiber-reinforced polymers (GFRPs) exhibit significantly higher specific strength and stiffness compared to metals such as aluminum, titanium, and steel. This demonstrates that composites provide superior load-carrying capacity at significantly lower weight, a critical advantage in weight-sensitive applications such as aerospace and automotive engineering. Furthermore, the mechanical performance of composites can be tuned by adjusting the fiber orientation (unidirectional or quasi-isotropic) and fiber volume fraction, providing considerable flexibility in material design.

The Ashby diagram in Figure 1.5 further emphasizes the superior position of composites among material classes. While polymers, metals, and ceramics are limited to specific regions by inherent limitations such as low strength in polymers, high density in metals, or brittleness in ceramics, composites possess a unique blend of high stiffness, high strength, and low density. This exceptional balance of properties allows composites to achieve a much higher performance-to-weight ratio, resulting in improved energy efficiency and reduced fuel consumption in structural applications. As a result, composites not only surpass traditional materials in mechanical performance but also offer additional advantages such as design compatibility and environmental efficiency, making them indispensable in modern engineering applications.

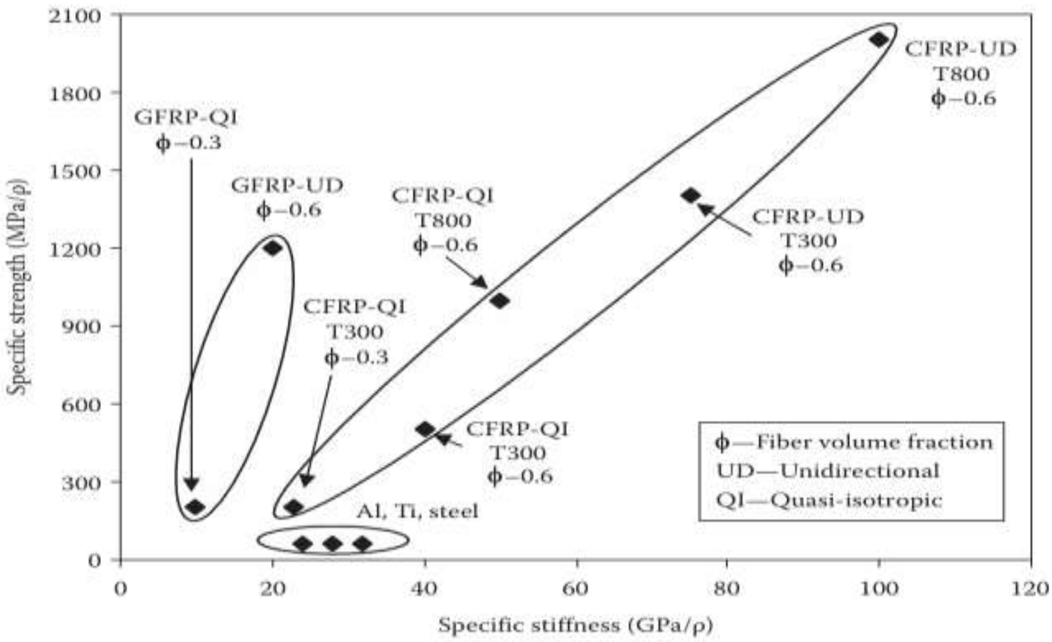

Figure 1.4. Specific strength and stiffness values of conventional materials and composites (Balasubramanian, 2014)

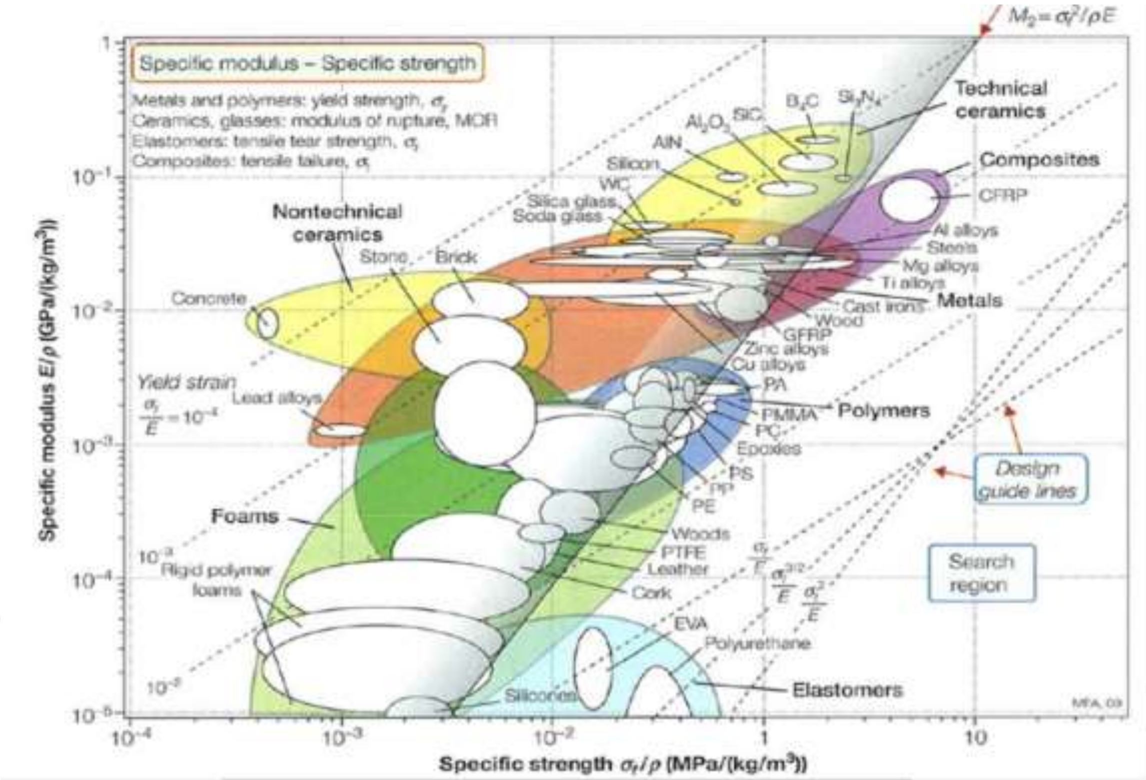

Figure 1.5. Ashby’s material selection diagram (Ashby, 1997)

Composite materials are generally designed and manufactured for applications requiring high performance, lightweight design, high thermal resistance, and corrosion resistance. In such cases, they offer advantages over conventional engineering materials, as seen in Figure 1.5. However, recently, composite materials have become preferred materials in architectural and industrial design, not only for their visual appeal, but also for their high surface quality, visual appeal, and growing popularity. Generally, the main advantages of composite materials can be listed as shown in Table 1.2.

Table 1.2. Advantages of the composite materials

No	Advantage	Description
1	Replacement for Metals	Due to their superior physical and mechanical properties, composites can replace many metals in various applications.
2	High Flexural and Tensile Strength	Some composites provide the same flexural strength as steel or aluminum but are much lighter; for example, up to 5 times lighter than steel and 2 times lighter than aluminum.
3	Excellent Fatigue Resistance	Carbon/epoxy composites can achieve up to 40% better fatigue resistance compared to metals.
4	Corrosion Resistance or Environmental Resistance	Unlike metals, polymer and ceramic matrix composites resist to weathering, chemicals, and atmospheric effects, making them ideal for marine, storage, and aerospace applications.
5	Heat Resistance	When composed of low thermal conductivity constituents, composites can withstand high temperatures; ceramic matrix composites are especially suitable.
6	Design Flexibility	They allow both of the fabrication of complex parts in a single piece without the need for riveting or welding and lightweight and efficient designs.
7	High Impact Resistance	Carbon and glass fiber composites provide higher impact resistance than metals, widely used in defense applications.
8	Vibration and Noise Damping	Composites absorb vibrations better than metals, reduce crack propagation.
9	Low Production Cost	They require lower temperatures and pressures during manufacturing, leading to reduced investment and production costs while maintaining competitiveness in the market.

For composite materials to be superior to other materials, the materials within them must adhere very well to each other. This adhesion depends on how well the base material (matrix) can wet the other materials. Furthermore, the compatibility of the base material and the reinforcing material, the method of production, and the even distribution of the reinforcing material within the composite are also important (H. Ersoy & Malzeme, 2001).

1.1.5. Disadvantages of The Composites

While composite materials appear to possess many advantages over conventional materials, as listed above, they have not experienced the rapid development and widespread use of other materials due to some significant disadvantages. The major disadvantages of composite materials can be listed as shown in Table 1.3.

Table 1.3. Disadvantages of the composite materials

No	Disadvantage	Description
1	Anisotropy	Mechanical properties vary depending on the direction of measurement.
2	Fatigue Sensitivity	Air voids and microcracks negatively affect fatigue performance.
3	High Material Cost	Due to multi-constituent structures and limited production volumes, raw materials are expensive.
4	Manufacturing Challenges	Production methods are complex and machining quality can be difficult to maintain.
5	Thermal and Chemical Limitations	Thermal and chemical resistance depend on the matrix material properties.
6	Moisture Absorption	Some composites absorb moisture, leading to dimensional instability.
7	Brittleness and Impact Sensitivity	Due to their brittle nature, sudden failures may occur and repairs are difficult.
8	Poor Recyclability	Composites are less recyclable compared to metals, creating sustainability challenges.

1.1.6. Application Areas Of The Advanced Composites Materials

Due to the advantages outlined in section 1.4, the use of composite materials has expanded since the mid-20th century, replacing traditional engineering materials in many sectors (especially in applications requiring high strength-to-weight ratios). The sectors where this proliferation is showed in Figure 1.6 in detail. Each of these sectors has utilized the superior properties of composites in different ways to solve engineering problems in their respective fields. These solutions contribute to the expansion of their applications. The areas where composites are most commonly used can be summarized as follows:

- Aerospace.
- Civil/Structural Engineering.
- Automotive Engineering.
- Electrical Engineering.
- Marine Engineering.

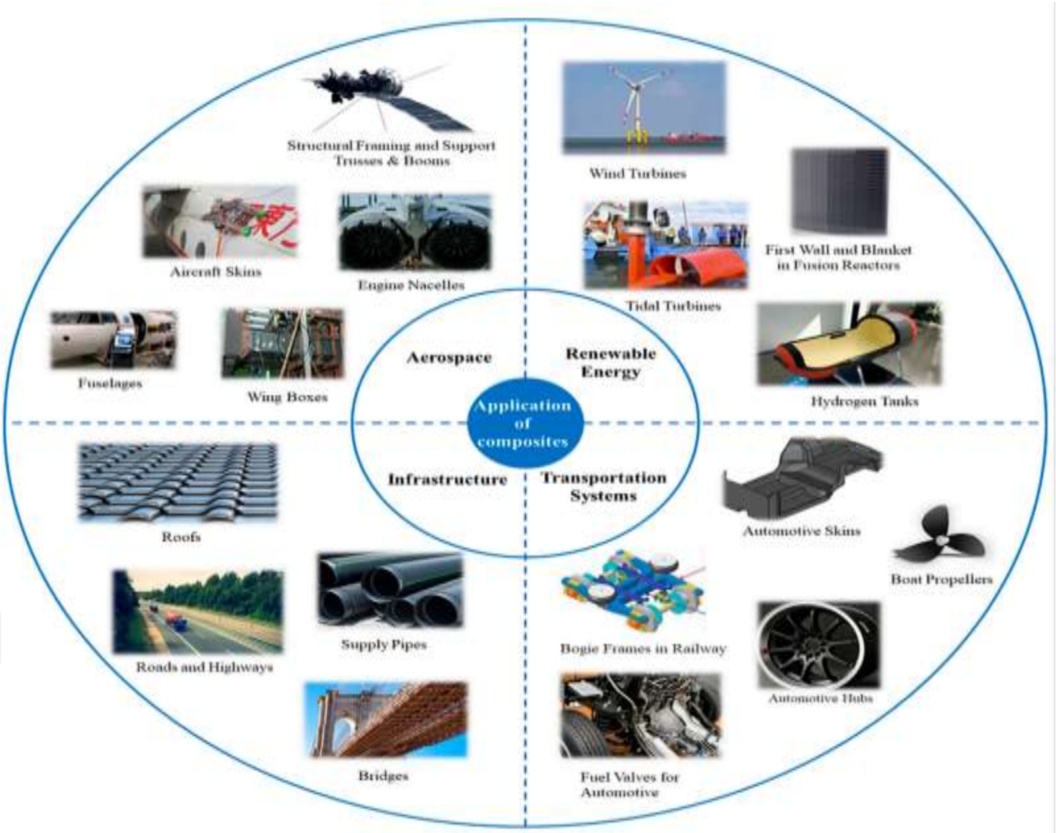

Figure 1.6. Application areas of the composites (Chen, Yu, & Jin, 2022)

Composite materials are increasingly being used in the automotive and transportation sectors, primarily because their lightweight structure contributes to increased fuel efficiency by reducing overall vehicle mass. Thanks to their lightweight and high-strength properties, composite materials directly contribute to reducing vehicle weight, improving fuel economy, and saving energy (Froes, 1994). Weight savings, particularly in the vehicle's core structure, allow for the use of smaller engines, resulting in secondary fuel efficiency (Bhong et al., 2023). The ability to manufacture glass fiber-polyester epoxy composites, particularly outside the United States, allowed the way for their use in the production of vehicles such as disabled tricycles, taxis, delivery trucks, sports cars, ambulances, caravans, and mobile shops. Additionally, glass fiber-reinforced plastics (GRP) are widely used in the motorcycle and scooter industries, where light weight, weather resistance, and aerodynamic performance are important for body components.

Boron-reinforced epoxy composites, firstly used in the tail structures of the US F-15 and F-14 fighter jets, have become one of the pioneering applications in aviation (Quilter, 2001). With technological advances, fiber-reinforced polymer (FRP) composites have become increasingly popular in spacecraft and aircraft production (Mangalgiri, 1999). A significant increase in the use of composite materials, particularly in fuselage and wing structures, has been observed (Elaldi, 2005). Today, resin-impregnated paper or metal honeycomb cores, fiberglass, Kevlar, and high-strength carbon fiber composites are widely preferred in many civil and military aircraft. These materials are used in many areas, including bulkheads, fuselages, helicopter rotor blades, pressure vessels, wing spars, seat components, spoilers, propellers, tailplanes, access panels, fuel tanks, air ducts, external tanks, nose and landing gear covers, floors, fairings, structural elements, and engine covers (Figure 1.7). Carbon fiber-reinforced carbon composites also stand out in applications requiring high temperatures (Niu & CHUN, 1988). In addition, reinforced plastics play a critical role in the defense industry and are used particularly in rocket launchers and rocket motor bodies.

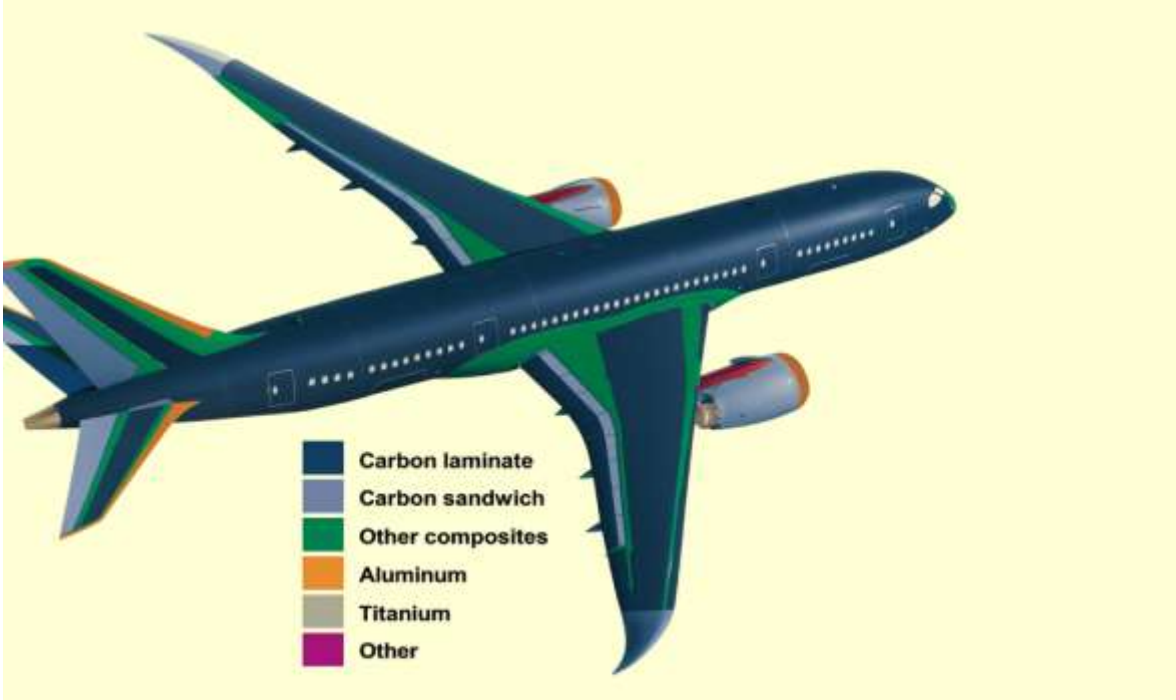

Figure 1.7. Locations of the various material types used in the Boeing 787 Dreamliner (William D. Callister, 2018)

Fiber-reinforced polymer composites are gaining increasing importance in civil engineering due to their properties such as high strength-to-weight and stiffness-to-weight ratios, corrosion resistance, light weight, and long durability (Karbhari, 2007; Van Den Einde, Zhao, & Seible, 2003). These materials are particularly preferred in infrastructure applications when used in combination with suitable fillers in the polymer resin matrix. Engineering termoplastics (ETP) composites are used in various areas, such as strengthening slabs, beams, and walls with externally bonded reinforcement, manufacturing of reinforcing bars and tendons, developing hybrid and fully composite structural systems, and encapsulating columns to increase their earthquake resistance and creating composite bridge decks (Nanni, 1993; Saadatmanesh, 1994). However, over the last three decades, glass fiber reinforced polymer (GFRP) materials have also become widespread in the production of load-bearing structural elements and are found in a wide variety of engineering structures such as modular roof cooling towers, curved roofs, power transmission towers, bridge decks, marine structures, chemical plants, offshore platforms, roadside safety barriers, lighting poles and industrial access platforms (Bakis et al., 2002; Barbero & GangaRao, 2005).

1.2. Failure of the Composites

Composite materials offer distinct advantages over traditional engineering materials due to their excellent specific strength, lightness, and superior fatigue resistance. However, unlike metals, the damage mechanisms of composites are quite complex due to their anisotropic and heterogeneous structures (Soutis, 2005). Composites typically exhibit progressive damage mechanisms rather than yielding and permanent plastic deformation. These mechanisms are characterised by the progression of micro-level defects such as fiber breakage, matrix cracking, fiber-matrix separation, and interlaminar delamination (Clyne & Hull, 2019). Therefore, understanding the micro-mechanisms of these damage modes is crucial for the reliable design and structural integrity of composite components. The primary damage modes that dominate under impact and bending loads, which are the focus of this study, are detailed below.

1.2.1. Matrix Cracking

Matrix cracking is the first type of damage to occur in composites. It is mostly caused by low-speed impact events, tension, compression or shear loads. Immediately after impact events, matrix cracking usually begins as barely visible impact damage (BVID). Matrix cracking progresses, reducing the compressive strength of the composite and the interlaminar shear strength, thereby creating a pathway for more severe damage modes to develop.

1.2.2. Fiber-Matrix Debonding

Fiber-matrix separation (debonding) is a micro-level failure that occurs at the interface between the fiber and the matrix where load transfer takes place (Livingston & Koohbor, 2022). This separation significantly impedes the transfer of loads from the fibers to the matrix. Fiber-matrix separation serves as the initial mechanism for larger damage modes such as matrix cracking and delamination, and rapidly reduces the overall stiffness of the material.

1.2.3. Delamination

Delamination is one of the most critical damage modes in composite laminates. It is the failure of the adhesive bond between adjacent layers (laminates) with different fiber orientations. Matrix cracks, bending and shear stresses are the primary causes of delamination (Vieille, Casado, & Bouvet, 2013). Delamination significantly affects the compressive strength of composite laminates, particularly after impact, and can lead to a rapid loss of structural integrity (buckling). During low or high speed impact events, delamination plays a central role in the propagation of damage.

1.2.4. Fiber Breakage

When a composite is bent, some of the fibers on the surface are subjected to excessive tension, while others are subjected to excessive compression. Fiber breakage is the final damage mode that typically occurs on the tensile side of the specimen. When the tensile strength is exceeded, the fibers break (Safri, Sultan, & Jawaid, 2019). However, in high-energy impacts, the fibers where immediately below the point of impact are subjected to sudden stress. This not only causes matrix cracks and delamination, but also leads to the breaking of fibers that directly absorb impact energy. The broken fibers consume a large portion of the impact energy.

As a summary. understanding and investigation of these critical failure modes is fundamental to the design of new composite architectures. While incorporating embedded microchannels into composite structures offers advantages in functionality (such as thermal management and self healing), it also has the potential to further complicate local stress distribution and initiate new failure pathways. Therefore, evaluating how various microchannel geometries affect these failure modes (specifically, delamination and fiber fracture) under impact and bending loads is a primary focus of this study to ensure the structural reliability of multifunctional Carbon Fiber Reinforced Polymer (CFRP) systems.

1.3. Transition to Smart and Functional Composites

Traditional composites were developed to provide structural advantages such as high strength and low weight. Today, with the increasing complexity of operational conditions and the increasing functional requirements of materials, the concept of not only high mechanical strength and light weight but also multifunctionality has become prominent in the development of composite materials. While traditional composites were designed as passive load-bearing structures, modern engineering practices now aim for smart composite systems that can perform active tasks. This has led to the emergence of a new class of "smart" or "functional" composites. In addition to their structural functions, these materials incorporate additional functions such as sensor capabilities, self-healing, and thermal management (Chung, 2002).

One of the most common approaches to achieving these functional properties is to create a network of vessel-like microchannels, inspired by the vascular structures in biological systems, embedded within the material. These microchannels allow the flow of liquid or gas, enabling functions such as heat transfer, chemical transport, or repair fluid circulation within the material. Thus, the composite structure becomes an active system rather than only a load-bearing element. Microchannels first appeared in the literature in the early 2000s with the "self-healing" approach, which aimed to repair damage within the material. However, over time, it was realized that these vessel-like structures could be used not only for self-healing but also for active functions such as thermal management. Carbon fiber-reinforced polymer composites (CFRP), in particular, experience problems such as reduced mechanical strength and interlayer separation (delamination) at high temperatures, creating the need for effective temperature control in these materials. For this purpose, the idea of circulating coolant through microchannels to remove heat from the material was emerged. Thus, composite structures have become intelligent thermal management systems with active cooling capabilities.

When we look at the using area of the thermal management system on the carbon fiber reinforced composites one of them more remarkable than other areas. The increase in articles on 7battery thermal management systems is particularly noticeable. Figure 1.8 shows that annual distribution of battery thermal management systems publications from 2000 to 2022.

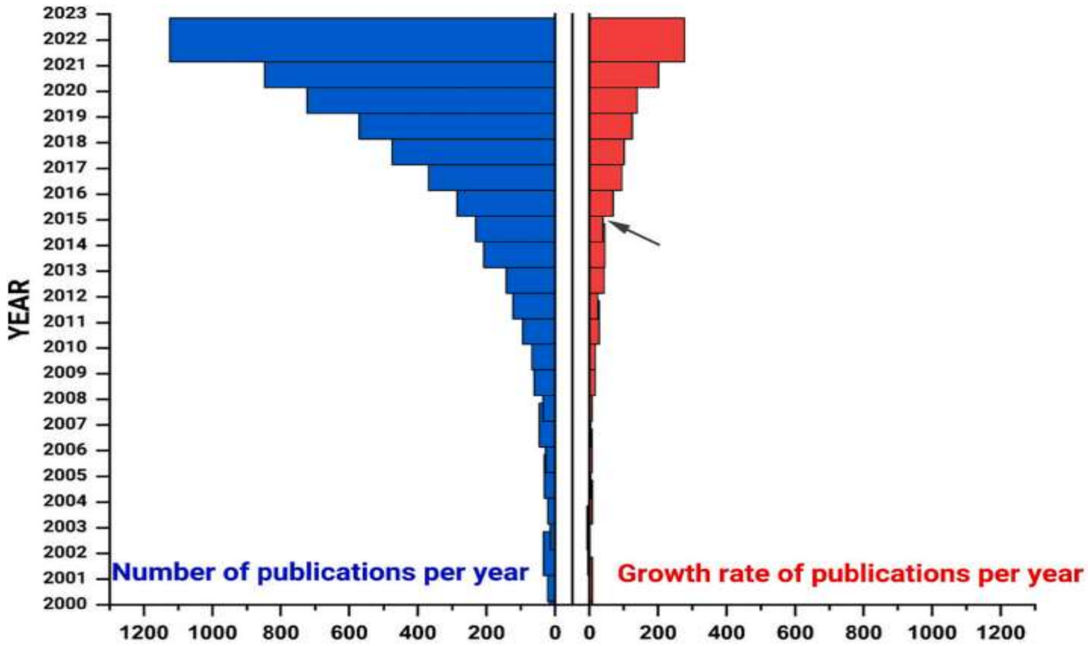

Figure 1.8. Annual distribution of BTMS publications from 2000 to 2022 (Kharabati & Saedodin, 2024)

Thanks to increase of the electric vehicles at last years, it seems that there is more publications on the battery thermal management systems from Figure 1.8. It means that thermal management is a significance problem for electrical vehicles and researchers try to find a new solution way. This problem can be explained as follows: Temperature significantly influences the performance, lifespan, and safety of Lithium-ion Batteries (LIBs). According to the data obtained from the literature, the temperature limit values at which the battery pack is safe and efficient are 15°C (lower value) and 35°C (upper value) (Siddique, Mahmud, & Van Heyst, 2018). To ensure safe and high performance driving, temperature of the battery must be steady at the working condition.

Many battery thermal management systems (BTMS) where can be seen at Figure 1.9 have been designed over the years to solve this problem. Because first researchers focused on the external battery thermal management systems, it can be seen that there is a significance advancement in this area. Also, inspired by healing channels used in carbon fiber-reinforced composites to repair cracks and delaminations some researchers have developed embedded cooling channels (Pety, Tan, et al., 2017). Especially, since existing battery cases use metal piping to cooling process, they are very heavy. If we use embedded cooling channels in the carbon fiber reinforced materials, it is possible to obtain a lighter battery cases. Carbon fiber reinforced materials have low weight, good damping and vibration reduction properties, thanks to these properties it can be a good choice when we design a more durable and lighter battery case.

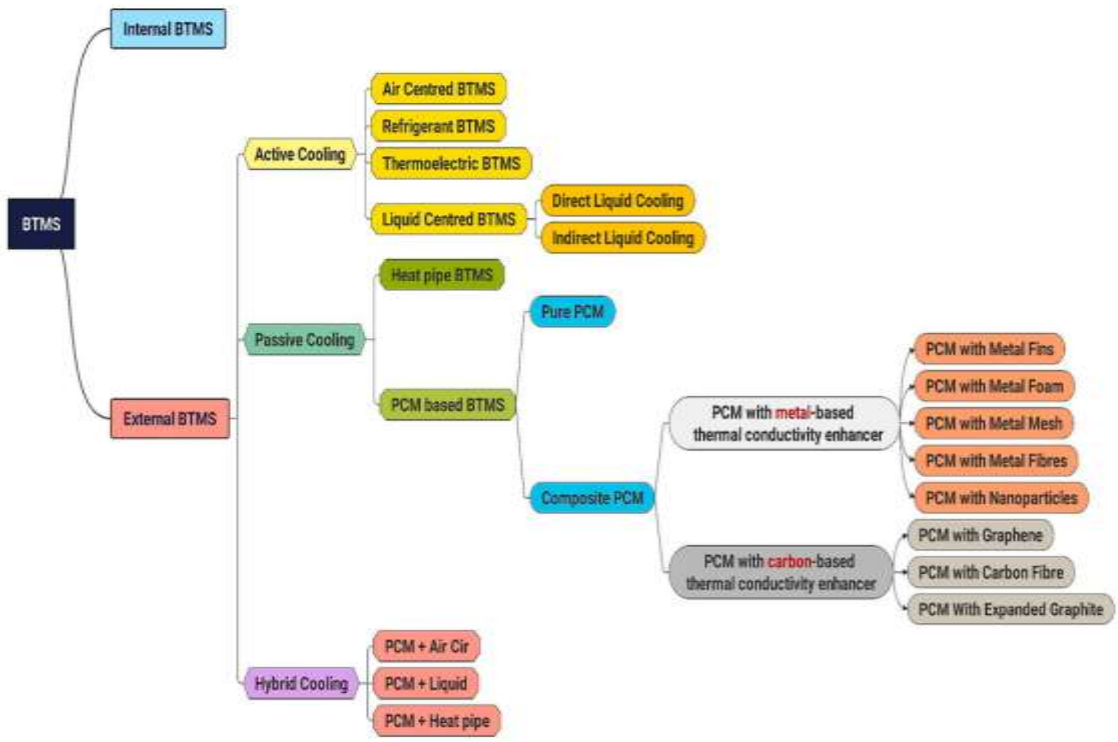

Figure 1.9. Battery thermal management systems (BTMS) (Kharabati & Saedodin, 2024)

On the other hand, there are limited studies in the literature on the effects of microchannels embedded in composite structures for thermal management on the mechanical properties of the material. Current production methods are not suitable for the production of channelled composites with different cross-sectional geometries because they directly interfere to the internal structure of the material or disrupt fiber integrity, directly or indirectly affecting the mechanical properties during the production of the different channel geometry. Therefore, the most of the studies to date have focused solely on circular cross-sectional channels, preventing the development of smart composite systems with different cross-sectional geometries. However, thanks to a newly developed production method, the production of smart composites with various microchannel cross-sectional geometries is now possible without directly machining the main composite material or disrupt fiber alignment (Geren N, 2024; Koştur, Geren, & Demirel, 2025). Therefore, determining the impact of the channel's geometric form on the impact and flexural behaviour of the composite is crucial for both the structural safety of such systems and the optimization of multifunctional designs.

This thesis aims to address this gap in the literature by experimentally investigating the mechanical behaviour of carbon fiber-reinforced composites (CFRP) with different macro or microchannel cross-section geometries. The results obtained aim to provide new and original findings regarding the effects of microchannel geometry on structural performance.

2. PRELIMINARY WORK

2.1. Literature Review – Introduction

This literature review aims to provide the reader with a comprehensive overview of the applications of composites containing embedded micro-channels and previous studies on this topic, examining them under various titles, from general to specific. A critical evaluation of existing studies will be conducted, focusing specifically on the effects of micro-channels on flexural performance, impact resistance and interlinear shear strength (ILSS). Finally, predictions will be made regarding how these studies may affect the material properties of test specimens with different channel geometries.

Investigation of the findings will provide the necessary background to identify the limitations of existing research and highlight the novelty and motivation behind this thesis, which focuses on the experimental investigation of CFRP composites with various microchannel geometries.

2.2. Embedded Channel (Vascular channel) Applications in Composite Materials

Before the concept of embedded channels occurred, composites were primarily developed to provide structural strength and reduce weight. The inefficiency of existing materials under certain operating conditions, combined with advancements in molding and manufacturing techniques, has led to the emergence of a new class of functional materials consisting essentially of various embedded microchannel networks. This concept mimics biological microvascular systems and holds promise for providing intelligent solutions to long-standing problems in structural materials. The primary function of embedded microchannel networks in fiber-reinforced composites is to provide free space and pathways for the storage and transport of a functional fluid to a desired location within a structure, such as blood vessels, and to perform one or more of the following functions: damage sensing (damage healing), self-healing, and cooling, either simultaneously or separately.

This section of the research is important because understanding and learning of the applications area of the embedded channels in composite materials will help us to dream and design new and more usable structures. Like, using these channels for the thermal management.

2.2.1. Damage Detection

It is well known that fiber-reinforced polymer (FRP) laminates are susceptible to damage from low-velocity impacts (Abrate, 2001). Impact damage can cause a significant reduction in the undamaged structural strength of polymer-matrix composites. The extent and volume of damage typically peak in the lower half of the laminate as it moves away from the impact surface and decreases toward the back surface . This damage, if it occurs at a macroscopic level, can be easily detected and repaired. However, microscopic damage such as matrix micro-cracking, fiber-matrix separation, and delamination is more insidious and can go unnoticed and unrepaired, leading to nearvisible impact damage (BVID). The impact of this hidden damage on laminate properties can be significant, especially under pressure conditions where strength can be reduced by up to 50% (Richardson & Wisheart, 1996). For these reasons, the use of damage detection can be highly beneficial.

To enable autonomous healing in advanced composite structures and provide a detailed understanding of the damage profile to be repaired, microchannel-based damage repair systems deliver X-ray or ultraviolet (UV) opaque fluids to the damage site. This application enhances the visibility of hidden damage associated with micro-channels (McCombe, Rouse, Trask, Withers, & Bond, 2012; Pang & Bond, 2005). Measuring the damage volume and mapping its location through the thickness is crucial to ensuring that the transmission infrastructure provides adequate recovery at critical points while maximising coverage and minimising structural cost. To this end, G.P. McCombe and colleagues used commonly used non-destructive assessment techniques (ultrasonic C-scan, low- and high-resolution X-ray CT scanning) to determine the damage formation and interaction of a self-healing hollow glass fiber arrangement embedded in a damage-resistant, quasi-isotropic 16-layer CFRP laminate. A hollow glass fiber (HGF) layer with a 100 μm outer diameter and 200 μm pitch was embedded in a 0-layer layer and placed at interface 3 or 13 (Figure 2.1). The samples were subjected to a drop impact with a pressure of 3 J, 4 J, or 5 J before being subjected to ultrasonic C-scan and X-ray CT scanning (McCombe et al., 2012). It is seen that the primary objective of the study was to evaluate the damage volume and distribution throughout the thickness of the laminate. Additionally, the effect of adding HGF layers on damage formation and the interaction of damage with HGF was evaluated in this study.

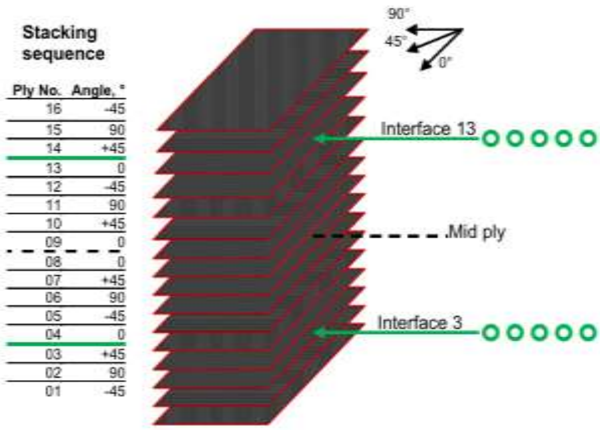

Figure 2.1. Exploded laminate specimen stacking sequence showing the 3rd and 13th interface insertion locations for the HGF. The samples are impacted on ply 16 (McCombe et al., 2012)

2.2.2. Self Healing

Damage and failure are natural consequences of material applications. Latest engineering research has been focused traditionally on the design of new and smart materials with increased strength. As a result of this research, one of the newly emerging concepts is the self-healing mechanism.

Self-healing fiber-reinforced polymer composites possess the ability to heal in response to damage wherever and whenever it occurs in the material. This perfect material behavior is inspired by biological systems in which self-healing is commonplace, like the human body (Zhao et al., 2014). Thanks to the healing agents contained within the vessels which embedded in the smart composite structure, smart composite materials can automatically heal when damaged without any external intervention. Through self-healing, it is expected that safety and reliability will improve, the maintaining cost of artificial composites will decrease, and material life will be extended.

Current self-healing composites can be categorised into three groups: capsule-based, vessel-based based and intrinsic self-healing materials (Figure 2.2) (Blaiszik et al., 2010; Wang, Pham, Ji, & Harkin-Jones, 2015). In capsule-based self-healing materials, small capsules containing a liquid able to fill and close cracks are embedded under the material surface. When the material is damaged, cracks cause some capsules to rupture, releasing the liquid and closing the gap. For vessel-based self-healing materials, the capsules are replaced by a vascular structure similar to a tunnel network, in which various functional liquids flow. These functional liquids will also fill the gap when a crack occurs and breaks the vascular network. The material contained inside a capsule or a vascular network is called a healing agent. The mechanism and behaviour of healing agents are fundamental to the recovery process and restoration of mechanical properties. Intrinsic self-healing materials heal through the inherent reversibility of chemical or physical bonding instead of structure design.

The primary purpose of using vascular channels rather than a capsule-based self-healing mechanism is to ensure continuous healing agent delivery and flow control by replenishing the healing agent through the circulatory system. Some studies have demonstrated that continuous self-healing of structural fiber composites via microvascular delivery is possible, although several uncertainties like pumping time and pumping power (Hart et al., 2017; Patrick et al., 2014).

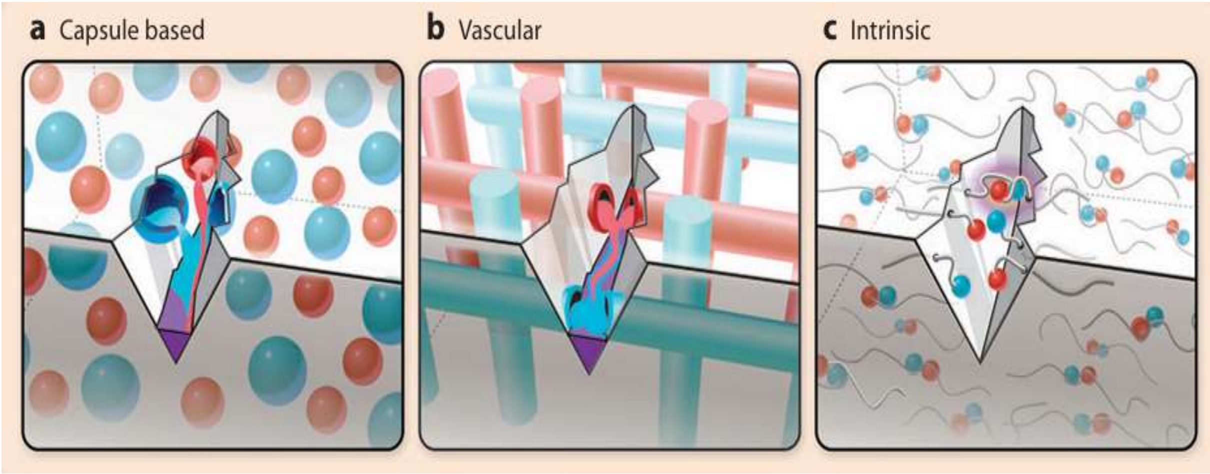

Figure 2.2. Approaches to self-healing include (a) capsule-based, (b) vascular, and (c) intrinsic methods (Blaiszik et al., 2010)

2.2.3. Thermal Management

The structural performance of carbon fiber-reinforced composites (CFRCs) can be degraded under high-temperature conditions, such as in applications of high-speed flight (Hengeveld, Mathison, Braun, Groll, & Williams, 2011; Meese & Nørstrud, 2001; Meetham, 1991), vehicle transportation (Johnson, Evans, Jacobsen, Thompson, & Christopher, 2004; Sonsino & Moosbrugger, 2008), and the cycling of batteries, fuel cells, and other electronics. These properties of Fiber Reinforced Polymer (FRP) composites may restrict their adoption in future vehicles. The effects of elevated temperature can change depending on the magnitude and duration of thermal exposure. Subjecting the composite structure to temperatures over the glass transition temperature reduces the thermo-mechanical performance in a short time, and it can cause permanent damage, including delamination, matrix cracking, plastic deformation, ultimately combustion and fire in the long term. In order to minimize the negative effects of the elevated temperature on the composite structure and improve the thermo-mechanical performance of FRP composites, a new and smart material design has been developed by the researchers. It can be seen that active cooling can be achieved (Pety, , , & White, 2017) owing to this developed mechanism from the literature. This mechanism is based on the circulation of coolant through microvascular channels embedded in the composite structure (Figure 2.3). Thus, thermal energy can be removed from the laminate through the coolant (like water or glycol), so this mechanism enables safe structural performance under high thermomechanical loading potentially.

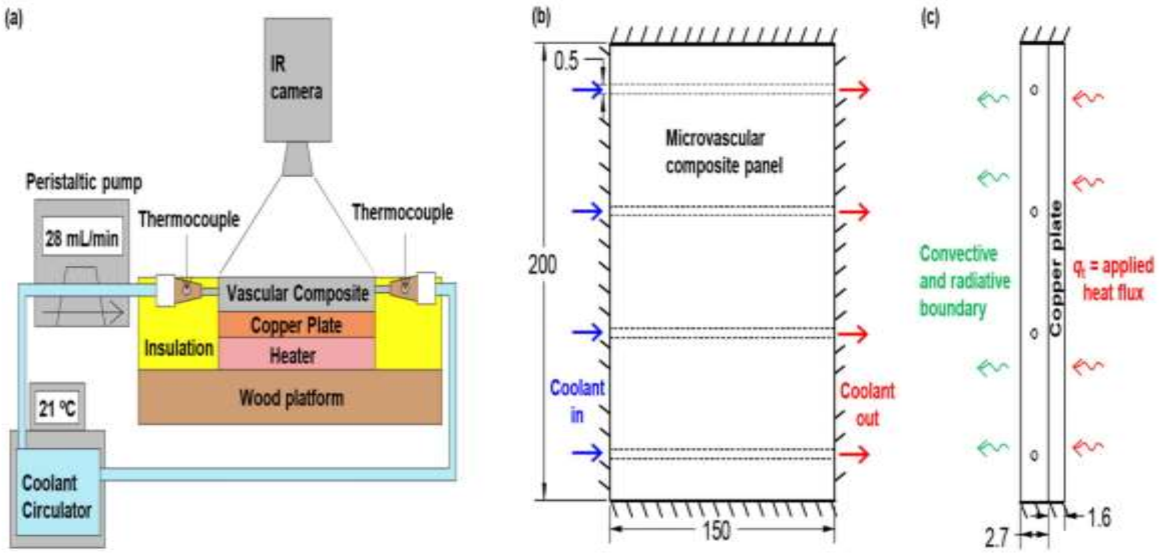

Figure 2.3. Schematics of cooling experiments and simulations. (a) An experimental setup where panel temperature is measured with an IR camera while coolant temperature is monitored with thermocouples embedded in the microchannel inlets and outlets. (b), (c) Top and side view of the simulation model (dimensions in mm). The microvascular composite panel is heated from below while coolant circulates through all channels at a set inlet temperature and flow rate (Pety, , et al., 2017).

On the other hand, extremely low temperatures can cause a serious problem due to different coefficients of thermal expansion and micro-cracking. In addition, fiber-reinforced polymer composites (FRPC) may be used in components that must be kept warm for other reasons. Ice formation is likely the primary factor to use vascular heating because ice formation can severely disturb the aerodynamics of aircraft wings and the blades of turbofan engines, and wind turbines. There is no reason why vascular heating should be used to circulate a hot fluid through the network, dissipating its heat into the laminate and thus raising the temperature, reducing thermal residual stresses or melting accumulated ice (Cole, 2020).

Batteries in electric vehicles (EVs) require a packaging system that provides both thermal regulation and crash protection. Several designs obtaining the active cooling of microvascular carbon fiber-reinforced composites to achieve this multifunctional goal exist in the literature. The main objective of this study is to determine the optimal channel geometry for cooling channels against the impact and flexural loads within the scope of the project "Development of a Self-Healing Battery-Pack System Incorporating an Active Thermal Management System," managed by Geren et al (Geren N., 2024) A new channel formation method will be used in this study. To better understand how this method differs from other channel formation methods in the literature, other channel formation methods should also be examined in detail.

2.3. Microvascular Channel Creating Methods

Microvascular channels were first used for damage detection by researchers and for the self-healing process by the US Army. Afterwards, these channels are used for active cooling for high temperature conditions in the carbon fiber reinforced composites (White et al., 2006). Different techniques are available in the literature to fabricate the carbon fiber reinforced composites, which contain microvascular channels. These techniques are discussed under the removable and non-removable core method below.

2.3.1. Non-Removable Hollow Cores

The basic principle behind non-removable hollow core-based techniques is quite simple. An array of straight, non-removable hollow tubes made of glass, metal or polymer is placed between the fabric layers during composite manufacturing. Upon curing, these embedded hollow tubes serve as microchannel for various applications. The schematic illustration of the principle behind these techniques is shown in Figure 2.4.

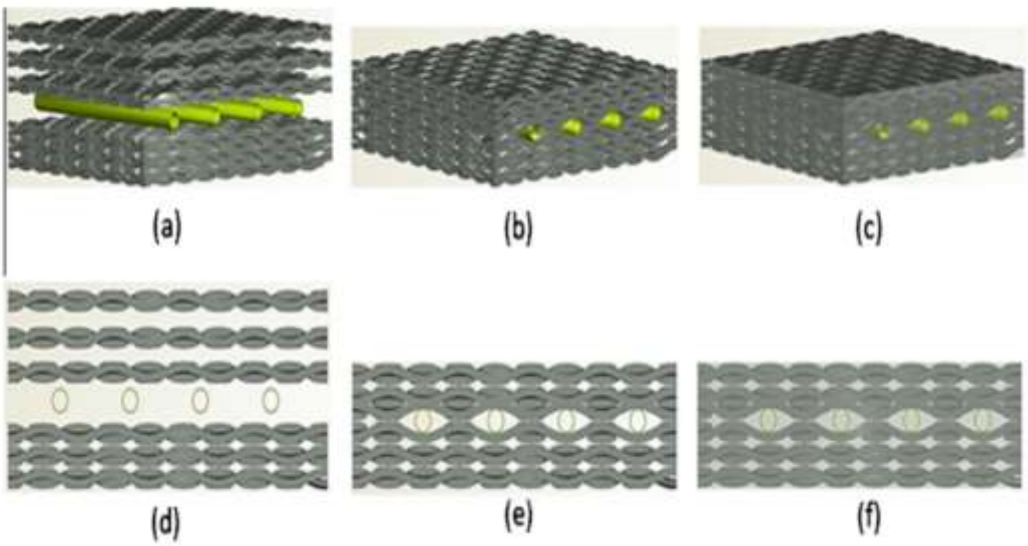

Figure 2.4. Schematic diagram for manufacturing techniques based on non-removable hollow cores (a and d) placement of hollow cores (glass, polymer or metallic) between dry fabric layers, (b and e) composite processing (hand lay-up, vacuum bagging, resin infusion, RTM or autoclave) and (c and f) cured composite laminate with embedded microchannel (Saeed, Chen, & Li, 2015)

Hollow Glass Tubes (HGT)

In this field, the first studies were made by Dry (C. Dry, 1996; C. M. Dry & Sottos, 1993) in order to create micro channels in self-healing. He placed a few pairs of four-inch-long glass pipette tubes with 100 μl volume in epoxy resin samples and filled one tube with resin and the other with hardener. Later, these samples were subjected to low-velocity impacts, which damaged the epoxy samples and broke the glass tubes. The contents in the tubes leaked, reached the damage area, reacted there to ensure healing in the samples and restored their lost strength.

Hollow Glass Fibers (HGF)

For this method, a tube which was made of glass fiber is placed into the carbon fiber reinforced composites so cooling channels can be obtained, but this process will be time-consuming, and it may negatively affect the mechanical properties of the composites. That's why this method is not found useful for our study.

Hollow Polymer Tubes

Williams et al. (H. R. Williams, R. S. Trask, & I. P. Bond, 2007) bonded polyvinyl chloride (PVC) tubing (1.5 mm diameter) between two 5 mm thick half cores having 2 mm wide and 2.5 mm deep already machined straight channels. They drilled 1.5 mm diameter vertical holes in the channelled core at appropriate locations to form an interconnected channel network. Finally, they fixed this channelled core between two (laminate) skins to produce a microchannel composite sandwich structure, as shown in Figure 2.5. The authors tried different approaches of self-healing on this structure, and fully regained compression after impact (CAI) strength in the samples with good resin-hardener mixing. With the development of this structure, they demonstrated that channelising a sandwich structure has minimum effect on static mechanical properties of the panel, while offering additional benefits of self-healing (H. R. Williams et al., 2007).

Again, we can say that this method time time-consuming and can affect the mechanical properties of the composite structures. So this method was not considered in this study.

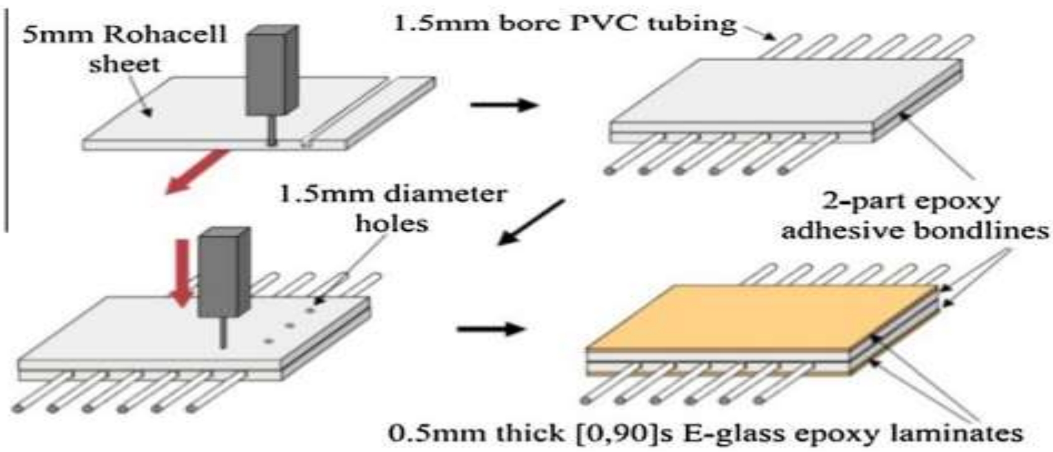

Figure 2.5. Manufacturing process for microvascularized sandwich structure (H. R. Williams, R. Trask, & I. Bond, 2007)

2.3.2. Removable Solid Cores/Preforms

The procedure for microchannel creation by removable solid preforms is very similar to non-removable hollow cores. The first step is the positioning of removable solid preforms that may be polymer or metallic between the dry fabric layers. After positioning, resin infiltration and curing are subsequently performed to obtain a composite laminate. Finally, hollow channels are revealed by removing preforms from the cured laminate. The way to create a hollow microchannel by removable solid preforms is shown in Figure 2.6.

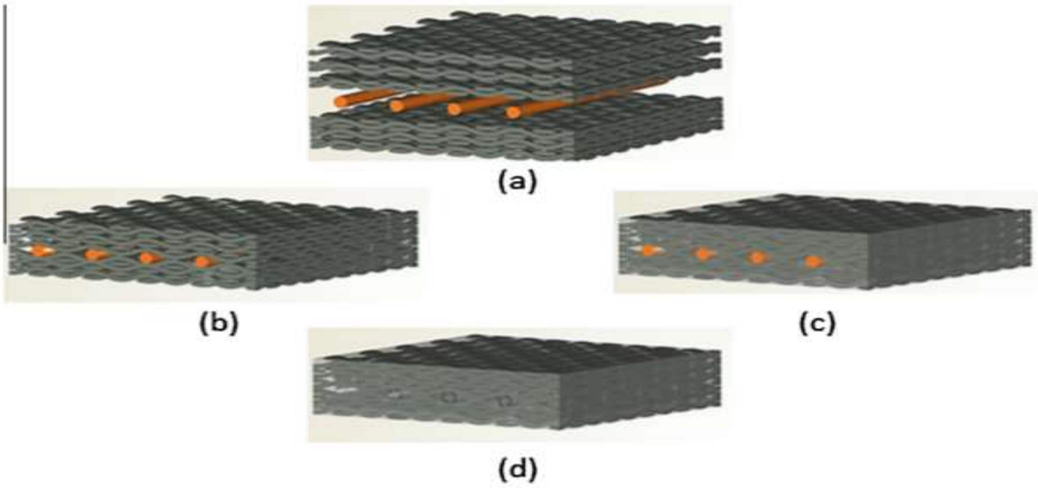

Figure 2.6. Schematic illustration for microchannel creation by removable solid cores (a) placement of solid cores (nylon fibers or low melting temperature soldering wire) between dry fabric layers, (b) composite processing (hand lay-up, vacuum bagging, resin infusion, RTM or autoclave), (c) cured composite laminate and (d) exposing microchannel by manual removal of solid mandrels (Saeed et al., 2015)

Polymer Fibers/Mandrels

Hamilton et al. utilized 280 μm diameter nylon fibers as a removable preform to create a microvascular system. They also measured the displacement field surrounding a single channel in tension and verified their results with an analytical solution. So, the first studies were developed on the removable solid cores.

Also, this method sounds similar to the method which is improved by Koştur and used during the manufacturing of channelled test specimens in his thesis (Eray 2024). However, the method used by Koştur layed the polyamide monofilaments within the composite parallel to the wowen fabric rather than in the vertical direction the fabric.

Metallic Wires

Trask et al.(R. Trask & Bond, 2010) created vascular networks within CFRC using low-melting-temperature soldering wire. The melting temperature of the soldering wire used was low enough for its easy removal by heating and high enough to withstand the resin's curing temperature. So they could remove soldering wire from channels. In some applications which need a higher wire diameter, removing all of the wire from the channels was not possible, which caused channel congestion. This situation can be a barrier in front of the cooling fluids. Furthermore, undesirable internal channel defects can affect the test results. Because of these problems, this method is found to be not technically useful.

Micromachining/Laser Processing

Conventional and modern micromachining methods have long been used to create vascular in metals for cooling applications. Precision machining, computer numerical controlled (CNC) machining, electric discharge machining (EDM) and laser machining have been used to create micro channels of few hundred micron (Dixit & Ghosh, 2015; Hung, Chang, & Chuang, 2012; Woias, Andrews, Papautsky, & Gerner, 2004) but this process (The schematic illustration is showed in Figure 2.7) effects the mechanical properties of the composite structure negatively and it is an expensive technology. It is found to be unsuitable for use in this work.

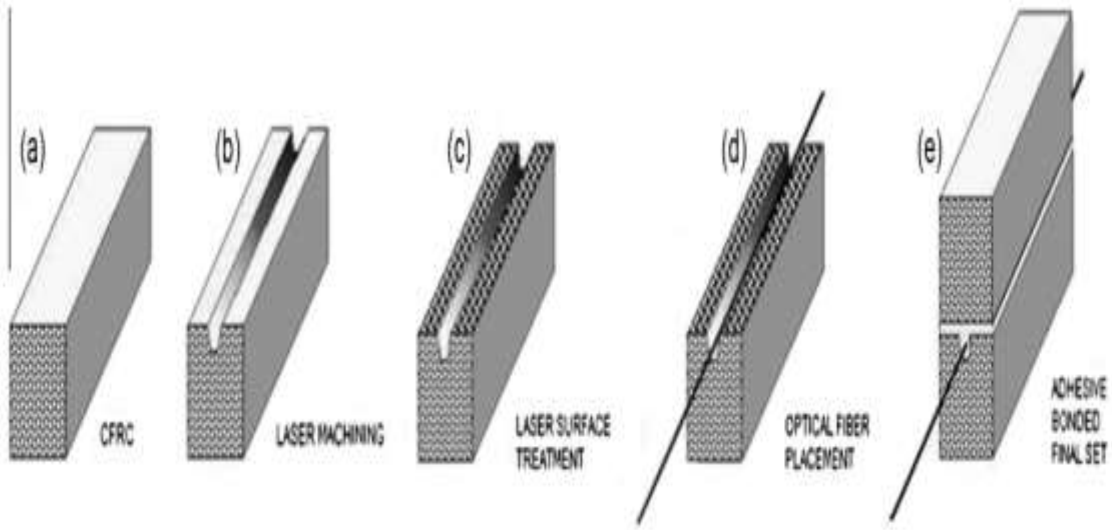

Figure 2.7. Schematic of creation microchannel by laser processing (a) composite block, (b) microchannel creation by laser machining, (c) surface texturing by laser, (d) optical fiber placement in the created microchannel, and (e) joining of the two half blocks using adhesive (Lima, Sakamoto, Simoes, & Riva, 2013)

Direct Ink Writing

Direct ink writing (DIW) is a fabrication method in which a computer-controlled fine nozzle moves and creates a three-dimensional pattern by depositing ink in a controlled architecture (D. Therriault, S. R. White, & J. A. Lewis, 2003). Schematic of the DIW process is shown in Figure 2.8.

Therriault et al.(Lewis, 2006; Daniel Therriault, Scott R White, & Jennifer A Lewis, 2003) fabricated three-dimensional micro-channel networks by DIW using a fugitive ink to promote fluid mixing through chaotic advection. They first deposited an organic ink on a cured epoxy substrate and formed a 3D network using a layer-by-layer approach. After deposition, the whole assembly was infiltrated with epoxy resin and left to cure. Once cured, the deposited ink was removed via heating and a slight vacuum to create a hollow 3D microchannel network (Lewis, 2006).

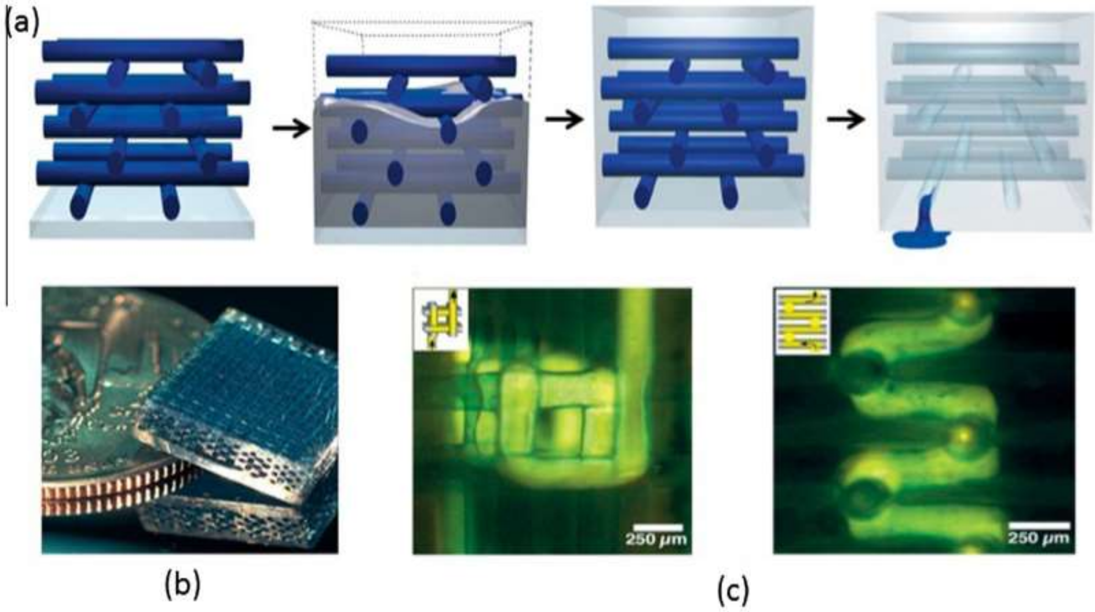

Figure 2.8. (a) Schematic representation of DIW (from left to right) ink deposition on cured substrate, epoxy infiltration of completed network, curing, evacuation of fugitive ink; (b) optical image of 3D microvascular network and (c) fluorescent images (top and side views) (Lewis, 2006)

It can be seen that various techniques are available to fabricate microvascular channels in the carbon fiber reinforced composites, and these techniques are categorised under the removable or non-removable cores in the literature. In order to minimize the effects of the microvascular channels on the mechanical properties of the fiber reinforced composites removable core microvascular manufacturing channel method should be used.

In this direction, a new method which is developed by Geren (Geren N., 2024; 2024) et al. (Geren N, 2024; Koştur et al., 2025) will be used. This method is based on the principle of creating a channel by taking advantage of the thermal expansion properties of a material that is polyamide 6 (PA-6) and its derivatives. During the manufacturing of the fiber reinforced composite structures, polyamide monofilament materials, which have different cross-section geometries placed between the fiber layers. At the composite curing temperature, the polyamide expands more than the composite structure, creating a wider internal channel hole within the structure. After hot press implementation, the composite plate is cured, and the monofilament materials are removed from the fiber-reinforced composites manually. Eventually, fiber reinforced composite structures which have microvascular channels at different cross-section geometries are obtained within the manufactured composite.

2.4. Mechanical Effects of the Vascular Channels

Inspired by biological microvascular systems, the inclusion of microchannels within FRP composites enabled them to execute additional functions (Swait et al., 2013; Zhao et al., 2014), but on the other hand, they also acted as cavities and stress concentration points and affected the structural strength of the composites. Understanding the impact of structural modifications, such as embedded micro-channels, on the low-velocity impact and flexural behavior of carbon fiber-reinforced composites provides predictions for optimising both mechanical performance and lightweight design. Evaluating composite materials under low-velocity impact and flexural loading is important for understanding their mechanical performance and potential applications in structural components.

This effect on the mechanical properties was investigated and reported by a number of researchers. In this section, the effects of embedded micro-channels on stiffness, strength and interlaminar shear are discussed.

2.4.1. Flexural Strength

Trask (R. S. Trask, Williams, & Bond, 2006) and Williams (G. Williams, R. Trask, & I. Bond, 2007) have conducted similar studies in the field of self-healing applications. In these studies, GFRP and CFRP composites with embedded micro-channels were fabricated, and four-point flexural strength tests were applied. Both researchers placed hollow glass fibers (HGFs) with an inner diameter of 40 μm into the laminate at intervals of 70 and 200 μm, but they used different composite structures. Trask et al. placed HGFs in GFRP composites, while Williams et al. placed them at specific points in CFRP composites. Trask et al. found a 16% decrease in flexural strength in GFRP composites, and Williams et al. found an 8% and 2% decrease in CFRP composites with micro-channels at 70 and 200 μm intervals, respectively. These decreases in flexural strength were thought to be due to disruption of the fiber architecture, the formation of resinous regions, and the replacement of reinforcing fibers with non-structural HGF (reduced fiber volume fraction). Also, the results of studies on the four-point bending strength of FRP composites containing micro-channels show that the loss of bending strength is greater in channels that are closer to each other, as mentioned above.

2.4.2. Impact Damage

Impact damage is another topic investigated within the scope of this thesis in order to examine the mechanical effects of micro-channels. An et. al. (An et al., 2025) experimentally investigated the low velocity impact (LVI) and post-impact compression (CAI) performances of CFRP (Carbon Fiber Reinforced Polymer) laminates containing three-dimensional microvascular channels produced using the sacrificial fiber method. In the study, the effects of microvascular channels on the impact resistance and post-damage mechanical properties of the composite material were comparatively evaluated.

Low-Velocity Impact (LVI) Performance

According to the research results, the peak impact force of the microvascular specimens was found to be 7% to 10% lower compared to the control specimens. In addition to this decrease, a 2% to 21% decrease in delamination area was observed. This is because the composite material's strength is lower in the direction perpendicular to the channels, causing damage to occur earlier and interrupting the stress transfer path. Impact damage, however, propagates more in the direction parallel to the micro-channels. Consequently, less fiber breakage or delamination occurs in the width-wise direction in microchannel samples, resulting in higher CAI strength.

Post-Impact Compression (CAI) Performance

Post-impact compression test results show that the CAI strength of the laminates with microvascular channels is 5% to 9% higher than the control group. This finding indicates that the microvascular channels increase the post-impact load-carrying capacity of the material. As a result, this study demonstrates that microvascular channels have a positive effect on the impact performance of CFRP laminates and help maintain the integrity of the material by altering the failure mechanism.

In another study, Kousourakis et. al. (Kousourakis, Mouritz, & Bannister, 2006) investigated the impact damage on the on the laminate without galleries, the laminate containing 0.17 mm or 0.68 mm glass-tube galleries, and the laminate containing 0.58 mm or 2.78 mm pure galleries (made using the silicone tubing) with respect to the test standards (ASTM D5628-96). They reported that the damage in the laminate containing small galleries (Figure 2.9. (a)) was approximately equal in length in the normal (damage width) and parallel (damage length) directions to the direction of the galleries, on the other hand the shape of the damage zone became more elliptical as the galleries size increased (Figure 2.9. (b)), with the damage zone being shorter in the normal direction to the galleries. Also, the length of the impact damage zone in the directions that are normal and parallel to the galleries is measured to understand the damage distribution on the test specimens under different gallery diameters (Figure 2.10).

These studies help us understand how impact damage affects material properties and how damage progresses under different channel diameters. Using the information and test methods obtained from these studies, low-velocity impact tests will be applied on test specimens with different cross-sectional geometries to examine how different channel geometries affect the damage mechanism and damage quantity.

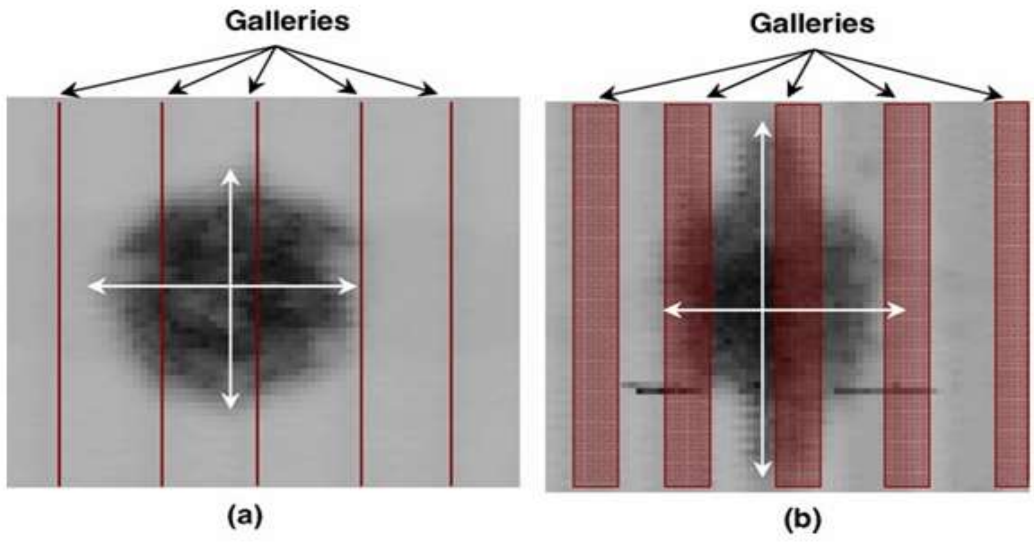

Figure 2.9. C-scan image of (a) 0.68 mm gallery coupon and (b) 2.98 mm gallery coupon damage. Energy = 20.9 J. The arrows on the image indicate the length and width of the impact damage zone (Kousourakis et al., 2006)

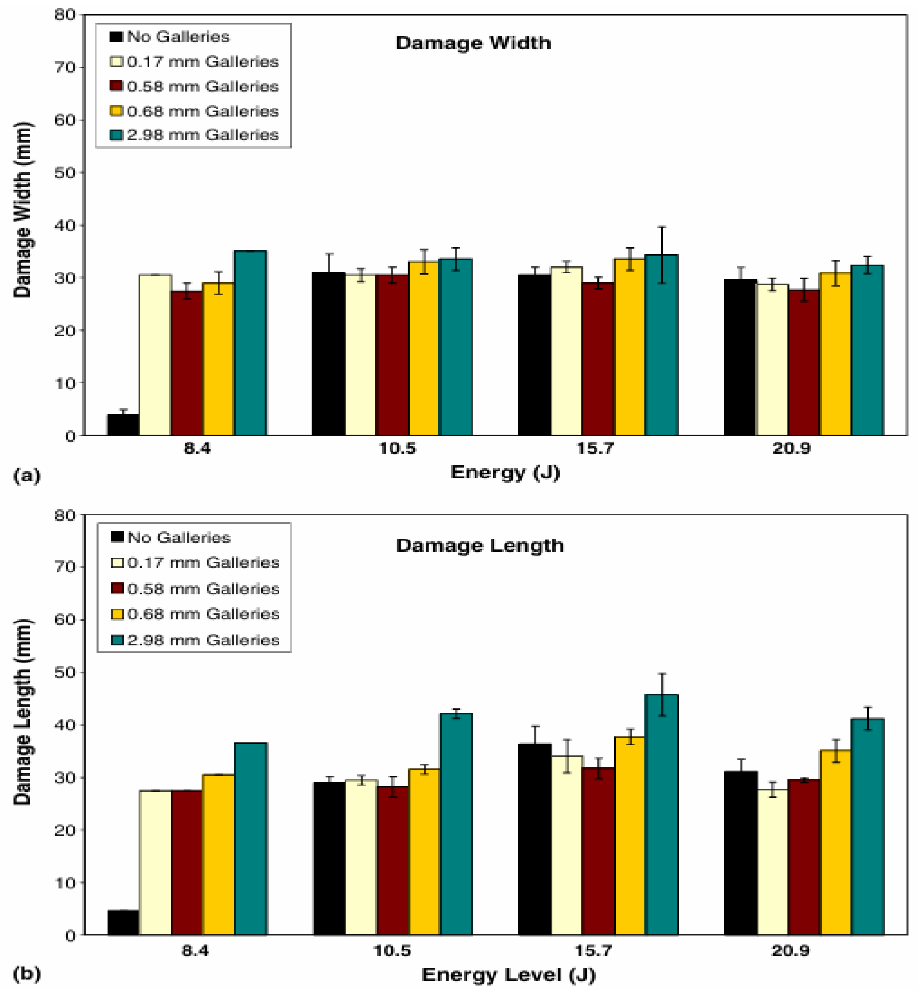

Figure 2.10. Impact damage length (a) normal and (b) parallel to the gallery direction (Kousourakis et al., 2006)

2.4.3. Interlaminar Shear Strength(ILSS)

Michael et al. suggest that the interlaminar shear strength (ILSS) reduction frequently observed in composites is a combination of the reduction in net cross-sectional area caused by distributed voids and the initiation of failure due to larger discrete voids. According to these, the suggested embedded channels in the composite structure can cause a reduction in the cross-sectional area. Thus, these channels affect the inter-laminar shear strength negatively. Also, Kousourakis et al. (Kousourakis et al., 2006) showed that ILSS of CFRP composites decreased linearly with increasing micro-channel diameter, for both types of micro-channels created by HGT (Hollow Glass Tube) and silicon mandrel (Figure 2.11). It can be seen that the ILSS drops by 1.8% for every 0.1 mm increase in the gallery diameter for the pure galleries and by 1.1% for every 0.1 mm increase in gallery diameter for the glass-tube galleries.

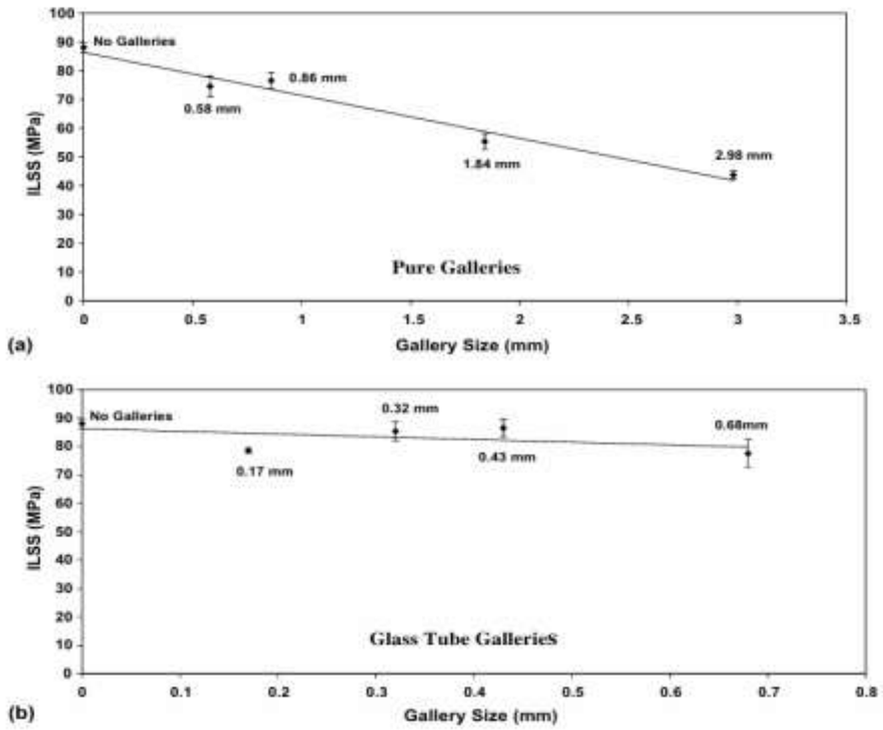

Figure 2.11. ILSS vs. gallery diameter (a) pure galleries and (b) glass tube galleries (Kousourakis et al., 2006)

Koutsourakis et. al. investigated the mod 1 delamination toughness value separately based on gallery size (Figure 2.12. and gallery spacing (Figure 2.13) variables within the same study. According to the result of this investigation, the delamination toughness of the laminate containing the pure galleries increased with gallery diameter at a linear rate up to 0.86 mm. Beyond the 1.84 mm gallery size, which gives a toughness value about twice that of the gallery free material, the delamination toughness appears to be independent of the gallery diameter, although eventually it is expected to decrease when the galleries are very large. And this was accounted for by a high percentage of the fracture plane within the CFRP specimen. The delamination toughness of the laminates containing the glass tubes also increased with gallery diameter, and for a given size, the improvement is slightly greater than that achieved for the pure galleries. In addition to this information, they show the typical relationship between gallery spacing and mode I delamination toughness in Figure 2.12. In conclusion, delamination toughness increases with the introduction of the galleries, but does not change significantly when spacing is greater than about 2mm, according to this study.

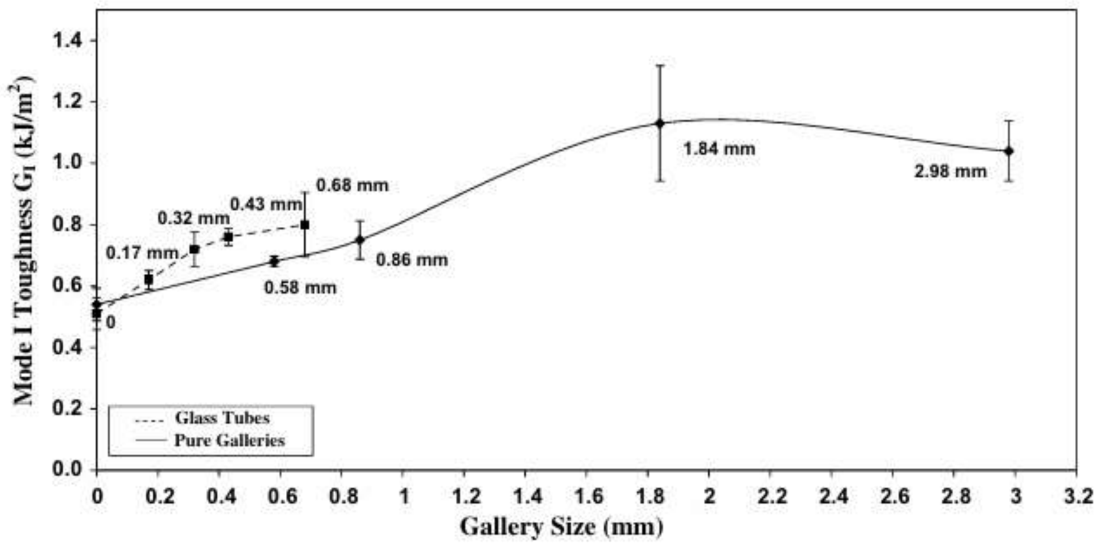

Figure 2.12. Mode I fracture toughness vs. gallery diameter. The gallery spacing was constant at 5 mm for the pure galleries and 3 mm for the glass-tube galleries (Kousourakis et al., 2006)

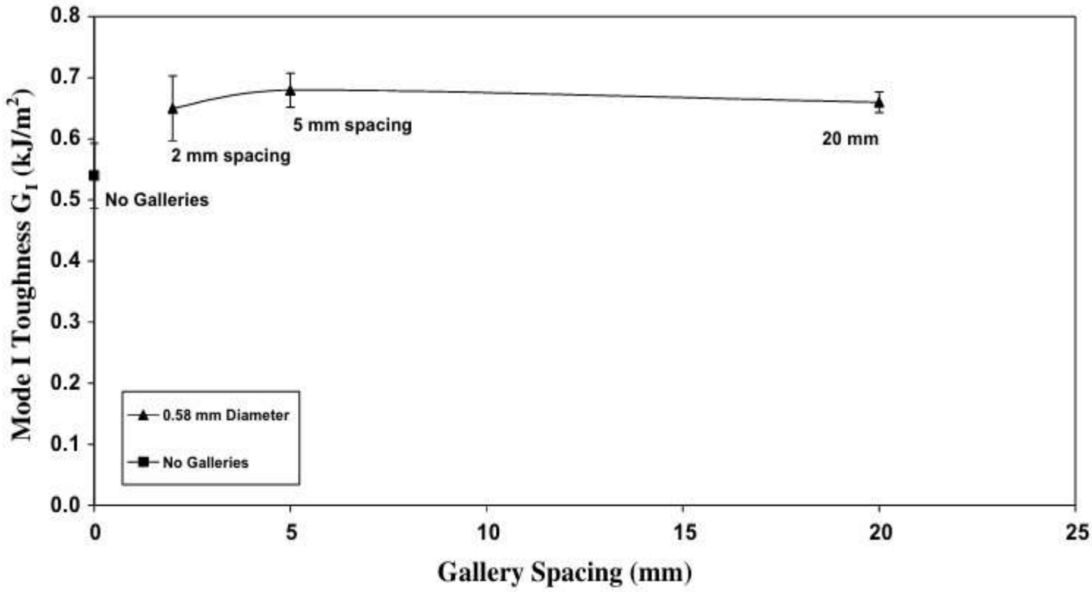

Figure 2.13. Mode I fracture toughness vs. gallery spacing. The data is for the laminate containing 0.58 mm pure galleries (Kousourakis et al., 2006)

2.5. Effect of Different Channel Geometries on Mechanical Behavior

In the previous section, only the mechanical properties of smart composites which have a circular cross-sectional area were commented on. The most important issue in this study is how channel geometries affect the material properties in composites which have different channel geometries. When we look at the current studies in the literature, almost all of the created channels have circular geometry. It can be caused that current channel creation methods used in composite materials are inadequate, inefficient, time-consuming or challenging in creating different channel geometries. Or, the researchers may have thought that channel geometries with sharp edges would negatively affect impact strength and flexural strength, considering that circular channel geometries make the stress distribution around the channel more homogeneous and cause less stress concentration.

There are studies in the literature (Ahmed & Ahmed, 2015; Phillips, Ryan Pierce, & Baur, 2011) that have conducted various simulation analyses to select the optimal thermal design for structures with different channel geometries. These studies demonstrate that it is a matter of interest how channel geometry will affect thermal design. Pety et al. (Pety, , et al., 2017) designed a battery box with an internal rectangular cross-section (1020 μm x 840 μm dimensions), cooling channels to provide thermal management in the battery box of electric vehicles (Figure 2.14). In this study, CFD simulations were used to evaluate which of four different network designs (Figure 2.15) provided the best thermal performance. However, this study did not explain how the rectangular channel geometry affected the material properties, and the scope of the study was limited to thermal performance analyses. To select the channel geometry with better thermal and mechanical properties, it is necessary to determine how different geometries affect the material's mechanical properties.

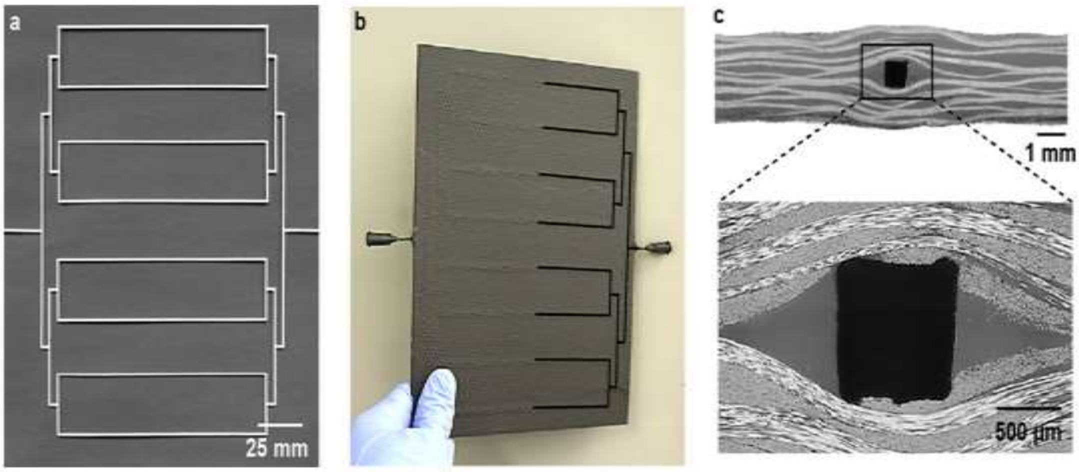

Figure 2.14. Carbon fiber/epoxy composite panels with 2D channel networks. (a) Laser-cut PLA network with the bifurcating channel design. The network is 840 µm thick, and strips are 1020 µm wide. (b) Composite panel with bifurcating channel network after curing and VaSC treatment. The right half of the embedded network is outlined in black for visualisation. (c) Cross-sectional micrograph of a 1020 µm 840 µm rectangular channel embedded in a carbon/epoxy composite (Pety, , et al., 2017).

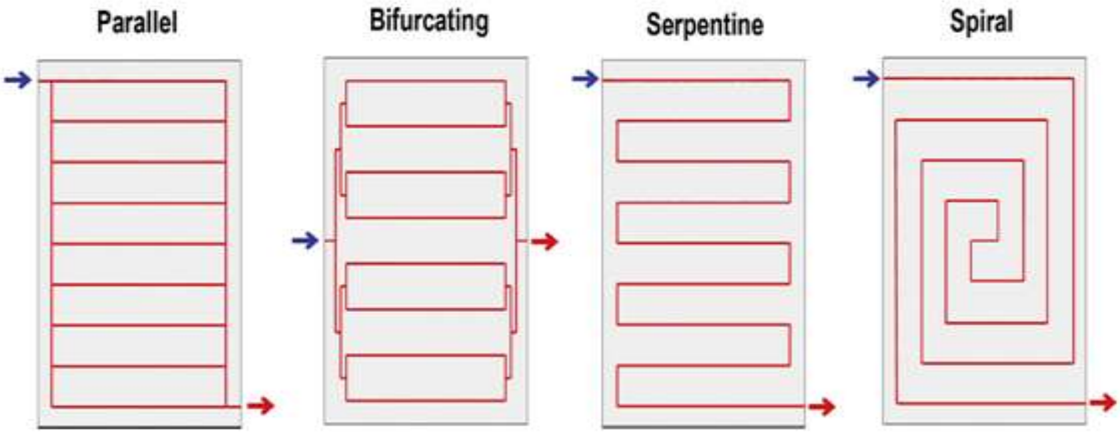

Figure 2.15. Four main network designs used for cooling studies, with inlets denoted in blue arrows and outlets in red arrows(Pety, , et al., 2017).

2.6. Research Gap And Motivations

A review of studies in the literature reveals that obtaining different channel geometries with existing channel formation methods is quite difficult and time-consuming. Therefore, the effects of channel geometry on mechanical properties have generally been addressed only limited way, and almost all studies have used circular cross-section channels. While different channel geometries (circular, square, rectangular, etc.) have been evaluated in numerical analysis studies for optimal thermal designs, no studies in the literature have experimentally investigated the effects of these geometries on the impact and flexural strength of the material.

This thesis aims to address this deficiency by experimentally investigating the impact and flexural performance of different channel geometries (circular, square, hexagonal, and star) on CFRP composites. The results obtained are expected to contribute to the determination of the most suitable channel geometry under different operating conditions and serve as a reference for future research.

In addition, the cross-sectional areas of the channels created in this study are larger than those in previous studies, which is another factor that makes the research special. Findings from the tests show that thermal management studies in composite materials can be further accelerated thanks to the new channel formation method used in the production process.

3. MATERIAL AND METHOD

This section will detail the production process of carbon fiber reinforced composite specimens with different channel cross-sectional geometries, the materials used in the experimental study, the channel formation methods, and the mechanical tests performed. Experimental design is based on an innovative production approach (Geren N, 2024; Koştur et al., 2025; N., 2024) developed by taking into account the knowledge gaps identified in the literature and the limitations of existing production methods. In this context, in order to examine the effect of channel geometry on the impact and bending behaviour of the composite material as accurately as possible, all production and test parameters were kept as constant as possible. Thus, the aim was to obtain comparable results between specimens with different channel cross-sections.

3.1. Materials

In this thesis study, carbon fiber reinforced polymer composite (CFRP) laminates were prepared for the production of test specimens with different channel geometries. An epoxy-based polymer matrix and carbon fiber fabric reinforcement material were used in the production. To create channels with different cross-sectional geometries within the CFRP laminates, polyamide monofilaments in various geometric shapes were selected.

To ensure that each channel form can be integrated into the structure accurately and reproducibly, special moulds were designed and manufactured for low velocity drop weight impact (DWI) and 3 point bending tests. Using this method, it has been possible to obtain laminates with a more uniform channel distribution and equivalent properties. During production, the necessary tolerances were taken into account to ensure that the channels to be opened on the moulds could be created to suit each geometric shape, and different profile cutters were designed accordingly. Using these cutters, channels specific to each channel geometry were machined onto the surface of the moulds with high precision and accuracy.

3.1.1. Carbon Fabric

In this study, carbon fiber fabric with a twill weave structure was selected as the reinforcement material in the production of CFRP composite structures due to its balanced performance in terms of strength, flexibility and surface aesthetics. These fabrics were supplied by kompozitshop. Table 3.1 indicates the physical and mechanical properties of the fabric used in this study.

Table 3.1. Physical and mechanical properties of twill carbon fabric

Property	**Value**
Fabric type	2/2 Twill weave, bidirectional carbon fiber fabric
Fiber type	Carbon fiber – 12K (PAN-based)
Areal weight	400 g/m² ±5%
Thickness	~0.40 – 0.45 mm (nominal value, typical for 400 g/m² twill)
Density	1.79 g/cm³
Tensile strength	4900 MPa
Tensile modulus	230 GPa
Elongation	~2.0 %
Yarn density (warp/weft)- Thread count (warp/weft)	25/25 ends per 10 cm
Weight ratio (warp/weft)	50% / 50%

3.1.2. Polymer Matrix

In this project, the matrix material used is an epoxy polymer resin (MGS LR160) and its hardener (LH160), produced by Hexion, which has proven itself over many years. This material possesses superior mechanical properties and is widely used worldwide in the manufacture of advanced civil aviation composite parts. It is certified by the German Federal Aviation Authority. These fabrics were supplied by kompozitshop.

Table 3.2 Chemical and physical properties of epoxy resin and its hardener

Property	**Epoxy Resin**	**Hardener**
Product brand description	**MGS LR160**	**MGS LH160**
Viscosity (mPas) at 25 °C	700-900	10 – 100
Density (gr/cm³) at 25 °C	1.13-1.17	0.93 – 100

Table 3.3 Physical and mechanical properties of the matrix

Property	**Matrix**
Mixed products	MGS LR160/ MGS LH160
Mixing ratio by weight	100:25
Viscosity at 25 °C	1300 – 1600 mPas
Density at 25 °C	1.17 gr/cm³
Operating temperature	-60 °C / +40 °C (without heat treatment) -60 °C / +70 °C (with heat treatment)
Process temperature	+10 °C / +50 °C operating range
Working time (pot life)	40-50 minutes (depending on ambient temperature)
Tensile stress	55-65 MPa (at 80 °C and 8 hours later)
Tensile Modulus	2400-2700 MPa (at 80 °C and 8 hours later)
Bending stress	90-105 MPa (at 80 °C and 8 hours later)
Flexural Modulus	2400-2600 MPa (at 80 °C and 8 hours later)

3.1.3. Polyamide (PA 6) Monofilaments

Polyamide (PA 6) monofilaments were chosen as temporary (removable) elements for the creation of internal channels. Their high temperature resistance (up to 180°C), dimensional stability, and low surface interaction with the epoxy resin were key factors in selecting this material. Polyamide maintained its geometric form throughout the curing process under hot pressure, ensuring the channel shape remained intact.

Following the curing process, polyamide exhibited a higher tendency to shrink during the cooling phase due to its higher thermal expansion coefficient compared to the epoxy matrix. This different shrinkage behavior reduced the adhesion at the interface between the polyamide and epoxy, allowing the monofilaments to be easily mechanically removed. This resulted in channels with high continuity and uniformity within the laminate. Furthermore, the availability and low cost of polyamide monofilaments offered a reproducible and economical solution for laboratory-scale production.

The selection of polyamide monofilaments is critical for accurately comparing the effects of different channel geometries on mechanical behavior. Therefore, as shown in Table 3.4, care was taken to determine the channel cross-sectional areas as close as possible to each other. In addition, the channel perimeter (P) and the perimeter-to-area ratio (P/A) were calculated and reported to quantify how boundary length per unit area varies with geometry, which is also relevant for surface-dominated functional considerations such as heat transfer. However, at the beginning of the study, it was intended to supply star-shaped monofilaments with a diameter of 4 mm, but since these were not available in the suppliers' stocks, star-shaped monofilaments with a diameter of 3.3 mm were used.

This could have resulted in the cross-sectional area of star-section channels being smaller than other geometries, making comparability somewhat difficult. Also, the successful production of star channels, one of the most geometrically complex cross-sections, is an important indicator of the repeatability, applicability, and sustainability of the production method employed in this study. Figure 3.1 shows cross-sectional views of the polyamide filaments used to create channels for a better understanding of the different channel geometries.

Table 3.4. Geometrical properties and cross-sectional areas of micro-channel types used in the study

Channel Geometry	Representative Geometry	Section Area (mm^2)	Channel Perimeter (P, mm)	Perimeter to area ratio (P/A) (mm^{-1})
Circular	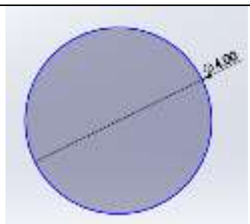	12.56	12.57	1.0007
Hexagonal	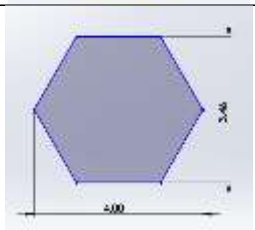	10.39	12.12	1.16
Square	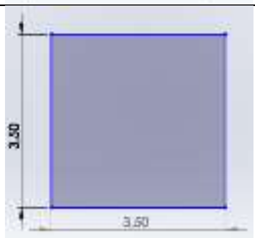	12.25	14	1.14
Star	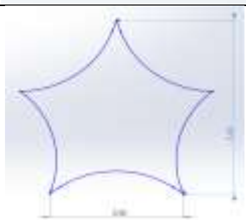	5	11.39	2.278

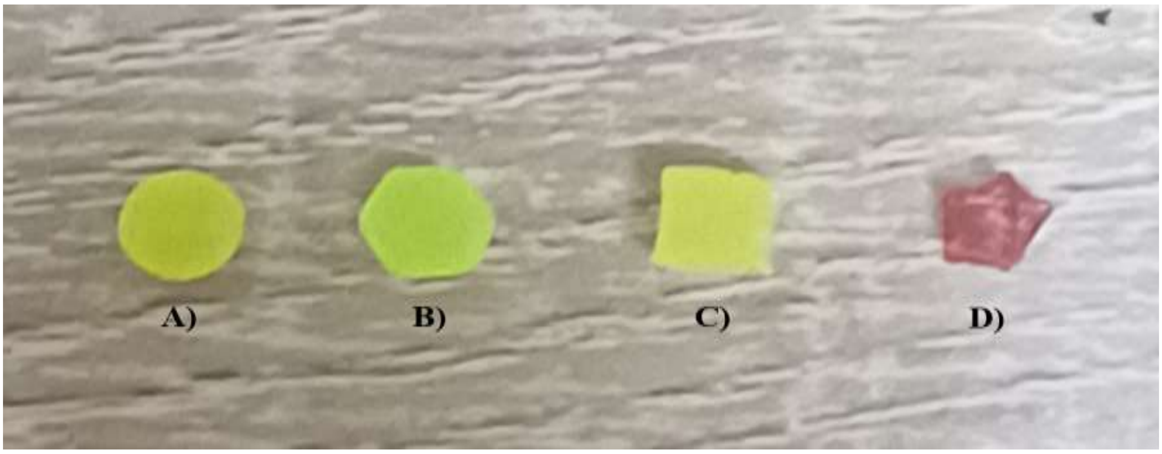

Figure 3.1. Cross-sectional geometries of polyamide (PA-6) monofilaments used to creating embedded micro-channels, (A) circular, (B) hexagonal, (C) square, and (D) star-shaped

3.1.4. Profile Cutter and Molds

The molds made from medium-density fiberboard (MDF) used in this study were machined using profile cutters and each of them specifically designed according to the channel geometries to be used in the study. These cutters (Figure 3.2) were manufactured to precisely replicate the cross-sectional form of the channels (circular, hexagonal, square, star shaped) on the mold surface. The use of such specialized tools ensured high dimensional accuracy, uniform channel distribution, and repeatability during the molding process, resulting in consistent CFRP laminates with integrated microchannels.

Figure 3.2. Profile cutters used for machining channels on surface of the molds: (a) circular, (b) hexagonal, and (c) square. All cutters are made of solid carbide material, selected for their high hardness and wear resistance during mold machining

Thanks to this special molds, after polyamide-based monofilaments were placed between carbon fiber layers, and moulds designed to match the geometry of the monofilaments were placed on the laminate under hot press. This ensured that the channel form was incorporated more effectively and evenly into the composite structure.

The greatest challenge encountered in this section is the production of suitable moulds for creating star-shaped channels. Both the processing of such a mould and its subsequent use under pressure without damaging the laminate has a high risk in terms of production. To overcome this difficulty, a new mould design that has circular cross-section channels (diameter= 3 mm) of appropriate dimensions was preferred over star-shaped channels.This ensured that the resin completely filled the tips of the star shape and that no voids remained in the laminate after production. Figure 3.3 shows the section view of each mould, while Figure 3.4(a-c) presents their three-dimensional CAD models.

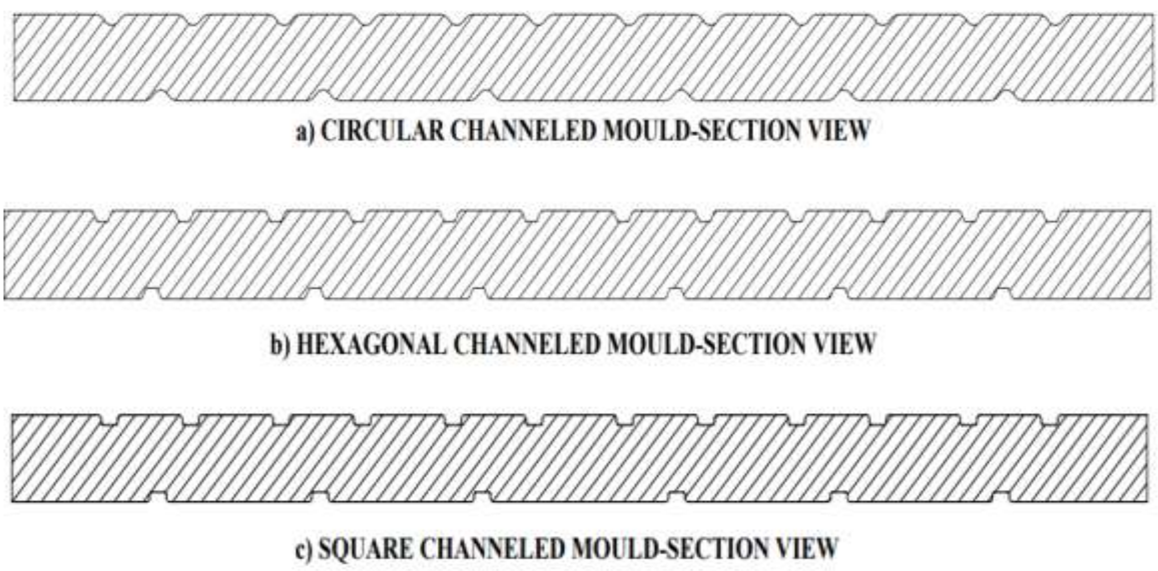

Figure 3.3. Cross-sectional views of the moulds with different channel geometries: (a) circular, (b) square, (c) hexagonal (While upper side of the mold are used during the manufacturing of the bending test specimens, otherside are used to manufacturing of the impact test specimens.)

(a) 3-D Circular channel mould.

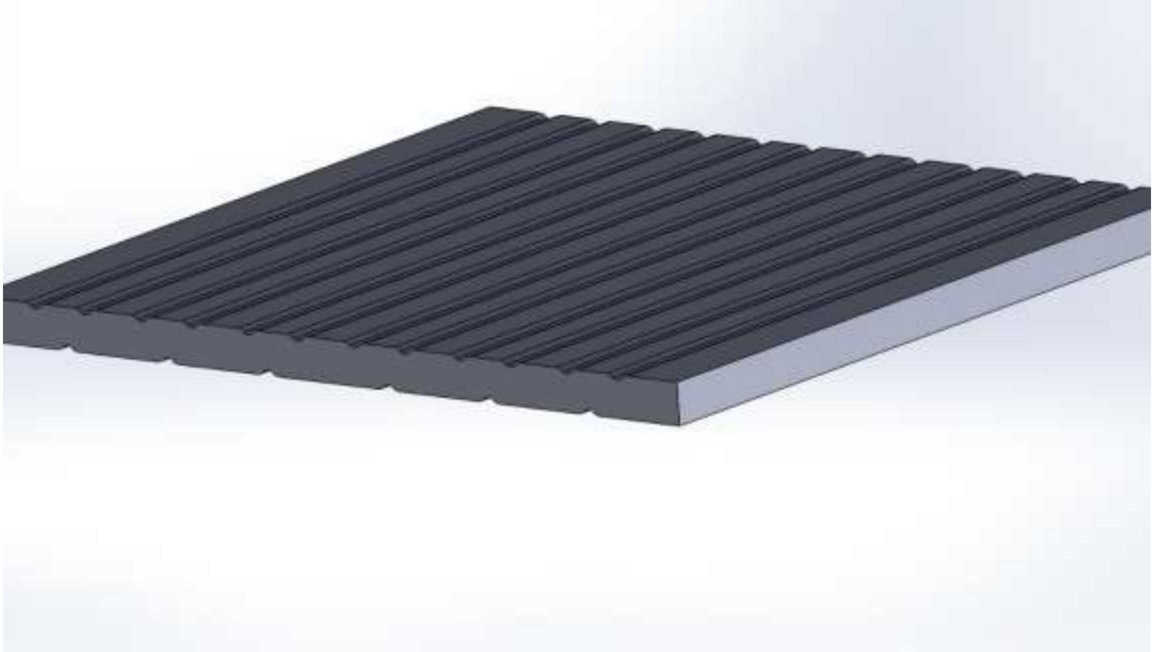

(b) 3-D Hexagonal channel mould.

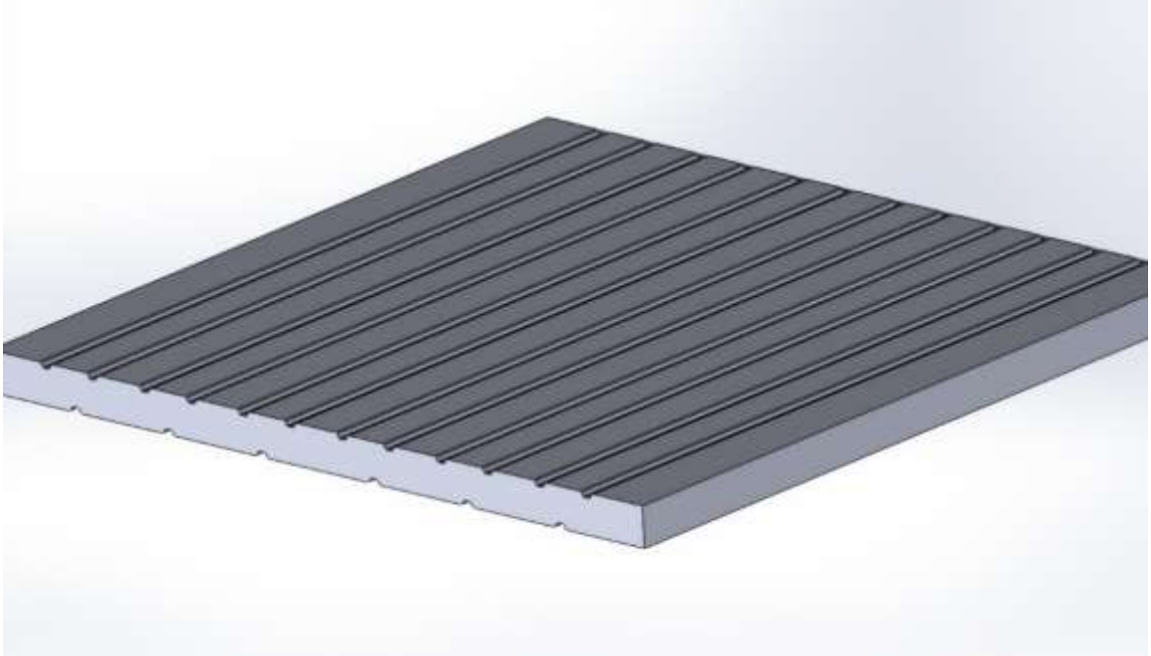

(c) 3-D Square channel mould.

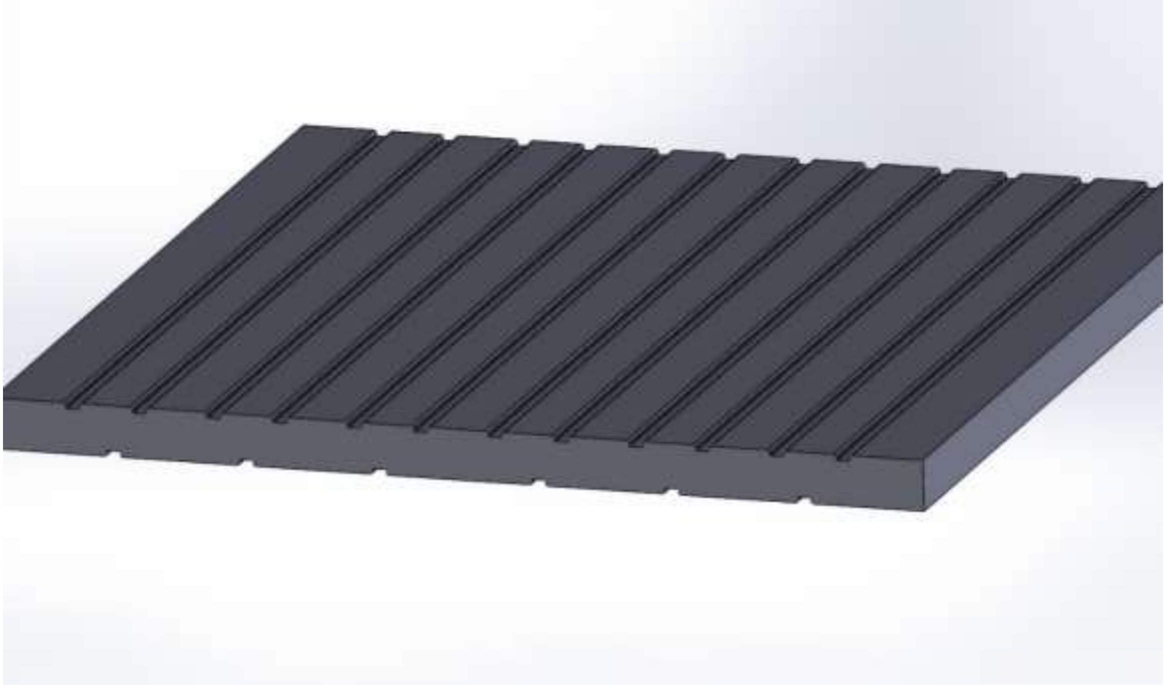

Figure 3.4. Three-dimensional views of moulds with different channel geometries: (a) circular, (b) hexagonal, and (c) square. Mould dimensions (Designed at Solidworks) are 350x350x25 mm

3.1.5. Consumables

Table 3.5. Consumable materials used during the manufacturing of CFRP laminates and their properties

Name of Consumable	Property	Supplier	Purpose of Using
Vacuum Nylon	Stands up to 110 °C Thickness: 75 µm	Kompozit Shop	To create a controlled working area
Polivaks Max-9	Stands up to 200 °C	Dost Kimya	To ease of removal of monofilaments from the laminate by coating the monofilaments
Air Intake Roller	Plastic Handle 18x100mm	Kompozit Shop	Removing air and voids between the fiber layers
Epoxy Mixing Cups and Brushes	Disposable plastic, solvent-resistant	Local supplier	For mixing and applying epoxy resin and hardener

3.2. Production Method

This section describes the experimental procedures applied for the production and testing of channelled carbon fiber reinforced polymer (CFRP) composite specimens with different microchannel cross-sectional geometries. The methods followed in the study were designed to enable the direct comparison of the effects of channel geometry on mechanical performance by ensuring that each specimen was prepared under the same production and testing conditions.

This section consists of the CFRP sample production process, the preparation of test specimens, impact and bending test procedures, and data analysis. Each stage of the experimental work has been carefully optimised to obtain repeatable results with minimal variability. All procedures were performed in accordance with the relevant ASTM standards (ASTM D790 for three-point bending tests, ASTM D7136 for impact tests).

3.2.1. Manufacturing of Channelled CFRP Laminate

Carbon fiber reinforced polymer (CFRP) laminates with microchannels were produced using a controlled hand lay-up and curing method under hot press (Figure 3.5). The primary objective of production was to investigate the effect of channel cross-section geometry on mechanical performance by keeping all parameters constant except for the channel geometry. All laminates were prepared using 400 g/m² twill-woven carbon fabric and an epoxy resin system (MGS L160/H160), with a resin/hardener ratio of 100:25 (by weight). The curing process was carried out under controlled temperature and pressure. The total weight of the epoxy resin used during production was determined to be equal to the weight of the reinforcement fibers, thereby maintaining a constant resin/fiber ratio in each laminate. To create the microchannels, polyamide monofilaments with defined cross-sectional geometries were placed between predetermined layers prior to curing. The curing process was carried out under controlled temperature and pressure. Subsequently, these monofilaments were removed, resulting in continuous and uniform channels without damaging the surrounding laminate. Throughout the production process, dimensional repeatability, homogeneous resin distribution, and minimisation of void content were targeted.

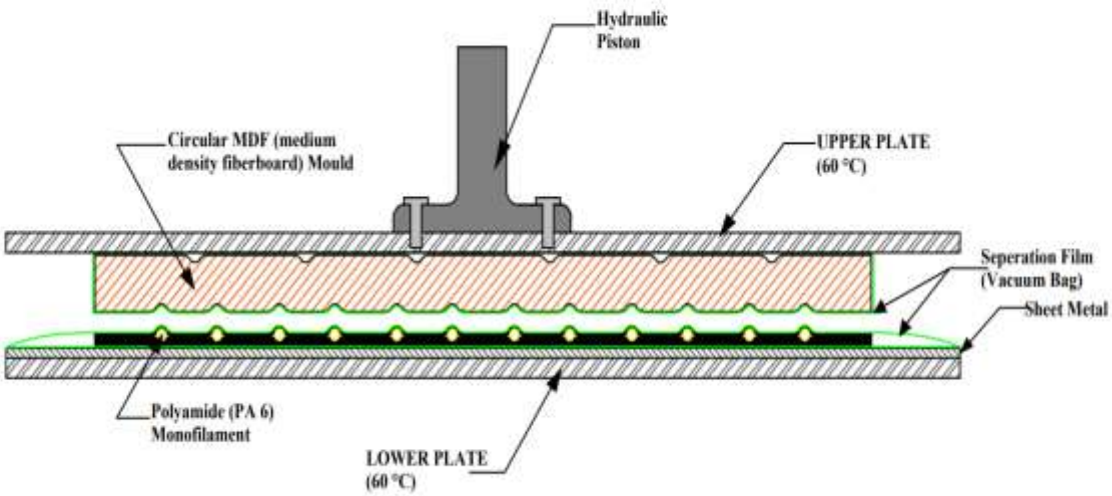

Figure 3.5. Schematic representation of the curing arrangement for a circular channelled CFRP laminate under hot press

This diagram shows the arrangement of the MDF (medium-density fibreboard) mould, separator film (vacuum bag) and polyamide (PA-6) monofilaments positioned between the upper and lower heating plates (60 °C). The pressure applied by the hydraulic piston was transferred homogeneously to the surface of the laminate, ensuring the uniform curing of the resin-impregnated carbon fiber layers. This arrangement allows the channel geometry to be maintained within the mould, enabling the formation of continuous microchannels within the laminate. Only the MDF moulds were changed depending on the channel cross-section geometry of the laminate to be produced, while all other production parameters were kept constant.

Mould Design and Production

In the production of channelled CFRP laminates, the mould design was carefully carried out in a three-dimensional design programme (*SolidWorks 2023*) to achieve a smooth surface quality and ensure that the channel geometry is formed completely within the laminate as designed. In this context, special cutting blades (profile blades) suitable for each channel geometry were designed and manufactured, taking into account the channel cross-section type, channel diameter, separation film thickness, and mould clearance tolerances.

Before machining the moulds, they were positioned on their side surfaces with support plates (fixtures) to ensure stability during production. Using these blades, moulds with different channel geometries to be evaluated in the study were machined with high dimensional accuracy on the CNC Router bench from medium-density fibreboard (MDF) based material (Figure 3.6). This method enabled repeatable and reliable mould production by controlling the geometric accuracy and surface roughness of the channel bearings.

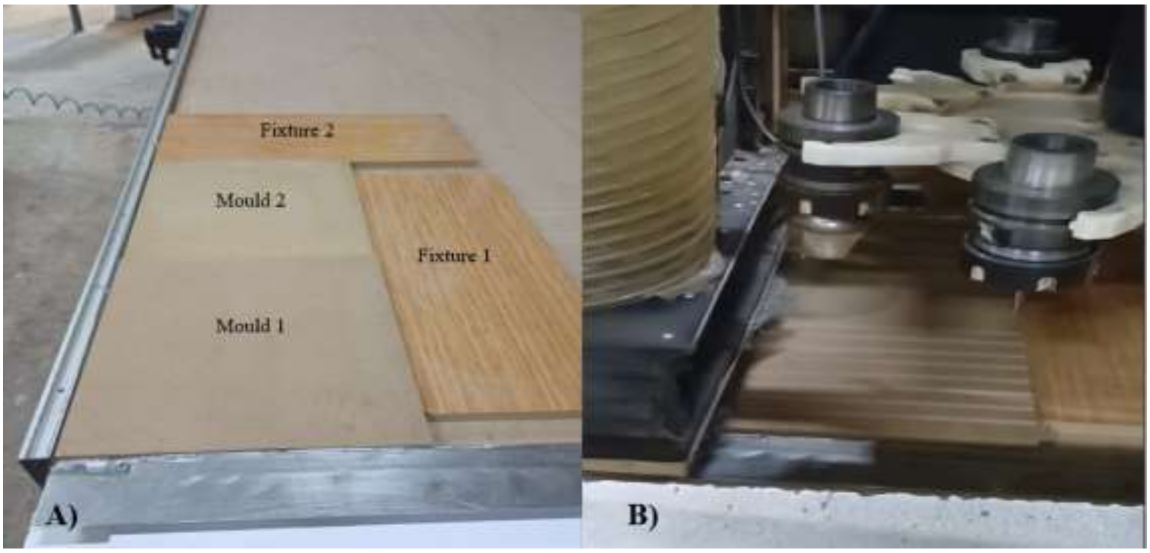

Figure 3.6. (A) Positioning of MDF mould and fixture plates, (B) Machining stage of channel geometries on the CNC Router bench

Additionally, the mold surface was coated with a nylon-based release film before production to prevent the epoxy resin from adhering. This practice ensured that the laminates were removed from the mold without damage after curing, preserving their surface integrity. Throughout the production process, the mold served as both a geometric guide and a structural support element.

Furthermore, channel bearings pre-machined to match the microchannel cross-sectional geometries ensured repeatability of the channel shape, ensuring that the polyamide (PA-6) monofilaments maintained their position and alignment under the applied pressure and temperature conditions during hot pressing.

Manufacturing and Lay-up of CFRP Laminates

Before starting the hand lay-up lamination process, carbon fiber fabrics were pre-prepared in accordance with relevant ASTM standards and channel spacings to ensure that samples for each test group could be prepared in a single production run and to minimize material waste. Carbon fabrics were cut to dimensions that would allow for the production of a total of six samples (Five primary test samples and one spare sample) for each test group (335 mm × 335 mm for bending tests and 335 mm × 375 mm for impact tests). Each laminate was constructed from ten (10) layers in accordance with the specified fiber layout. Figure 3.7 shows that preparation of twill carbon fabric layers for impact and bending specimens before lamination.

Figure 3.7. Preparation of twill carbon fabric layers for impact and bending laminates

Before starting the lamination process, a nylon-based release film (vacuum bag) was fixed to the sheet metal using double-sided tape to ensure a controlled working environment and a smooth, clean contact surface. This film prevented any resin leakage from the laminate edges during the pressing phase, allowing the samples to be easily removed from the mold after curing without causing surface damage (Figure 3.8).

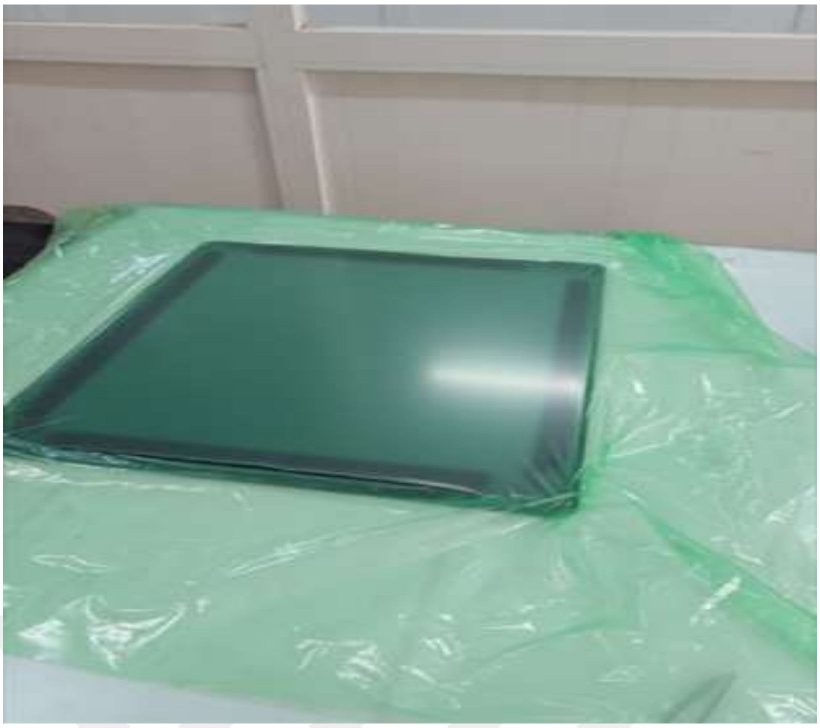
Figure 3.8. Nylon-based separation film applied to the MDF mould surface

During the lamination process, eight layers of carbon fabric were carefully and sequentially placed on a mold surface covered with a release film. Each layer was impregnated with a pre-prepared epoxy resin mixture, ensuring complete wetting of the fibers (Figure 3.9). The resin was spread evenly over the fiber surface using a plastic applicator, ensuring complete penetration of the matrix into the fabric and the formation of a strong bond between the layers. All layers were stacked, maintaining the original orientation of the fabric roll, ensuring consistent fiber orientation throughout the laminate. The layer arrangement was arranged in a symmetrical $[(0/90)]_{5s}$ configuration, providing balanced, quasi-isotropic in-plane rigidity. A de-airing roller was used during each layer placement step to eliminate air bubbles and ensure complete resin impregnation of the carbon fabric. This careful lamination process ensured uniform resin distribution between the layers, maintaining a smooth surface finish and structural integrity before pressing.

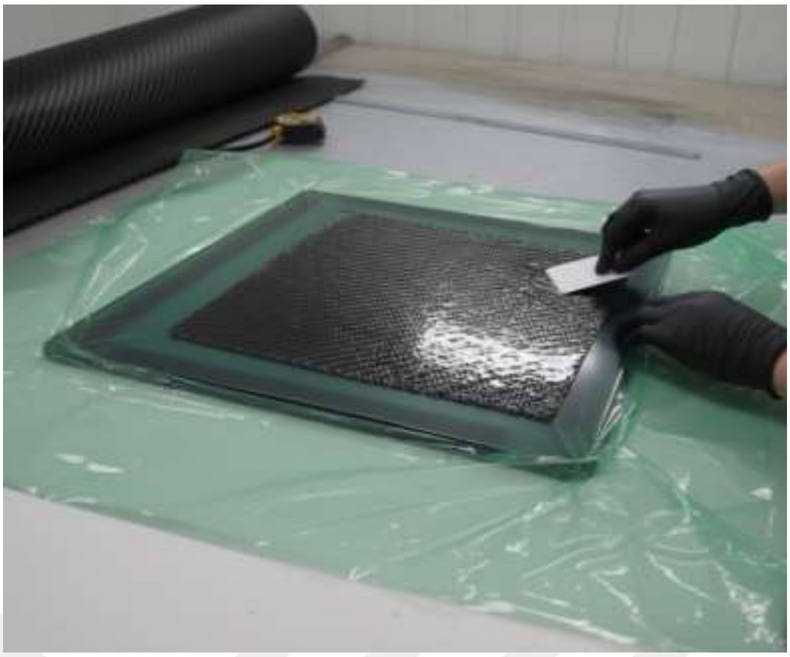

Figure 3.9. Hand lay-up process during lamination

Placement of Polyamide Monofilaments

This stage is one of the most critical production steps, physically defining the channel geometry for the creation of microchannels within the composite laminate. Polyamide (PA) monofilaments were used as temporary elements that would be removed after curing, leaving continuous channels in their place. Therefore, the correct, stable, and even placement of the monofilaments is crucial for channel continuity, geometric accuracy, and inter-sample reproducibility.

In order to prevent displacement of the monofilaments during the lamination and hot pressing processes, a wooden frame was used. Ends of the monofilaments gently crushed and flatten with a hammer and then fixed with nails on the wooden frame (Figure 3.10). This method kept the tension of the filaments constant and ensured that the channel direction and the distance between the channels were maintained throughout the production.

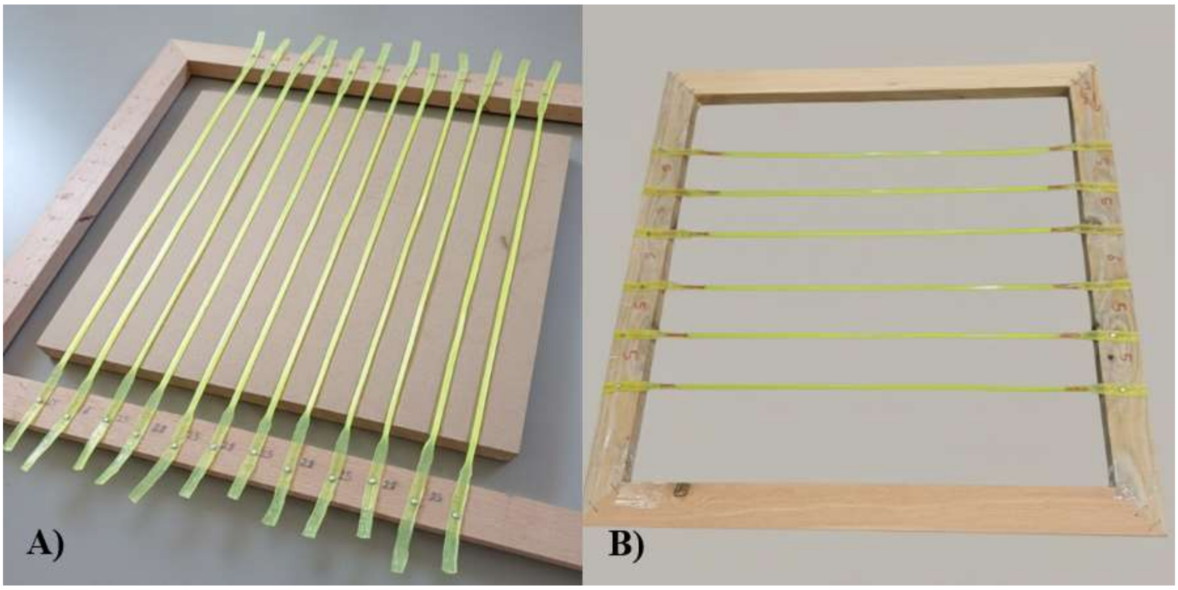

Figure 3.10. (A) The position of the polyamide (PA-6) monofilaments fixed to the fixing frame by stretching them for the bending test samples, (B) The position of the monofilaments fixed to the fixing frame by stretching them for the impact test samples

Channel spacing and alignment measurements were determined based on the channel spacing and sample dimensions determined for the test groups. Thus, in all samples produced for impact and bending tests, channels were created at the same location and spacing for each group, only the channel cross-sectional geometry was used as a variable.

After placing the monofilaments, the final two carbon fabric layers were placed sequentially on the mold, taking care to maintain fiber orientation and layer alignment during this step. Following completion of the lamination, the moulds, processed to suit the channel geometry, were carefully placed (Figure 3.11.) on top of the laminate to preserve the shape integrity of the channels. This ensured that the channel bearings of the moulds and the monofilaments were aligned precisely, ensuring the channel geometry within the laminate was fully formed as designed.

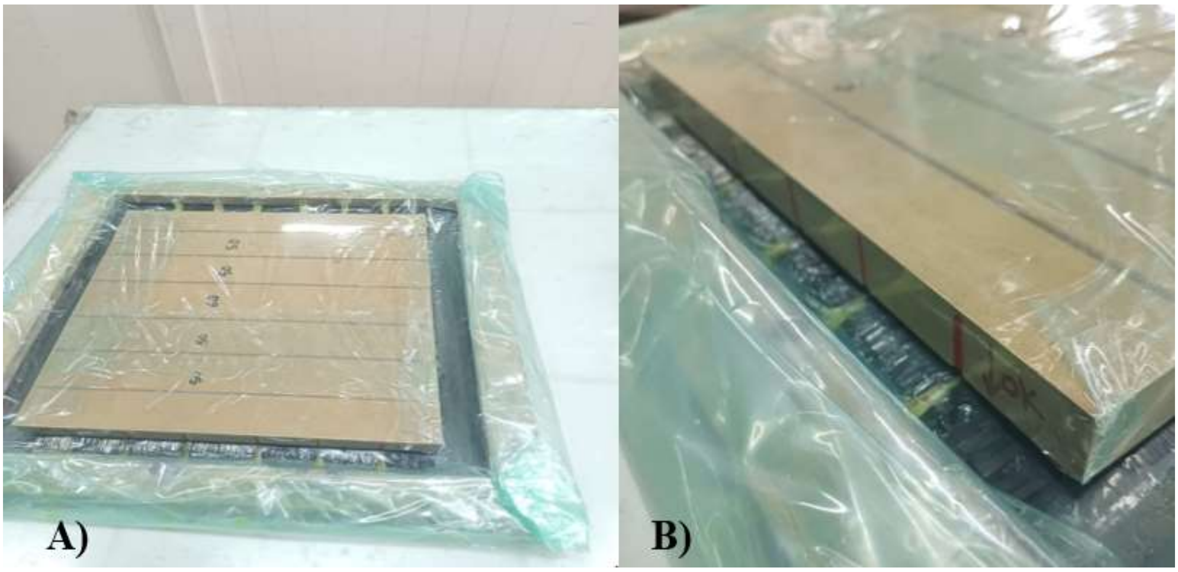

Figure 3.11. (A) Laminate that has completed lamination and is ready to enter the press, (B) Side view of the MDF mould and polyamide monofilament placement prior to pressing

Curing Process Under Hot Press

Composite samples, whose preliminary preparation was completed using the lamination (hand lay-up) method and into which polyamide monofilaments were embedded, were produced by placing them in a laboratory-type hot hydraulic press machine equipped with temperature and pressure control systems for the final curing and moulding process. The upper and lower heating plates of the press ensured homogeneous heat and pressure distribution across the laminate surfaces throughout the production process. This method is preferred for the production of composite parts with superior mechanical properties, high fiber volume fraction, and low void (porosity) ratio.

The process was completed in the following steps:

Placement**:** The sample, which had been laminated on a thin sheet metal plate, completely impregnated with resin and containing polyamide monofilaments, was carefully positioned between two heating plates (Figure 3.12.A). During pressing, an additional MDF plate was placed on top of the mould to ensure that the applied pressure was transmitted homogeneously to the laminate surface. Without this plate, the press load would act directly on the frame surrounding the mould, and the pressure distribution within the mould cavity would not be homogeneous. The MDF layer therefore acts as a mechanical intermediate layer, ensuring that the effective pressure is directed directly onto the laminate.

Figure 3.12. Curing process of CFRP laminates under hot press. (A) Placement of the prepared laminate between heated press plates prior to curing. (B) Curing process performed by applying hydraulic pressure and temperature in a laboratory-type hot press device

Pressure and Curing Application: The curing process was carried out at 60 °C, for 4 hours and under an effective pressure of 3 bar (≈ 0.3 MPa) by taking the studies in the literature as reference for the MGS L160/H160 epoxy system (Figure 3.12.B). These parameters ensured complete polymerisation of the resin, sufficient resin flow, and strong interlayer bonding, while allowing the designed microchannel geometry to be maintained. The applied pressure ensured the removal of trapped air bubbles within the material and the preservation of the positions of the polyamide (PA 6) monofilaments that would form the channels. This prevented the formation of voids and delamination within the laminate. After curing was completed, the laminates were removed from the press and the samples could be easily removed from the mold without damaging their surfaces thanks to the nylon separator film.

To achieve the desired 3-bar effective pressure (P_e) on the laminates, the required hydraulic pressure (P_h) was calculated by taking into account the surface area of the press piston (A_p) and the area of contact between the laminate and the press plates (A_c) (Table 3.6). The ratio of the applied pressures can be expressed using the following equation, based on the principle of force balance.

$$\mathbf{P_h \times A_p = P_e \times A_c} \tag{3.1}$$

$$P_h = P_e \text{ x } \left(\frac{A_c}{A_p}\right) \tag{3.2}$$

Where,

- P_h: hydraulic pressure (bar or MPa)
- P_e: effective pressure on the laminate (≈3 bar)
- A_p: area of the press piston (m²)
- A_c: contact area between the laminate and the press plates (m²)

Table 3.6. Calculation of the hydraulic and effective pressure values applied during the hot press curing process for bending and impact laminates

Test Category	**Dimension of the Laminate (mm)**	**Contact Area (A_c) (m²)**	**Piston Diameter (mm)**	**Piston Area (A_s) (m²)**	**Hydraulic Pressure (P_h) (bar)**
Bending	335 × 335	0.1122	75	0.004418	72
Impact	335 × 375	0.1256	75	0.004418	80

Under the applied pressure, the resin flowed between the carbon fiber layers and formed resin-rich regions around the embedded polyamide (PA 6) monofilaments (Figure 3.13). These regions ensured complete encapsulation of the filaments and enhanced interlayer adhesion. Temperature and pressure values were continuously monitored throughout the curing cycle to maintain process stability. This controlled hot press curing procedure ensured that all samples had a consistent thickness, uniform surface quality, and highly repeatable internal channel geometry.

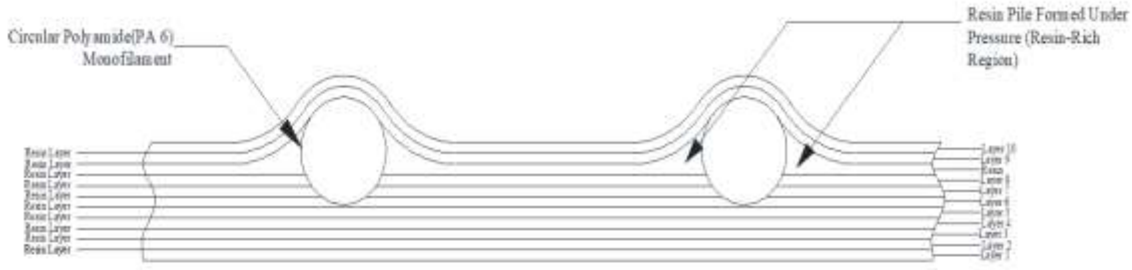

Figure 3.13. Schematic representation of polyamide (PA 6) monofilaments and resin-rich regions placed to create circular cross-section channels

Demoulding and Removing of the Monofilaments

After the curing cycle was completed, the laminates were carefully removed from the mould by reducing the pressure applied to the press (Figure 3.14). The nylon-based release film ensured that the samples were demoulded cleanly without any surface damage or edge deformation (Figure 3.15). Following demolding, the laminates were slowly cooled to room temperature under reduced pressure to facilitate easier removal of the monofilaments from the laminates.

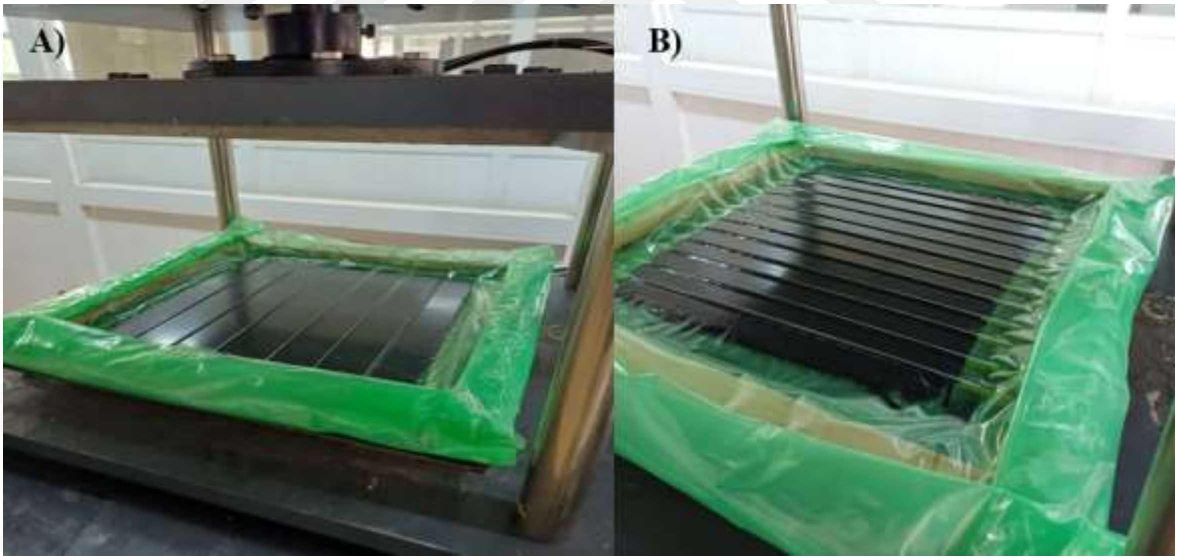

Figure 3.14. (A) Impact test laminate with square-section channels after curing, (B) Appearance of the bending test laminate with star-section channels after curing

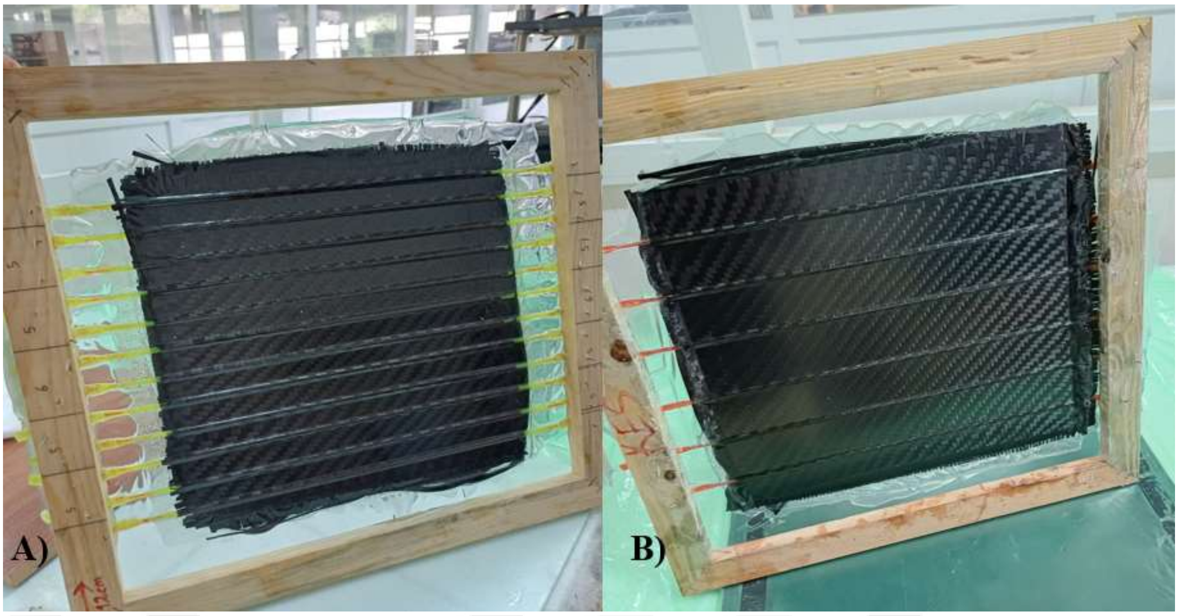

Figure 3.15. (A) Appearance of the bending test laminate with square cross-section channels after demoulding. (B) Appearance of the impact test laminate with star-shaped cross-section channels after demoulding

Following the cooling process, the polyamide (PA 6) monofilaments within the laminates were mechanically removed (Figure 3.16). Due to PA 6 having a higher thermal expansion coefficient compared to the epoxy matrix, it exhibited a greater tendency to shrink during cooling. Although this slightly increased the friction resistance during removal, it reduced the adhesion at the interface, allowing the filaments to be pulled cleanly without damaging the channel walls.

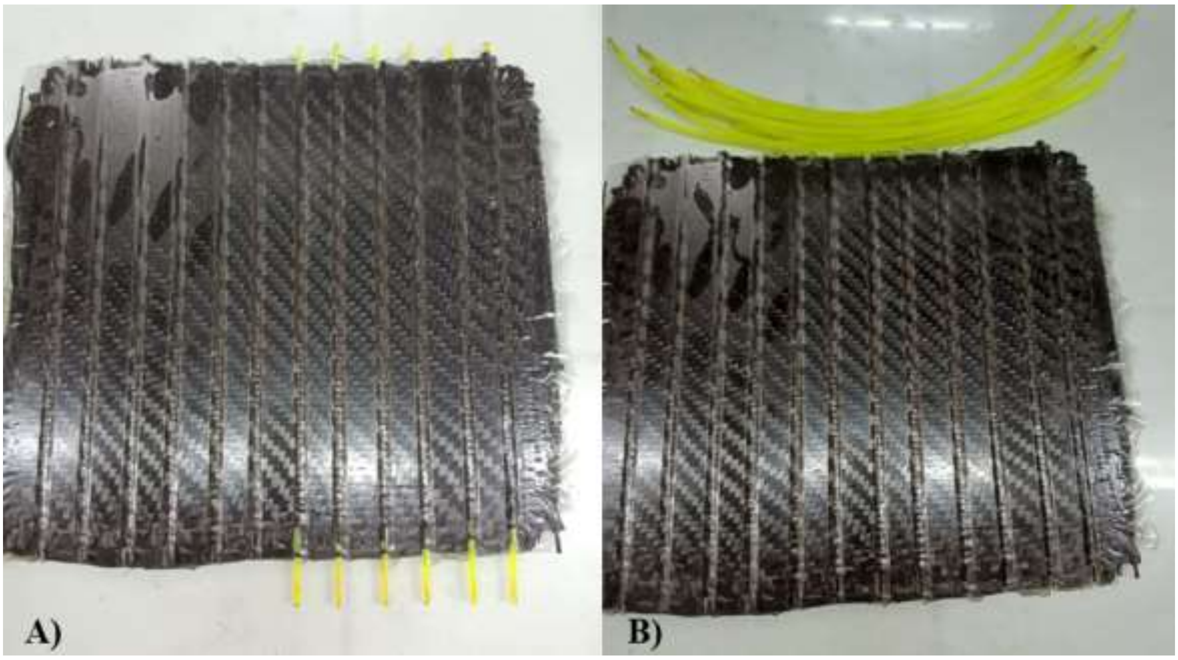

Figure 3.16. (A) Bending test laminate with square-section channels still containing polyamide (PA-6) monofilaments after curing, (B) Appearance of the laminate with square channels obtained after removal of the monofilaments

3.2.2. Preparation of the Test Specimens

Following the curing and demoulding stages, the produced channelled CFRP laminates were cut into test specimens of the dimensions specified in the standards (Table 3.7) to ensure they could be used in mechanical testing in accordance with relevant ASTM standards. The primary objective of this stage is to obtain repeatable and comparable test specimens with accurate dimensions, clean edges, and a symmetrical structure (minimising deviations from the neutral axis).

In this regard, mould-like cutting templates have been designed and produced specifically for bending and impact test specimens to enable laminate panels to be cut precisely with a circular saw (t=2mm) (Figure 3.17.A). The templates were placed on the laminate surface prior to cutting to mark the cutting paths; thus, during the cutting process with the circular saw, the channel areas were not damaged, and the specimens were prepared symmetrically and reproducibly. This method contributed to obtaining more reliable and consistent test results by increasing cutting precision.

Table 3.7. Summary of specimen configurations and test parameters for flexural and impact tests

Specimen Type	**Referenced ASTM Standard**	**Monofilament Geometry and Diameter (mm)**	**Distance Between Channels (mm)**	**Number of Channels**	**Width of the Specimens (mm)**	**Length of the Specimens (mm)**	**Number of Samples Tested**
Bending Test Specimens	ASTM D790	Circular (4) Hexagonal (4) Square (3.5) Star (3.3)	25	2	≈51	Varies with span length (per ASTM D790)	25
Impact Test Specimens	ASTM D7136		50	3	150	100	25

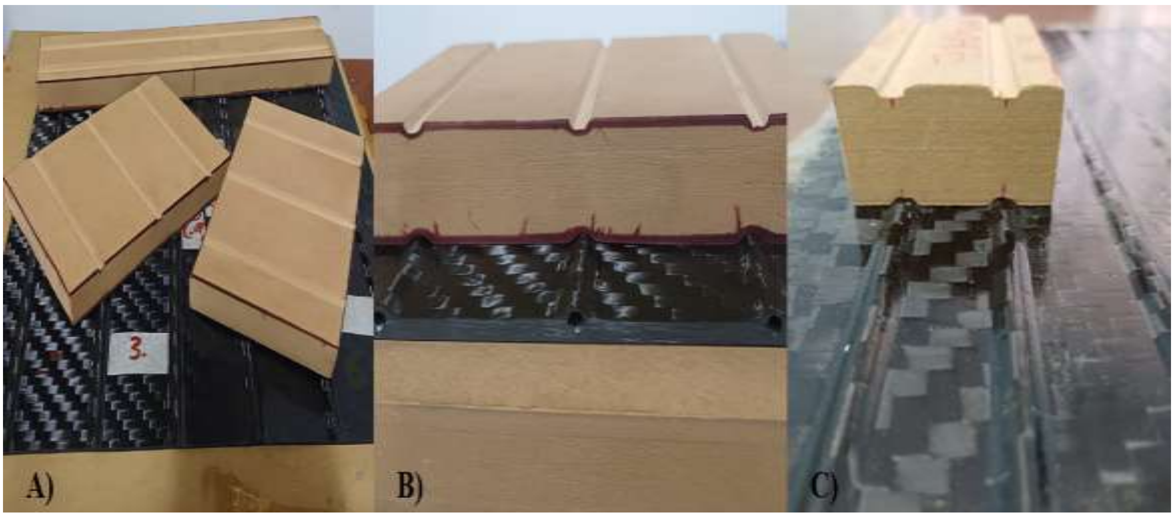

Figure 3.17. (A) Cutting templates for the bending and impact laminates produced, (B) Placing the cutting template prepared for cutting impact samples on the laminate in order to draw the cutting line, (C) Placing the cutting template prepared for cutting bending samples on the laminate in order to draw the cutting line.

3.2.3. Labeling and Coding of Specimens

Labeling of the Specimens

Before starting the cutting process, sample labelling was carried out on the prepared laminates (Figure 3.18). This stage is critical in ensuring that samples can be correctly distinguished after cutting and that the reliability of the experimental data is maintained. To ensure the traceability of each test sample, the labelling process has been standardised to include the following three key pieces of information:

- Test Type: The type of mechanical test (bending or impact) to which the sample will be subjected.
- Channel Cross-Section Geometry: The cross-sectional shape of the microchannel within the composite (circular, square, hexagonal, or star).
- Sample Sequence Number: The individual sequence number among samples with the same properties.

Labelling was carried out using solvent-resistant markers and adhesive number labels that are resistant to the chemicals used in the production and cutting processes. This method prevented the markings on the samples from being damaged after cutting, eliminated the risk of confusion, and ensured a high level of traceability throughout the entire experimental process.

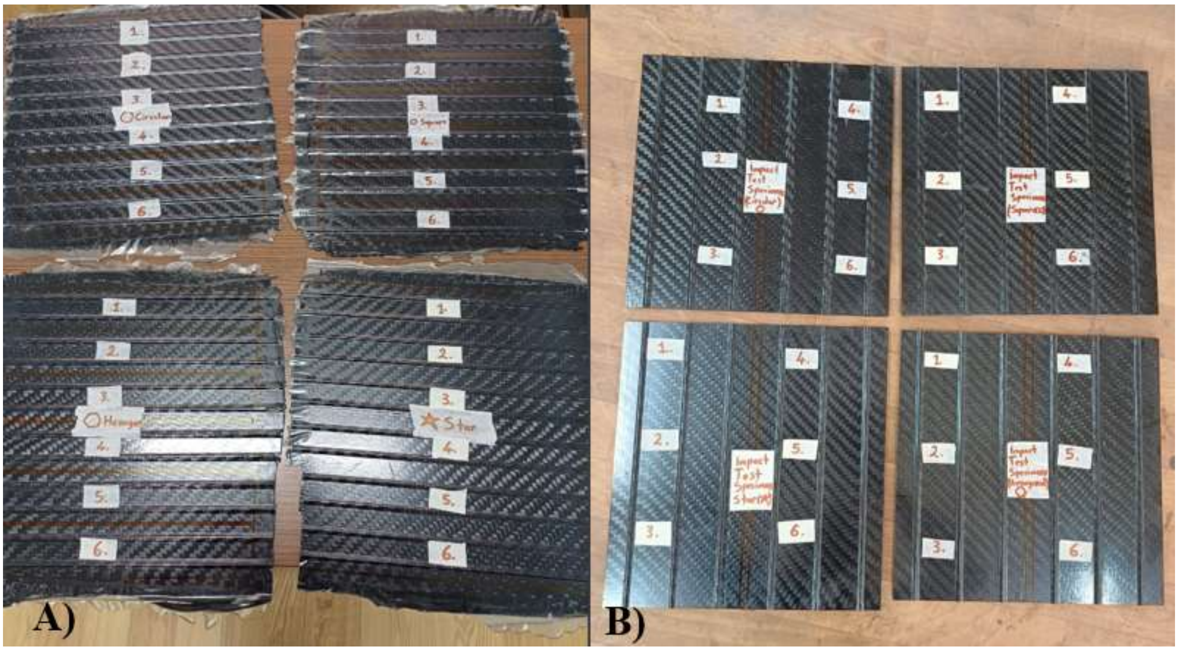

Figure 3.18. A) Labelling of bending test laminates with different microchannel geometries, (B) Labelling of impact test laminates with different microchannel geometries.

After drawing the cutting lines, the test specimens were labelled on the laminates. Each laminate was labelled according to the test type (flexure or impact), channel cross-section geometry (circular, square, hexagonal or star) and specimen sequence number. This was done to avoid specimen confusion after cutting and to ensure that the experimental data were associated with the correct specimen.

After the labeling process was completed, the samples to be used in the tests were precisely cut using a 2 mm thick circular saw and channelled test specimens with different microchannel section geometries were produced (Figure 3.19). Figure 3.20 and Figure 3.21 show the front and rear face views of the produced channelled CFRP laminates, respectively. These images clearly demonstrate the continuity and geometric integrity of the circular, square, hexagonal, and star-shaped microchannels within the laminate.

Figure 3.19. Prepared CFRP test specimens after cutting and classification according to test type (impact and bending)

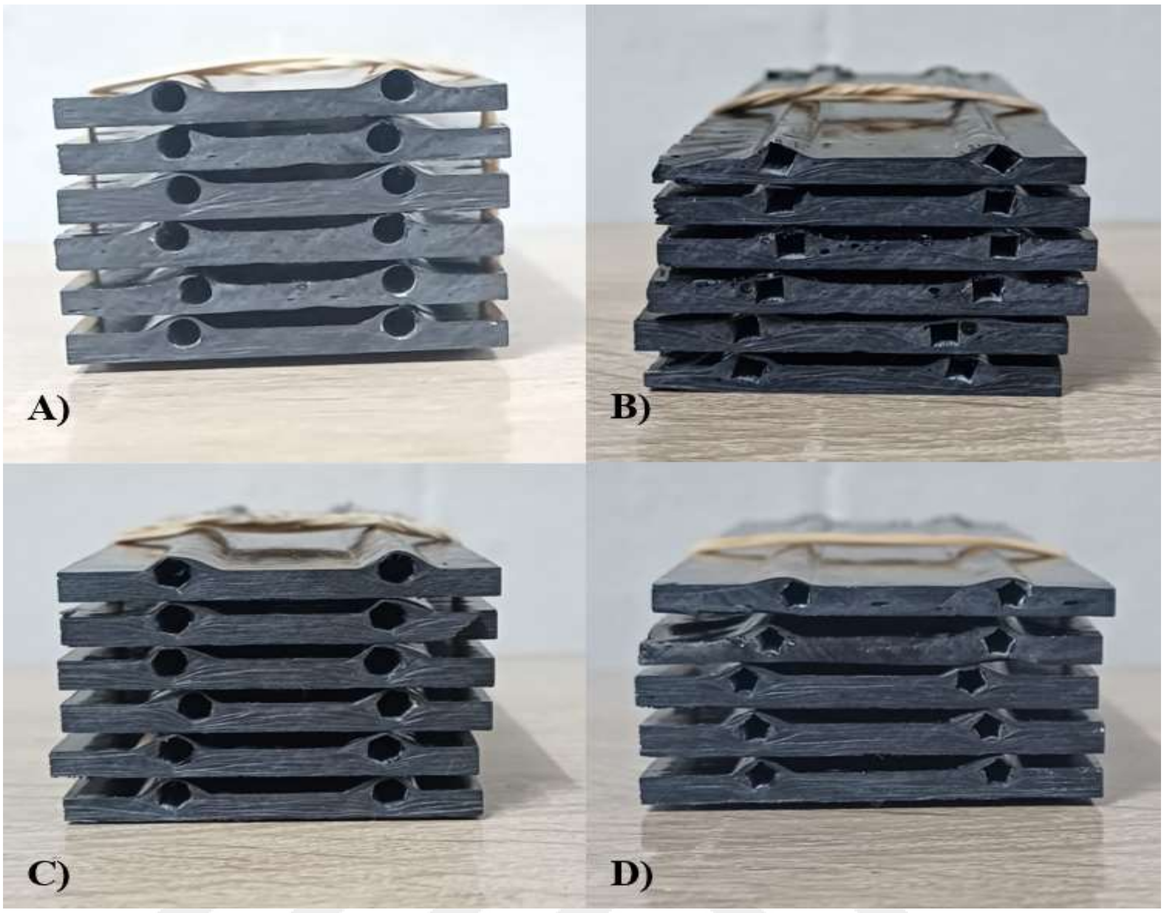

Figure 3.20. Front face views of 3 point bending test specimens with different embedded microchannel geometries ((A) Circular, (B) Square, (C) Hexagonal, and (D) Star-shaped channels.)

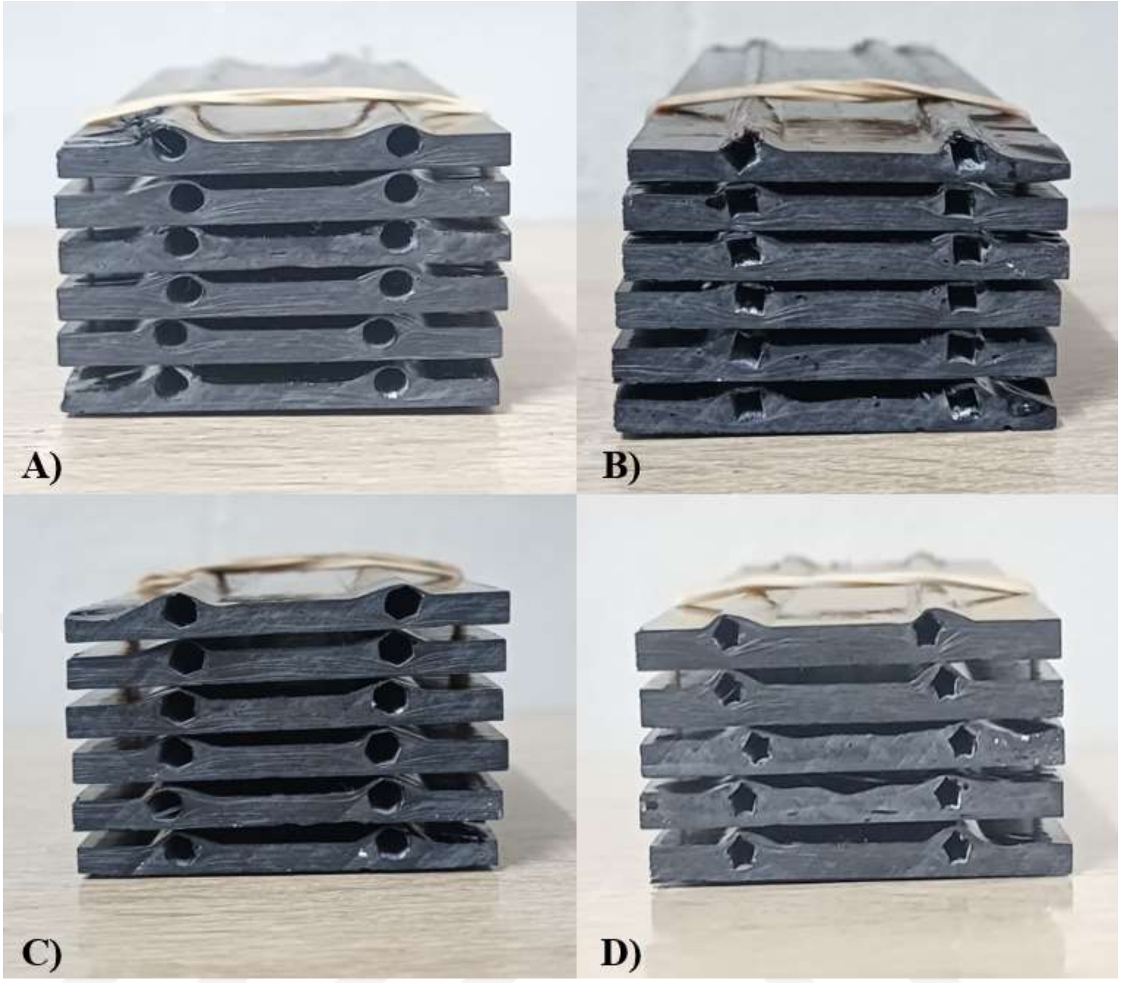

Figure 3.21. Rear face views of 3 point bending test specimens with different embedded microchannel geometries ((A) Circular, (B) Square, (C) Hexagonal, and (D) Star-shaped channels.)

These images clearly demonstrate the continuity and geometric integrity of circular, square, hexagonal, and star-shaped microchannels within the test specimens. However, partial rotations in the channel axes were observed during the production process, particularly in the square and hexagonal cross-section samples. The potential effects of these rotations on the mechanical strength of the material will be evaluated in detail in the Results and Discussion section in the following sections.

Coding of the Specimens

In this study, a standardised coding system was established to systematically identify and track each sample (Table 3.8). This system allowed the specimens to be categorised according to test type, microchannel cross-section geometry and specimen sequence number. The main purpose of the coding structure is to avoid confusion between specimens during the testing process, to facilitate data tracking and to ensure that experimental results can be reliably associated with the relevant specimen.

Table 3.8. Coding system used for test specimens

Code	Test Type	Channel Geometry	Specimen No.	Description
BT–NC–01	Bending	Non-channelled	01	Reference bending specimen without channels
BT–CC–02	Bending	Circular	02	Bending specimen with circular channels
BT–SC–03	Bending	Square	03	Bending specimen with square channels
BT–HC–04	Bending	Hexagonal	04	Bending specimen with hexagonal channels
BT–StC–05	Bending	Star	05	Bending specimen with star-shaped channels
IT–NC–01	Impact	Non-channelled	01	Reference impact specimen without channels
IT–CC–02	Impact	Circular	02	Impact specimen with circular channels
IT–SC–03	Impact	Square	03	Impact specimen with square channels
IT–HC–04	Impact	Hexagonal	04	Impact specimen with hexagonal channels
IT–StC–05	Impact	Star	05	Impact specimen with star-shaped channels

3.3. Mechanical Testing Methods

The mechanical performance of manufactured CFRP laminates containing embedded microchannels has been experimentally evaluated using standardised bending and impact tests. These tests were designed to quantitatively determine the effect of channel cross-sectional geometry on the load-carrying capacity, stiffness, and energy absorption properties of composite structures. All specimens were prepared by keeping the fiber orientation, layer sequence, curing conditions, and resin/hardener ratio constant, thus ensuring that only the channel geometry remained variable.

Two different test methods were applied in this experimental study: a three-point bending test in accordance with the ASTM D790 (International, 2015) standard and a low velocity drop weight impact (DWI) test in accordance with the ASTM D7136 (International, 2020) standard. In the bending tests, the channels were positioned parallel to the long side of the specimen; thus, the flexural strength and elastic modulus under static loading were evaluated. In contrast, in the impact tests, the channels were aligned parallel to the short side to investigate the energy absorption and damage resistance behaviour under dynamic loading.

The experimental studies were carried out on a high precision Instron 8801 universal testing machine (Figure 3.22.A) and DW750 Drop Weight Impact Test Machine (STEP Lab, Italy) impact testing machine (Figure 3.22.B) with digital data acquisition system. Flexural strength and modulus values were calculated from the load-deflection curves obtained from flexural tests, while force-time and energy-displacement curves were obtained from impact tests to determine the amount of absorbed and rebound energy. Each test configuration was repeated at least five times as specified in the standards to ensure statistical reliability. The following subsections describe in detail the test types, experimental setup, test parameters and data collection processes.

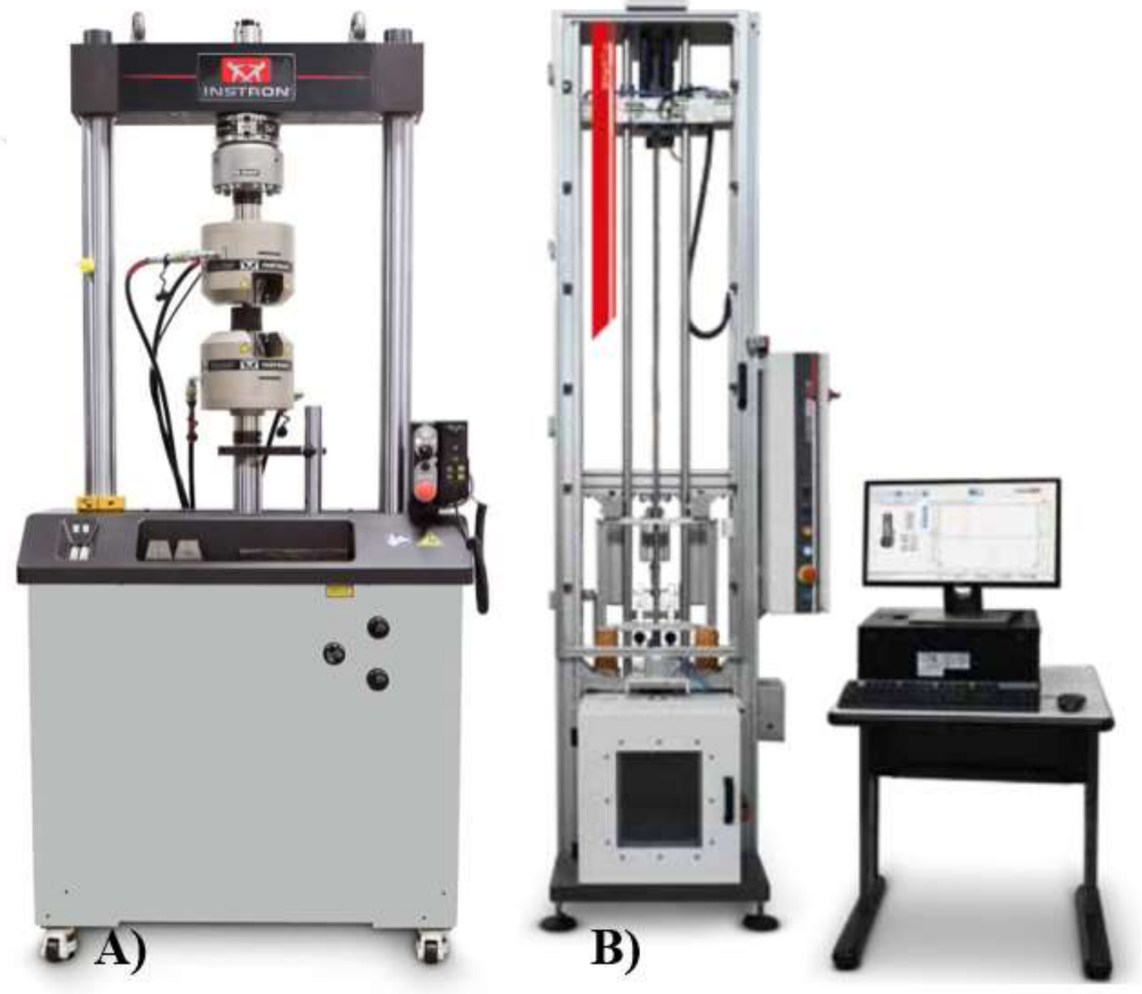

Figure 3.22. Test equipment used for mechanical characterisation of CFRP laminates. (A) Instron 8801 servo-hydraulic universal testing machine for three-point bending tests in accordance with ASTM D790. (B) DW750 drop-weighted impact tester for low velocity impact tests in accordance with ASTM D7136 (*STEP Lab, Italy*)

3.3.1. Three-Point Bending Test

The flexural performance of the manufactured CFRP laminates was evaluated by a three-point flexural test in accordance with ASTM D790 (International, 2015). The specimens were cut parallel to the direction of extension of the embedded microchannels, so that the applied bending load acts perpendicular to the channels.

Due to the anisotropic nature of the material, the 60:1 span/thickness (L/h) ratio recommended in the standard was used. This long span ratio reduces the effect of shear stresses and provides a more accurate determination of the actual flexural behaviour of the material. The thickness of each specimen was measured with a digital caliper at at least five different locations and averaged to calculate the average thickness for each specimen and each test group separately (Table 3.4). Due to the small differences between the average thicknesses, different span values were used for each test group. This approach improved the accuracy of the test results and comparability between specimens with different channel geometries.

The crosshead speed applied in flexural tests was calculated according to the Procedure B formula defined in ASTM D790. This procedure assumes an external fiber strain rate of Z=0.10 mm/mm/min and is recommended for use in thick composite materials. The velocity values calculated for each sample group using the equation which specified in 3.3 are given in Table 3.9. The loading rate is determined by the following relation:

$$R = \frac{ZL^2}{6d} \tag{3.3}$$

Where,

R= Rate of crosshead (mm/min)
L= Span Length (mm)
d= Depth of the specimen (thickness)

Table 3.9. Flexural test parameters for CFRP laminates with different microchannel geometries according to ASTM D790

Test Specimen Group	Average Thickness (mm)	Span-to-Thickness Ratio (L/h)	Span Length (mm)	Average Width (mm)	Crosshead Speed (mm/min)
Channelless Test Samples	3.86	60:1	232	51.11	23.2
Circular Channelled Test Specimens	4.042	60:1	242.52	51.31	24.252
Hexagonal Channelled Test Specimens	3.83	60:1	229.8	51.39	22.98
Square Channelled Test Specimens	4.211	60:1	252.66	51.25	25.266
Star Channelled Test Specimens	3.7828	60:1	226.968	51.34	22.696

Test Setup and Test Parameters

Flexural tests were carried out using the servo-hydraulic controlled Instron 8801 Universal Testing Machine. The machine has a maximum load capacity of 100 kN and can control the force applied during the test and the movement of the loading head with high precision. In this way, static load could be applied to the specimens at the desired speed in a stable and repeatable manner.

The tests were carried out in a three-point bending arrangement in accordance with ASTM D790. The specimens were placed between two lower supports and an upper loading head and the load was applied vertically through the upper head to the midpoint of the span (Figure 3.23). The applied load and deflection values at the midpoint were continuously recorded by the Instron 8800 digital control unit during the test.

In the CFRP specimens used in this study, the channels were positioned parallel to the longest side of the specimen. Because the applied load during the three-point bending test is vertical, this placement ensures that the channels are perpendicular to the load direction. The channels are positioned on the bottom surface of the test specimen in the testing machine, located in the region where maximum tensile stresses occur under bending loading. Therefore, the channel region is directly under tension. Furthermore, before reaching the channels, there are eight carbon fiber layers on the top surface, where the load first passes during bending, and two carbon fiber layers after the channels. This configuration was maintained for all bending test specimens, allowing for a reproducible study of the effect of channel geometry on mechanical behavior.

Figure 3.23. Three-point bending test setup used for bending testing of CFRP laminates (ASTM D790)

Procedure B and Type II configurations were preferred for the tests performed in this thesis. Procedure B is used when the specimen does not fracture before the elastic bending stress reaches 5%. This procedure allows the load-deflection relationship to be measured in the fully elastic region in order to determine the flexural modulus more accurately. In other words, the flexural stiffness and elastic behaviour can be evaluated without fracture of the material.

Type II is the test type in which the deflectometer (deflection indicator) system is used. This system directly measures the actual deflection between two specific points on the specimen and eliminates errors that may arise from crosshead movement. In this way, more precise and reliable bending data can be obtained, especially for composite and thick specimens.

Therefore, the choice of Procedure B and Type II is scientifically the most appropriate choice in order to test the specimens in the elastic region without fracture and to make deflection measurements with high accuracy and to reveal the effect of channel geometry on flexural behaviour more clearly.

As specified in ASTM D790, the test was automatically terminated when the applied load fell below 70% of the maximum force. This criterion ensured that the main fracture moment and the post-peak behaviour of the specimen were accurately recorded, while at the same time preventing excessive deformation or secondary damage. According to the test results obtained, it will be analysed to what extent different channel geometries change the load carrying capacity of the material with reference to the specimens without channel.

Determining The Effect of Channels on The Strength of Composite Structure

In order to quantitatively determine the effect of different microchannel geometries on cross-sectional properties and bending strength, the results obtained from three-point bending tests were first statistically evaluated for each channel geometry group, and the sample with the bending response closest to the group average was selected as the reference sample. The cross-sections of these reference specimens were scanned in detail using a coordinate measuring machine (CMM). The point coordinates obtained with the CMM were transferred to CAD software, and the actual cross-sectional contours of the specimens were reconstructed using this data. Thus, the wavy upper surfaces, local thickness variations, and geometric irregularities around the channel formed during the hot pressing process were included in the cross-section model (Figure 4.11). From these cross-sections obtained in the CAD environment, the moment of inertia (I) of the cross-section was calculated for each configuration, and the relevant findings are presented in the results section (section 4) of the study.

Determining The Shape Factor of Test Specimens

In this study, a bending shape factor (Ψ_B^e) has been defined for each selected reference test specimen in order to express the effect of the section properties on bending behaviour using a dimensionless parameter. The non-channelled laminate (BT-NC-03) was accepted as the reference section due to its flat and non-channelled structure, and the bending shape factor of all other channelled specimens was evaluated relative to this reference.

The bending shape factor is expressed as the ratio of the bending stiffness of each configuration to the bending stiffness of the reference laminate. In this context, the bending shape factor is defined as follows, using the bending modulus Ef obtained from three-point bending tests according to the ASTM D790 standard and the moment of inertia (I) calculated in the CAD environment.:

$$\Psi_B^e = \frac{S}{S_S} = \frac{EI}{E_S I_S} \tag{3.4}$$

On the other hand, since the bending stiffness and bending modulus (E) are quantities dependent on the slope of the force–deflection curve in the elastic region and the cross-section geometry, they are directly related to the shape factor. Therefore, in order to calculate the shape factor, it is first necessary to determine the bending moduli of the reference (non-channelled) specimens. According to the ASTM D790 standard, the flexural modulus for rectangular cross-section non-channelled specimens is calculated using the slope (m) of the force-deflection curve in the elastic region, as given in Equation 3.5.

$$E = \frac{mL^3}{4bd^3} \tag{3.5}$$

Where,

E : Modulus of elasticity in bending, MPa
L : Support span, mm
b : Width of beam tested, mm
d : Depth of beam tested, mm
m : Slope of the tangent to the initial straight-line portion of the load-deflection curve, N/mm

In calculating the flexural modulus of corrugated test specimens, the classical deflection equation involving the second moment of area (I) of the cross-section was used as a basis, and E was expressed for a simply supported beam loaded at its midpoint via the force-deflection (F–δ) relationship, as shown in Equation 3.6. Since the slope of the force-deflection curve in the elastic region is defined as in Equation 3.7, this expression can be rearranged, and the flexural modulus for corrugated specimens can be written as given in Equation 3.8. Thus, the flexural moduli for both non-channelled reference specimens and specimens with different channel geometries have been obtained consistently for use in calculating the shape factor in the following sections. The main reason to use the second moment of area (I) values directly is, that the top surfaces of the laminates do not have a flat geometry.

$$E = \frac{FL^3}{48\delta I} \tag{3.6}$$

Where,

E : Modulus of elasticity in bending, MPa
F: Applied load at the mid-span corresponding to the deflection δ, N
L : Support span, mm
δ : Mid-span deflection corresponding to the load F, mm
I: Second moment of area of the specimen cross-section about the neutral axis, mm^4

$$m = \frac{F}{\delta} \tag{3.7}$$

$$E = \frac{mL^3}{48I} \tag{3.8}$$

In this study, the slope m used in the flexural modulus calculations was obtained by applying a linear regression to the load–deflection data in the range between 20% and 30% of the maximum force F_{max}. This interval represents the initial straight-line (elastic) portion of the load–deflection curve, as shown in Figure 3.24.

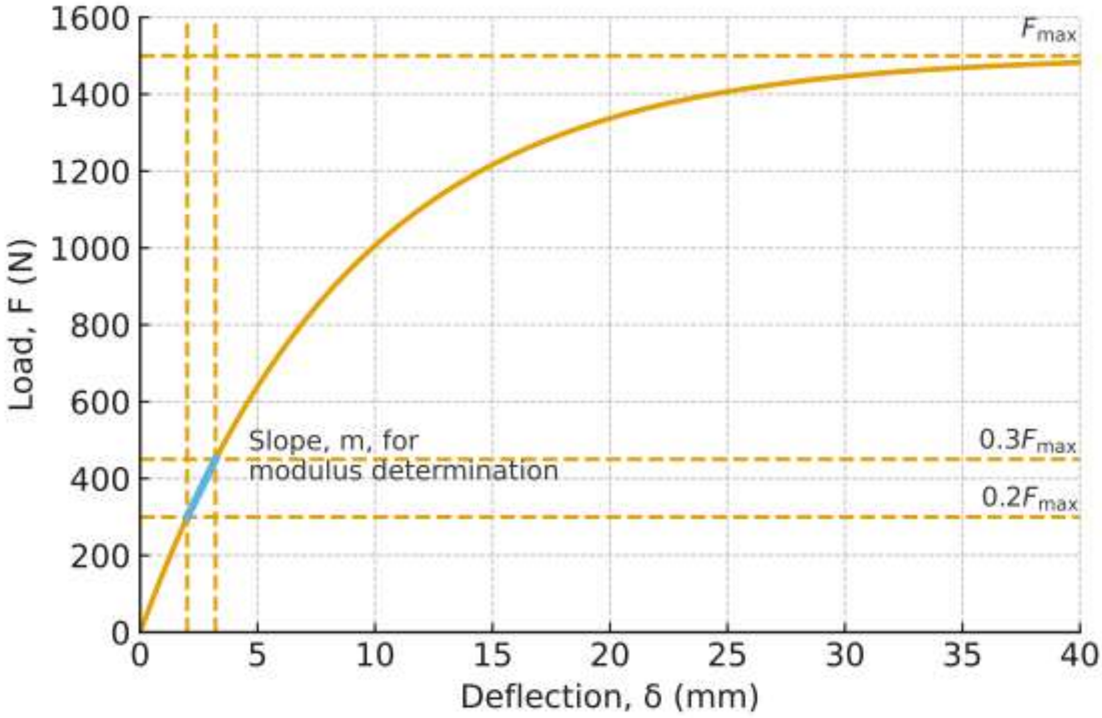

Figure 3.24. The representation of the 20% - 30% portion of the load-deflection curve for the slope calculations

With this approach, the bending modulus E_f and the section's moment of inertia (I) values have been consistently obtained for each channel geometry. In the following sections (Section 4), the bending behaviour of different channel groups will be compared, primarily using the non-channelled laminate (BT-NC-02) as a reference, based on the relative changes in breaking load, bending stiffness (deflection, m), bending modulus E_f, and section properties (I). Subsequently, using the bending shape factor (Ψ_B^e) defined for each channel configuration, the effect of the channel cross-section geometry on bending performance will be evaluated on a dimensionless and directly comparable scale.

Deflection Rigidity and Determination of Specific Deflection Parameters

After determining the bending shape factor (Ψ_B^e) for each reference sample, additional parameters have been defined to enable a fairer comparison of the bending response of the test groups. The F_{max}/δ_{max} ratio, frequently used as a practical indicator of stiffness in three-point bending tests, can be evaluated. However, since this quantity includes the total deformation up to the peak load, it may not always represent elastic stiffness. Furthermore, it is not suitable for direct comparison because the span (L) values differ between the groups compared in this study. Since deflection $\delta \propto L^3$ in three-point bending, the F_{max}/δ_{max} ratio reflects both the stiffness of the specimen and the span effect arising from the test conditions.

Additionally, the F_{max} and δ_{max} values may be affected by damage that begins to occur as the peak load is approached (loss of stiffness, matrix cracks, delamination, etc.). In this case, the F_{max}/δ_{max} ratio reflects both the elastic stiffness and the damage effect on the elastic region behaviour. Therefore, stiffness was calculated in this study from the slope of the elastic (linear) portion of the load–deflection curve. The elastic region slope ($m=\Delta F/\Delta\delta$) was determined by applying linear regression in the linear load range (approximately 0.2–0.3 F_{max}) selected in accordance with the ASTM D790 standard. The bending stiffness was calculated using the following equation with the obtained m and L values:

$$S_B \propto EI = \frac{mL^3}{48} \quad (3.9)$$

Due to the variation in sample lengths (ℓ) between groups, mass per unit length $\mu = M/\ell$ was used instead of total mass (M) in mass normalisation.

$$\mu = \frac{M}{\ell} \quad (3.10)$$

Accordingly, specific bending stiffness is defined as the ratio of bending stiffness to mass per unit length.

$$S_B^* = \frac{S_B}{\mu} \quad (3.11)$$

Similarly, to enable comparison by normalising the peak load capacity with mass, the specific maximum load (F_{max}^*) has been calculated as follows:

$$F_{max}^* = \frac{F_{max}}{\mu} = \frac{F_{max}}{M/\ell} = F_{max}\frac{\ell}{M} \quad (3.12)$$

With this approach, the effect of different span values on the stiffness parameters has been taken into account through the SB definition, and the mass differences arising from the sample length have been prevented from creating an artificial effect on the specific parameters.
Where,

- F_{max}: Maximum load, N
- δ_{max}: Deflection at F_{max}, mm
- m: Elastic region slope ($\Delta F/\Delta\delta$), N/mm
- L: Support gap (span), mm
- S_B: Bending stiffness (eşdeğer eğilme rijitliği), $N.mm^2$
- M: Mass of the specimen, g
- ℓ: Total sample length, mm
- μ: Mass per unit length (M/ℓ), g/mm
- S_B^* : Specific bending stiffness, $N.mm^3/$
- F_{max}^*: Specific maximum load, N.mm/g

3.3.2. Drop Weight Impact Test

Determination of the behaviour of composite materials under impact loads is of great importance for evaluating the reliability and durability of these materials under real service conditions. The falling weight impact test is based on the principle that a weight released with a controlled energy strikes the surface of the specimen and allows the types of damage caused by impact, energy absorption capacity and structural integrity to be examined. This method is widely used in the analysis of damage mechanisms such as delamination, fiber breakage and matrix cracking, especially in fiber-reinforced polymer composites.

In this study, the impact strengths of CFRP laminates with different microchannel cross-section geometries were compared with reference laminates without channels based on ASTM D7136/D7136M-20 standard. The aim of the low velocity impact tests was to determine the effects of differences in microchannel cross-sectional geometry on the ability of the material to absorb and dissipate impact energy, and to determine how and in which direction embedded channels change the damage behaviour compared to specimens without channels. In all tests, the impact load was applied at the geometrical centre of the specimen, i.e. the microchannel axis.

Force-time, energy-time and energy-displacement curves were recorded for each specimen and parameters such as maximum impact force, absorbed energy and rebound energy were calculated from these data. Statistical reliability was ensured by testing at least five specimens for each channel geometry.

Test Setup and Test Parameters

Impact tests were carried out using the STEP Lab DW750 Drop Weight Impact (DWI) Test Machine (*STEP Lab, Italy*) that has 750 joules impact capacity. This system works on the principle of free fall of impact mass with a certain potential energy and fulfils the low velocity impact test conditions defined in ASTM D7136/D7136M-20 standard. The device records the force, displacement and velocity data generated during the impact through high-precision sensors and energy-time curves are automatically obtained from these data.

During the test, the specimens were placed on the fixed lower support frame of the device and fixed at four corners with a support span of 125 mm. The impact tip has a 12.7 mm radius hemispherical steel head and in each test the impact load was applied to the microchannel axis at the geometric centre of the specimen. The test setup and impact head are shown in detail in Figure 3.24.

Impact test specimens were placed on the fixture with the channels oriented perpendicular to the support opening. Positioning was performed to ensure that no channels were located under the support points on the left or right sides. During test setup, the hemispherical impact tip was aligned with the geometric center of the laminate and adjusted to strike the channel precisely. In this study, because the channels were located at the bottom of the impact surface, a total of eight carbon fiber layers were located below the point where the impact was applied before reaching the channel and there are two carbon fiber layers under the channels. This placement arrangement was maintained for all specimens, allowing for a repeatable study of the effect of channel geometry on impact behavior.

Figure 3.24. Detailed view of the low velocity impact test rig showing the CFRP test specimen and hemispherical impact tip fixed on the DW750 drop weighted impact tester (*STEP Lab, Italy*)

A review of the literature reveals that a damage regime meeting the "Barely Visible Impact Damage (BVID)" criterion defined in the ASTM D7136/D7136M standard for CFRP laminates approximately 4 mm thick, but which does not cause complete penetration, is achieved with an impact energy of 30 J (This energy level falls within the range of 25–35 J, which is the typical energy range representing the BVID limit in CFRP materials in the literature.). Therefore, an impact energy of 30 J was also selected for this study.

The applied energy was determined by combining the impact mass (m = 4.323 kg), the drop height (h = 0.7145 m), and the contact velocity (v) was calculated as 3.744 m/s using the relationship given in Equation (3.4). Also, all parameters used in the test are summarised in Table 3.10.

$$v = \sqrt{\{2\, g\, h\}} \tag{3.4}$$

Where,

v= velocity

g= gravity

h= drop height

Table 3.10. Test parameters used in low velocity impact tests performed with DW750 drop weighted impact test machine

Name of Test Parameter	**Magnitude**
Drop Height (mm)	714.51
Drop Speed (m/s)	3.744
Drop Energy (J)	30
Total Drop Weight (g)	4323.7

4. RESULTS AND DISCUSSIONS

In this section, findings obtained from bending and impact tests applied to CFRP laminates with different microchannel cross-sectional geometries have been comprehensively analysed. Experimental data were evaluated in terms of load-carrying capacity, flexural stiffness, characteristics of force–deflection curves, energy absorption capacity, and observed damage mechanisms, and the relationship of these parameters with the channel geometry was systematically investigated. Since all specimens were prepared under the same production conditions (fiber architecture, matrix composition, curing temperature, pressure, and layer sequence), it is assumed that the performance differences between the groups are primarily due to the microchannel cross-section geometry. In this context, the numerical results, force–deflection curves, flexural moduli, absorbed energy values, statistical comparisons, and damage analyses for each geometry group were considered together to reveal in detail the effect of microchannel geometry on the mechanical performance of CFRP laminates.

In this regard, the data for each test group was first evaluated internally, and then the effects of different microchannel geometries on bending performance were examined in detail by comparing the reference test samples representing each group.

4.1. Flexural Behaviour of NC (Non-Channelled) CFRP Test Specimens

Non-channelled (NC) CFRP test specimens (for three-point bending tests) constitute the primary reference structure for this study because they do not contain any microchannels or geometric discontinuities. These specimens present pure bending behaviour to understand how the channels incorporated into the structure affect the mechanical behaviour of the material and to scientifically validate the findings.

This section examines the mechanical response of non-channelled specimens under three-point bending loading in detail. Using graphs generated using force-deflection data obtained from three-point bending tests, key performance indicators such as the stiffness response in the elastic region, the characteristic slope of the load-deflection curve, the peak load capacity, and the observed failure mechanisms were systematically analysed. The pure bending response of the non-channelled structure provides the essential starting point for accurately interpreting the effects of microchannel cross-section geometry on composite mechanical performance and establishing a reliable basis for comparisons to be made in subsequent sections.

4.1.1. Force–Deflection Response of NC (Non-Channelled) Test Specimens

To reveal the general trend of the data obtained from the three-point bending tests, the force–deflection curves of all tested specimens belonging to the non-channelled (NC) test group are presented together in Figure 4.1. This graph provides the opportunity to visually evaluate the characteristic features of pure bending behaviour and the repeatability between specimens.

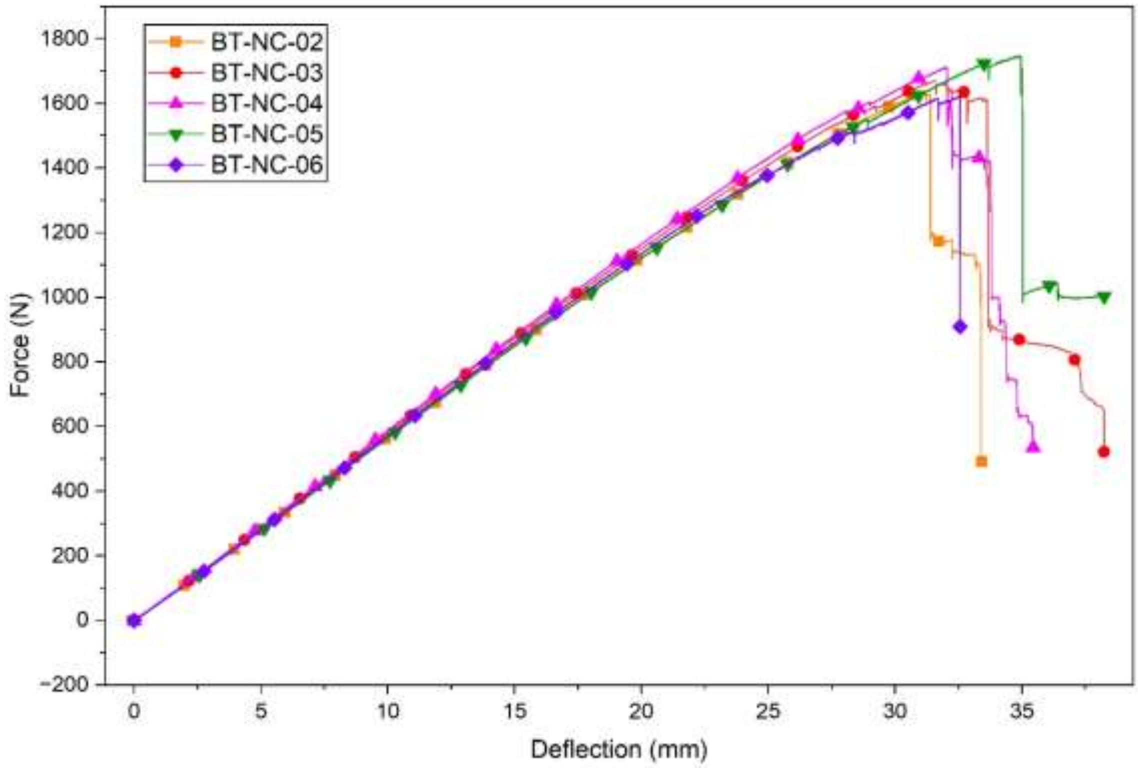

Figure 4.1. Force–deflection curves recorded during the three-point bending test of non-channelled (NC) CFRP test specimens

When examining the force–deflection curves of the non-channelled test group, it is observed that all specimens progress almost identically in the elastic region. This situation demonstrates that load transfer is both effective and highly consistent between specimens, thanks to the complete cross-sectional area in non-channelled specimens and the absence of interruption in fiber continuity by geometric discontinuities. This high overlap observed in the linear region confirms that the stiffness response of non-channelled specimens is stable and repeatable, and that the production process results in low mechanical variation between specimens.

The peak load (F_{max}) was concentrated in the range of 1600–1750 N for all NC specimens, and this narrow distribution indicates that the material has a microstructurally stable load-carrying capacity. The sudden load drop in the curve following the peak load indicates brittle failure behaviour in CFRP laminates, characterized by fiber fracture on the tensile side.

4.1.2. NC Failure Mechanism and Damage Observation

The damage mechanism observed in the NC specimens reflects the typical fracture mode of carbon fiber-reinforced composites under three-point bending loading. With increasing load, matrix cracks first formed, and as these cracks propagated, limited delamination occurred between the layers. Final fracture occurred on the lower surface corresponding to the tensile zone in all specimens and resulted in sudden fiber breakage. The absence of any micro-channels or geometric discontinuities within the cross-section caused the damage to exhibit a distinct, unidirectional, and rapidly progressing fracture form. The sudden loss of load-carrying capacity in the force–deflection curve also confirms this brittle tensile fracture. This pure bending fracture observed in the NC group provides a fundamental reference for evaluating the effect of microchannel cross-section geometries on the initiation and progression mechanisms of damage.

4.1.3. Flexural Test Results of the NC (Non-Channelled) Test Specimens

After interpreting the bending behaviour of the NC group from the graph, the test parameters of the samples were evaluated to demonstrate how this behaviour corresponds numerically. In this context, the characteristic values obtained from the three-point bending tests of the NC samples are presented in Table 4.1.

Table 4.1. Fundamental test parameters obtained from three-point bending tests of non-channelled (NC) CFRP test specimens

Specimen Code	Thickness (mm)	Fracture Force (N)	Deflection at Fracture Force ($\delta_{@fracture}$ mm)	Max Deflection (δ_{max}, mm)	Elastic Region Slope (m, N/mm)
BT-NC-02	3.84	1638.052	31.131	33.407	57.251
BT-NC-03	3.86	1671.61	31.563	38.236	59.391
BT-NC-04	3.88	1712.31	32.036	35.439	59.856
BT-NC-05	3.90	1746.99	34.953	38.229	58.041
BT-NC-06	3.84	1621.463	32.532	32.56	58.276

All calculations were made in accordance with ASTM D790. The maximum load value (F_{max}) was taken from the peak point on the load-deflection curve. δ@fracture represents the deflection value at the peak load (F_{max}) at which fracture occurs and represents the displacement reached by the specimen at the beginning of fracture. The maximum deflection represents the maximum deflection exhibited by the test specimen during the test.

The slope of the elastic region (m) was determined using the linear regression method applied in the linear elastic region to the values covering approximately 20-30% of the F_{max} values of the load-deflection curves. This approach, applied to each test group, allowed for the combined evaluation of data points representing the elastic zone and allowed for more reliable calculation of the slope values, independent of point measurement errors.

4.1.4. Statistical Evaluation of NC (Non-Channelled) Test Specimens (SD & COV Analysis)

The force–deflection curves belonging to the NC group and the results for each test specimen are presented in detail in Table 4.1. Later, the statistical distribution of these data was also evaluated. For this purpose, basic statistical indicators such as the mean, standard deviation, and coefficient of variation (COV %) of the fracture load (F_{max}) and elastic region slope (m) values obtained from all NC specimens were calculated and summarised in Table 4.2. This table quantitatively demonstrates the repeatability and consistency of the mechanical behaviour of the NC group and provides a solid reference for comparisons with other microchannel geometries.

Table 4.2. Statistical parameters for the fracture load (F_{max}) and elastic region slope (m) values obtained from the three-point bending tests of non-channelled (NC) CFRP test specimens

Parameter	Unit	Mean	Standard Deviation (SD)	COV (%)
Fracture Force (F_{max})	N	1678.085	51.888	3.092
Elastic Region Slope	N/mm	58.563	1.052	1.797

4.2. Flexural Behaviour of Circular-Channelled (CC) CFRP Test Specimens

Samples with circular cross-section (CC) channels form one of the fundamental comparison groups in evaluating the effect of embedded channel geometry on bending behaviour. The circular channel geometry is expected to have the lowest stress concentration among the geometries of microchannels due to its lack of corners in the cross-section and minimal disruption of fiber continuity. In this section, the bending behaviour of specimens with circular cross-section channels has been comprehensively evaluated, taking into account the load–deflection graph, the mechanical parameters obtained, the statistical distribution, and damage development.

4.2.1. Force–Deflection Response of Circular Channelled (CC) Test Specimens

In this section, data obtained from three-point bending tests were used to evaluate the mechanical responses of circular channelled (CC) test specimens which one of the microchannel specimen groups examined within the scope of this study, under bending load. In this context, the force–deflection curves for each CC specimen are presented together on a single graph in Figure 4.2, and the effects of the circular channel form on structural behaviour are discussed.

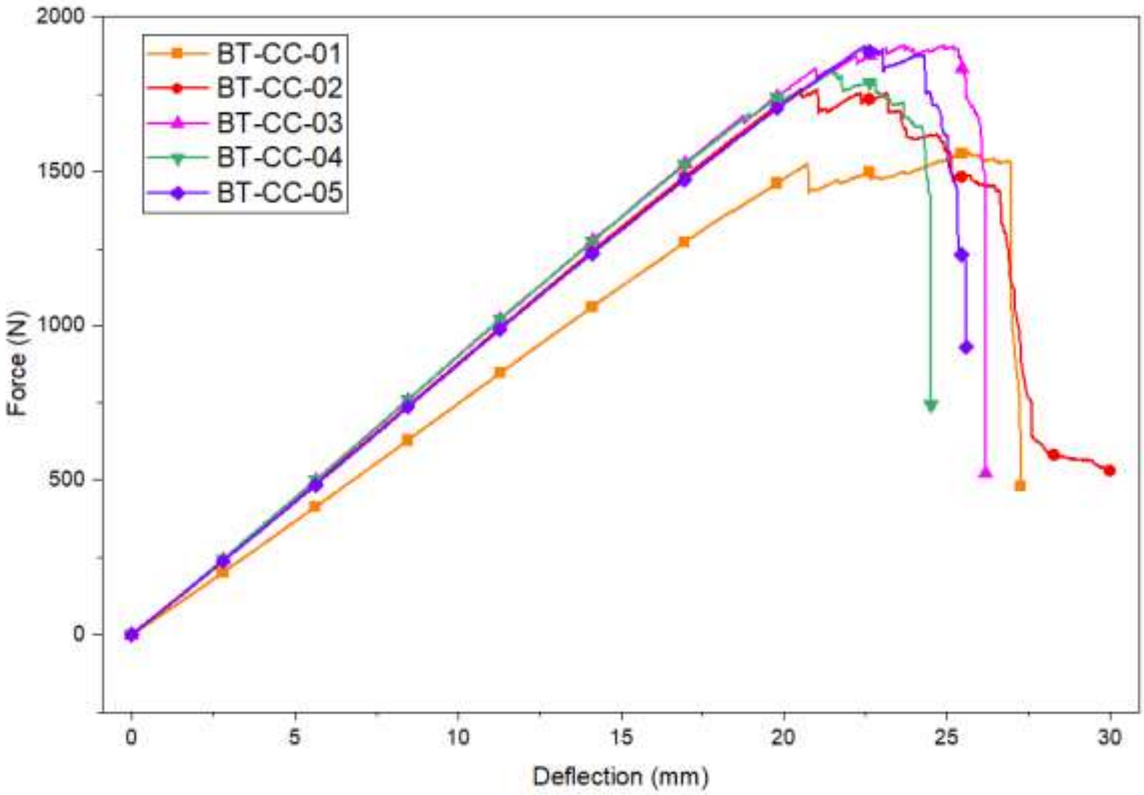

Figure 4.2. Force–deflection curves recorded during the three-point bending test of circular channelled (CC) CFRP test specimens (Nominal channel diameter Ø=4 mm)

The force–deflection curves of CC samples with circular microchannels exhibited a highly consistent and repeatable mechanical response throughout the elastic region. The curves of the BT-CC-02, BT-CC-03, BT-CC-04, and BT-CC-05 specimens are nearly superimposed, indicating that the circular channel geometry minimally disrupts fiber continuity and only slightly affects elastic deformation behaviour. The similar values of the slope (stiffness) in the elastic region for these four samples confirm both the repeatability of the production process and the high stability of load transfer for this geometry.

Specimen BT-CC-01, on the other hand, progresses at a lower slope in the elastic region compared to the other samples and exhibits a significant separation within the group. This difference may be related to the relatively lower thickness of the sample (Table 4.3) or to reduced stiffness that may have resulted from fiber placement variations (fiber density, resin ratio) resulting from local production. However, the deviation is limited and does not disrupt the overall behavior of the group.

When examining the peak load (F_{max}) levels, it is observed that the load-bearing capacity of the CC group generally reaches higher values compared to the NC group. In particular, the F_{max} values of the BT-CC-03, BT-CC-04, and BT-CC-05 samples are clustered in the range of approximately 1750–1900 N. This clustering indicates that the circular channel geometry minimizes stress concentration, thus not causing a significant reduction in cross-sectional strength and even allowing a higher load carrying capacity than some NC specimens. The more horizontal progression observed in the post-failure curve of the BT-CC-02 sample indicates a gradual post-peak load loss.

The curved shapes obtained in the fracture zone clearly reveal the damage development characteristic of circular channel geometry. While a sudden and sharp load drop resulted in typical brittle fracture in the BT-CC-04 and BT-CC-05 specimens, a more "semi-ductile" post-peak behaviour was observed in the BT-CC-02 and BT-CC-03 specimens, which continued to carry load to a limited extent after fracture. These differences are considered to be related to the amount of delamination formed during fracture and the local damage distribution around the channel.

Furthermore, examination of the fracture process reveals that the damage progressed in two stages. As the first two carbon fiber layers above the channel were the areas most exposed to tension on the tensile side, fracture initiation occurred in these layers, causing the first sudden drop in the force–deflection curve. Following the fracture of the upper layers, the remaining eight layers of the test specimen continued to carry the load, as shown in the figure 4.2. This resulted in a short-term preservation of load-carrying capacity in the post-peak region of the curve, followed by a second drop characterised by final fracture. This two-stage damage behaviour demonstrates that the circular channel altered the local stress distribution on the layer arrangement and guided the fracture process to a certain extent.

4.2.2. CC (Circular Channelled) Failure Mechanism and Damage Observation

When examining the force–deflection curves of the CC specimens, it is understood that the fracture behaviour follows a similar mechanism in all specimens. During the initial stages of load increase, the curves rise linearly and progressed almost superimposed in the elastic region. This indicates that the circular channels did not significantly disrupt the fiber arrangement in the elastic region and that load transfer was stable at this stage.

The initiation of fracture occurred in each specimen due to the breaking of fibers in the tensile region located above the channel. Due to the local stress concentration formed around the channel, damage occurred first as matrix cracking, then delamination developed, and finally fiber breakage occurred in the last stage. This sequential process manifested itself as a sudden drop in load on the force–deflection curve. In this initial stage, fiber breakage and matrix cracking were particularly concentrated in the first and second layers immediately above the channel.

Following the separation of the layers upper side of the channel, the crack propagated towards the lower layers. With the weakening of the interlayer bond, delamination expanded and the specimen fractured completely as a result of successive layer separations. This fracture process continued with the load gradually decreasing after the peak load without being completely zero for a short period of time in the specimens.

In general, damage in CC samples is characterised by matrix cracking and fiber breakage starting on the channel, followed by layer separation and limited delamination, exhibiting a similar fracture sequence in all samples.

4.2.3. Flexural Test Results of the CC (Circular Channelled) Specimens

Following the graphical evaluation of the bending behaviour of circular channelled (CC) specimens, the test results obtained from three-point bending tests are presented in this section to demonstrate how this behaviour corresponds numerically. For each circular channelled (CC) test specimen, the fracture load (F_{max}), deflection at fracture ($\delta_{@fracture}$), maximum deflection (δ_{max}), and elastic region slope (m) values are detailed in Table 4.3. These results enable a quantitative evaluation of the effect of circular channel geometry on stiffness, carrying capacity, and deformation behaviour, and form the basis for statistical comparisons to be made in the following subsection.

Table 4.3. Fundamental test parameters obtained from three-point bending tests of circular-channelled (CC) CFRP test specimens

Specimen Code	**Thickness (mm)**	**Fracture Force (N)**	**Deflection at Fracture Force ($\delta_{@fracture}$, mm)**	**Max Deflection (δ_{max}, mm)**	**Elastic Region Slope (m, N/mm)**
BT-CC-01	3.8	1566.78	25.623	27.922	74.350
BT-CC-02	4.06	1765.88	20.494	27.13	87.387
BT-CC-03	4.14	1909.14	23.686	34.244	90.549
BT-CC-04	4.2	1823.99	21.472	28.852	90.545
BT-CC-05	4.02	1906.17	22.452	29.228	88.024

4.2.4. Statistical Evaluation of CC (Circular Channelled) Specimens (SD & COV Analysis)

The statistical distribution of the fracture load (F_{max}) and elastic region slope (m) values for the CC samples is given in Table 4.4. The calculated coefficient of variation (COV ≈ 7.8%) for both parameters indicates that the CC group exhibits higher variation in its mechanical response compared to the NC group. The fact that COV values are approximately 3% in the NC group indicates that the non-channelled structure has a more homogeneous load transfer. Also, the increase in the CC group may be related to local fiber distribution differences around the channel, thickness variations, and microstress distribution.

Table 4.4. Statistical parameters for the fracture load (F_{max}) and elastic region slope (m) values obtained from the three-point bending tests of circular-channelled (CC) CFRP test specimens

Parameter	Unit	Mean	Standard Deviation (SD)	COV (%)
Fracture Force (F_{max})	N	1794.392	140.674	7.839
Elastic Region Slope	N/mm	86.171	6.762	7.848

In circular channelled samples, both F_{max} and the elastic region slope (m) group, is not due to better fiber continuity compared to NC, but rather because small increases in specimen thickness significantly increase sectional rigidity and the circular channel geometry only slightly disrupts fiber alignment, thereby largely preserving elastic load transfer. The slight increase in thickness observed in the CC group is related to the insufficient layer compression of the fiber layers around the channel and the resulting resin accumulation (resin-rich zone) in this area. The circular shape of the monofilament has caused a minimal increase in thickness in the sample cross-section, particularly around the channel. Since increasing the thickness nonlinearly increases the section strength under bending, the elastic region slope (m) is higher compared to the NC samples. Therefore, the increase in the elastic region slope observed in the CC group can be interpreted as a result of geometric and production-induced section effects.

4.3. Flexural Behaviour of HC (Hexagonal Channelled) CFRP Test Specimens

This section examines in detail the bending behaviour of hexagonal microchannel (HC group) CFRP laminates. While the hexagonal channel geometry is expected to increase bending stiffness by enhancing sectional inertia, it is anticipated that stress concentrations at the channel corners may adversely affect fracture behaviour. Therefore, the three-point bending test results for HC specimens will be evaluated in terms of load–deflection response, damage/fracture mechanisms, fundamental bending parameters, and statistical distribution to reveal the net effect of this channel configuration.

4.3.1. Force–Deflection Response of HC (Hexagonal Channelled) Test Specimens

Figure 4.3 shows the force–deflection curves obtained under three-point bending loading for test specimens with hexagonal channels. This graph provides a comprehensive comparison of the elastic region behaviour, maximum load capacity, and general post-failure trends of the hexagonal channelled (HC) test group, thereby establishing a fundamental framework for evaluating the group's bending performance.

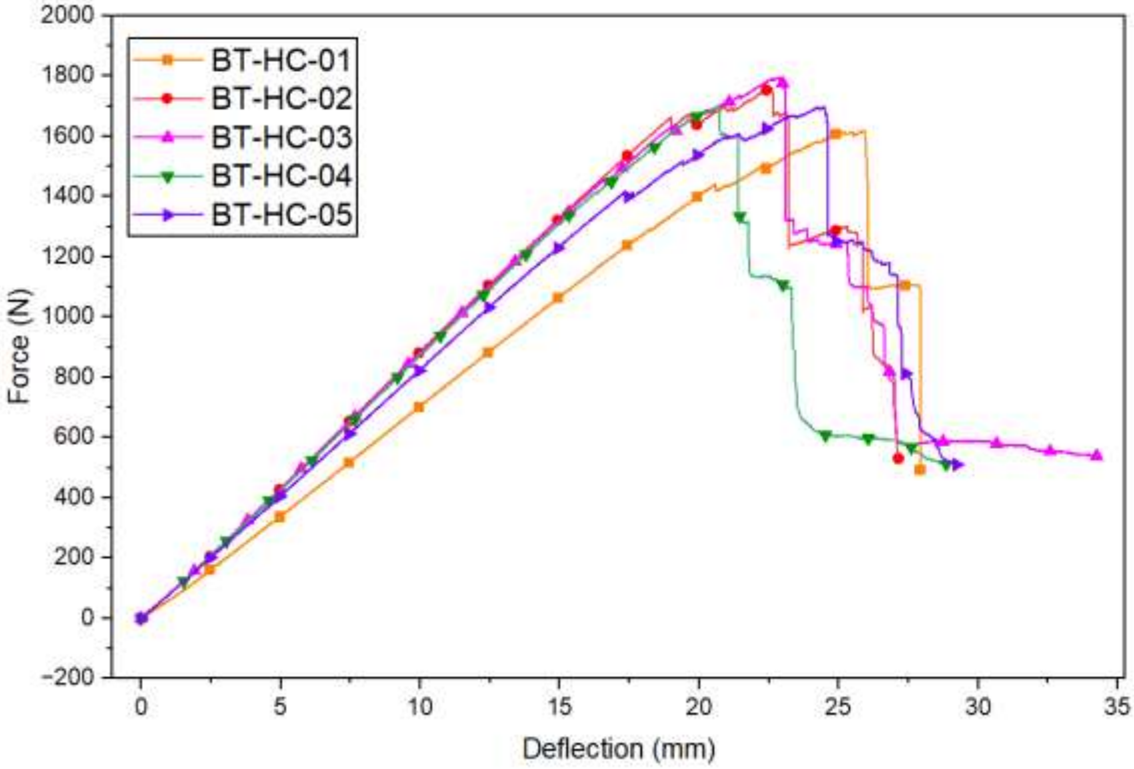

Figure 4.3. Force–deflection curves recorded during the three-point bending test of hexagonal-channelled (HC) CFRP test specimens (Nominal channel diameter Ø=4 mm)

The force-deflection curves of the HC group exhibit a higher slope and distinct rigid behaviour in the elastic region. Up to approximately 15–20 mm in the linear section, force values were higher than NC specimens at similar deflection levels. This indicates that the hexagonal channel geometry increased the sectional inertia, resulting in slightly higher initial bending stiffness than the NC group.

Also, HC curves reach the peak region earlier than NC, and the maximum load generally occurs at lower deflection values around 20–22 mm. After the peak, it is observed that the force decreases in a multi-stage and irregular manner in HC samples, with sudden load drops being particularly prominent in the HC-04 sample. This situation indicates that damage begins early due to stress concentrations formed at the corners of the hexagonal channel and that stability after fracture is limited. For comparison, although NC specimens have a lower initial slope, they reach peak load at greater deflections and, after fracture, the load decrease following F_{max} is spread over a wider deflection range in hexagonal-channel specimens compared to non-channel specimens, and a more distinct residual load carrying capacity is retained. In non-channelled specimens, however, after the maximum load, the load tends to decrease more sharply within a shorter deflection range. This situation demonstrates that hexagonal channelled specimens exhibit a more distinct progressive damage development under bending compared to non- channelled structures, while non-channelled specimens display behaviour closer to sudden fracture.

As a result, the HC group offers higher stiffness and a more distinct gradual damage development in the elastic region compared to the NC, but this gain comes with lower deformation capacity and more irregular fracture behaviour.

4.3.2. HC (Hexagonal Channelled) Failure Mechanism and Damage Observation

The damage mechanism observed in HC specimens indicates that microchannel carbon fiber reinforced composites exhibit a more complex fracture behaviour under three-point bending, due to the varying stress distribution around the channel. The emergence of multiple gradual load decreases following the elastic region in the force-deflection curves with the increase in load and the observation of distinct fracture areas on the tensile side of the samples corresponding to the upper region of the channel after the test, This indicates that the damage is predominantly concentrated around the top of the channel.

When fracture surfaces observed at the macro scale and typical bending damage modes reported in the literature are evaluated together, it is thought that the damage process may have been shaped by the sequential effect of matrix cracks starting in the tensile zone above the channel, layer separations (delamination) progressing towards the channel perimeter, and fiber fractures developing in the upper layers with advancing loading. It is evaluated that the angular geometry of the hexagonal channel section may increase local stress concentrations around the channel within the test specimens, and the small angular rotations of the hexagonal channels around their axis during the laying and hot press curing of the monofilaments which used to create the channel may slightly change this stress distribution from sample to sample. As a result of these effects, it can be said that the sequential and fluctuating bearing capacity losses observed in the force-deflection curves of the HC samples are compatible with a behaviour suggesting that the damage progresses in the form of a gradual and spread fracture around the channel.

4.3.3. Flexural Test Results of the HC (Hexagonal Channelled) Specimens

The fundamental bending test parameters corresponding to the force–deflection curves presented in Figure 4.3 are summarised in Table 4.5 for hexagonal channel (HC) CFRP test specimens. The table enables a quantitative assessment of the flexural performance of the HC group by providing the thickness of each specimen, the force and deflection values at failure, the maximum deflection amount, and the elastic region slope (m) together. The elastic region slope (m) was determined by applying a linear regression method to the linear portion of the load–deflection curve covering approximately 20–30% of the load range F_{max}, as previously stated in Section 4.1.3.

Table 4.5. Fundamental test parameters obtained from three-point bending tests of hexagonal channel (HC) CFRP test specimens

Specimen Code	**Thickness (mm)**	**Fracture Force (N)**	**Deflection at Fracture Force ($\delta_{@fracture}$ mm)**	**Max Deflection (δ_{max}, mm)**	**Elastic Region Slope (m, N/mm)**
BT-HC-01	3.798	1619.78	25.891	27.922	71.487
BT-HC-02	3.873	1762.99	22.556	27.13	90.812
BT-HC-03	3.881	1796.05	22.863	34.244	88.980
BT-HC-04	3.855	1698.84	20.665	28.852	86.693
BT-HC-05	3.743	1698.96	24.486	29.228	84.514

When evaluated together with the data presented in Table 4.1 for the non-channelled (NC) group, it is observed that the elastic region slopes of the HC samples are significantly higher compared to the NC group, while their fracture and maximum deflection values are lower. This indicates that hexagonal channelled specimens are more rigid under bending loads than the NC group but have a more limited deformation capacity.

4.3.4. Statistical Evaluation of HC (Hexagonal Channelled) Specimens (SD & COV Analysis)

Table 4.6 shows the fracture load (F_{max}) and elastic region slope (m) calculated for the three-point bending tests of hexagonal channel (HC) CFRP specimens. The coefficient of variation (COV) of approximately 3.96% obtained for the F_{max} values indicates that the failure load in the HC group has a very low dispersion and that the experiments offer a good level of repeatability. The COV value of approximately 9% for the elastic zone slope indicates that stiffness is more sensitive to the channel geometry and, in particular, to stress concentrations developing in the channel region, but remains within acceptable limits of variability.

Table 4.6. Statistical parameters for the fracture load (F_{max}) and elastic region slope (m) values obtained from the three-point bending tests of hexagonal channel (HC) CFRP test specimens

Parameter	**Unit**	**Mean**	**Standard Deviation (SD)**	**COV (%)**
Fracture Force (F_{max})	N	1715.324	67.928	3.960
Elastic Region Slope	N/mm	84.497	7.649	9.053

When evaluated together with the statistical results given in Table 4.2, the HC samples' F_{max} average is quite close to that of the NC group, whereas the average elastic region slope reaches significantly higher values. On the other hand, the COV of the m parameter in the HC group (~9%) is significantly higher than the value in the NC group (~1.8%), indicating that while the hexagonal channel geometry increases the bending rigidity, indicates that the mechanical response exhibits a more variable character compared to NC samples due to the small angular rotations of the hexagonal cross-section around its own axis during the laying and hot pressing curing of the monofilaments used to create the channel, and the associated local microstructural differences formed around the channel.

4.4. Flexural Behaviour of SC (Square Channelled) CFRP Test Specimens

In this subsection, the behaviour of square microchannel (SC group) CFRP specimens under three-point bending is investigated. To observe how the square channel geometry affects the sectional rigidity and how stress concentrations that may occur at the channel corners are reflected in the fracture behaviour, the load–deflection curves and fundamental bending parameters of the SC specimens were compared with those of the group without channels.

4.4.1. Force–Deflection Response of SC (Square Channelled) Test Specimens

When examining the force–deflection curves (Figure 4.4) of the square channel (SC) test group, it is observed that during the initial stages of loading (around 0–10 mm), all specimens exhibit a nearly overlapping, smooth, and linear increase. The slopes in this region are very close to each other, meaning that the presence of square channels does not create a significant difference between samples in this range. Elastic stiffness is quite consistent across the group in the 0–10 mm range. Compared to the non-channelled (NC) specimens, this initial linear region has similar character; in fact, the slope observed in the curves of the square-channelled (SC) test group is slightly higher than the non-channelled (NC) specimens. This indicates that the square channel does not significantly reduce the section rigidity in this area; on the contrary, it can increase it to a limited extent in some specimens.

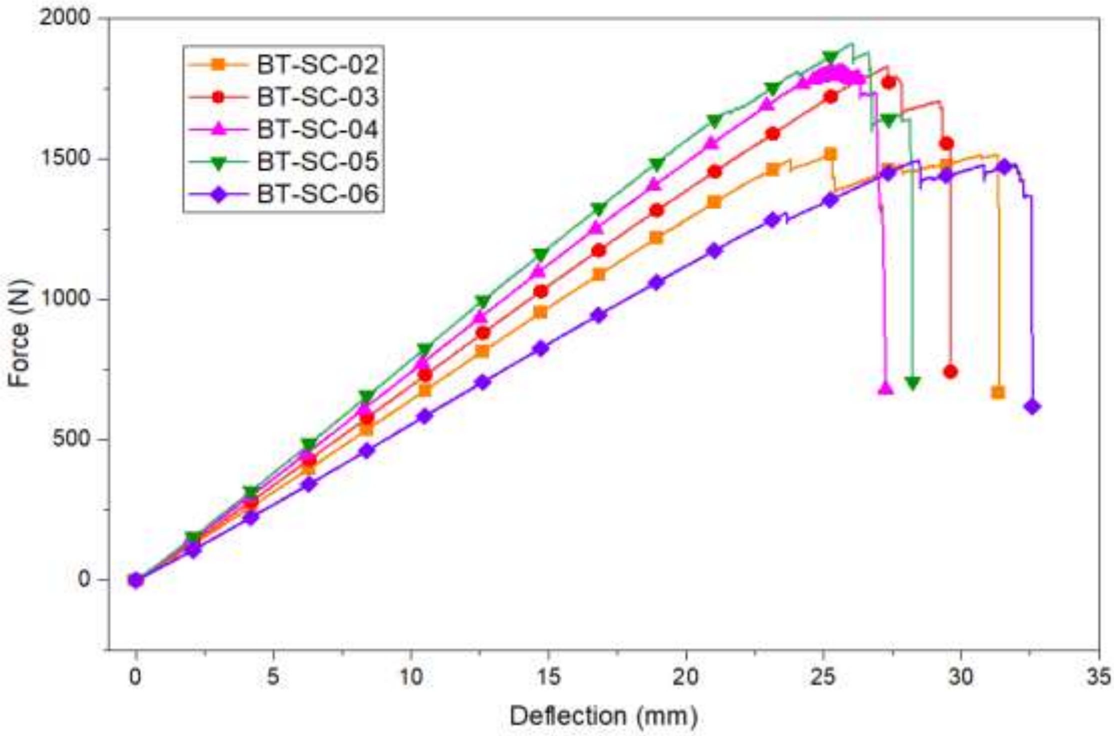

Figure 4.4. Force–deflection curves recorded during the three-point bending test of square-channelled (SC) CFRP test specimens (Nominal channel diameter Ø=4 mm)

At approximately 10–20 mm deflection, the curves remain largely linear, but the force levels between the specimens begin to diverge significantly. The BT-SC-05 curve carries the highest loads in this region, while BT-SC-06 moves at the lowest load level, with the other specimens progress in between. Therefore, even if the square channel geometry remains constant, local variations arising from production and local rotations around the channel axis cause significant dispersion in the transport capacity. Considering that the curves in the NC group progress much closer to each other within the same deflection range, it can be stated that the SC group exhibits a more dispersed behaviour compared to NC in terms of maximum load and deformation capacity.

At the maximum load region, SC specimens reach peak values in the range of approximately 1500–1900 N, and these peaks generally occur at deflections of around 25–30 mm. Compared to specimens without channels, specimens with square channels are seen to reach similar, and in some cases even higher, maximum load levels at slightly lower deflections. This situation suggests that square-channel specimens generally exhibit a more rigid bending behaviour with a limited deformation capacity.

When the force–deflection curves of square-channelled and non-channelled specimens are evaluated together, it is observed that in the square-channelled group, after F_{max}, the load decreases within a relatively short deflection range in most specimens, with only a few specimens retaining a limited residual load-carrying capacity. In non-channelled specimens, after the maximum load, load loss in some specimens is distributed over a wider deflection range, occurring as a gradual decrease, and in this region, the load-bearing capacity is now significantly preserved compared to square-channel test specimens. Therefore, it can be said that the square channel geometry makes the fracture process more sudden and reduces the amount of ductile deformation according to channelless laminates, while largely preserving the load carrying capacity under bending.

4.4.2. SC (Square Channelled) Failure Mechanism and Damage Observation

When examining the fracture surfaces formed after three-point bending in the SC group, it was observed that the damage was generally concentrated in areas associated with the square channel region. Crack formation and progression have become more distinct, particularly in the area subjected to tensile stress between the channel and the lower surface of the sample. The more prominent appearance of broken lines and separations around the corners of the channel suggests that stress accumulation may be effective in these areas. Fracture surfaces observed at the macro scale exhibit behaviour consistent with typical bending damage modes concentrated on the tension side under three-point bending.

When the load approached the F_{max} level, in some SC samples (e.g. BT-SC-03 and BT-SC-05), the crack rapidly penetrated the cross-section, causing a sudden loss of load-bearing capacity with delamination around the channel. On the other hand, in specimens such as BT-SC-02 and BT-SC-06, some of the fibers continued to carry load after the initial crack, and a short plateau and limited residual load-carrying capacity were observed in the force–deflection curves. This situation reveals that fracture in the SC group can exhibit both sudden and partially gradual characteristics depending on the specimen.

Compared to non-channelled (NC) specimens, it can be said that damage in SC specimens is more concentrated around the channel and that fracture is directed by the square channel corners. In NC specimens, bending damage develops with a more uniform tensile crack and delamination in the mid-span region, whereas in SC specimens, crack initiation shifts to the narrow cross-section region between the channel and the surface, and after F_{max}, the load decreases rapidly over a shorter deflection range in most specimens. These results demonstrate that while the square channel geometry maintains the overall bending load-carrying capacity, it concentrates damage around the channel and renders the fracture behaviour partially more localised and abrupt compared to non-channelled laminates.

4.4.3. Flexural Test Results of the SC (Square Channelled) Specimens

The fundamental bending test parameters corresponding to the force–deflection curves presented in Figure 4.4 are summarised in Table 4.7 for square-channel (SC) CFRP test specimens. The table enables a quantitative assessment of the flexural performance of the SC group by providing the thickness of each specimen, the force and deflection values at failure, the maximum deflection amount, and the elastic region slope (m) together. The elastic region slope (m) was determined by applying the linear regression method to the linear portion of the load–deflection curve covering the load range of approximately 20–30% of F_{max}, as indicated in the preceding sections. According to Table 4.7, the elastic region slope in the SC samples varies between 57–79 N/mm; the highest stiffness is obtained in the BT-SC-05 sample, while the lowest stiffness is obtained in the BT-SC-06 sample. The fracture forces are in the range of 1490–1910 N, with the BT-SC-05 and BT-SC-03 samples representing the highest load-bearing capacity within the group. The deflection values at the point of failure are clustered in the 25–28.5 mm range indicates that the SC group reached damage at similar deformation levels under bending.

Table 4.7. Fundamental test parameters obtained from three-point bending tests of square-channelled (SC) CFRP test specimens

Specimen code	**Thickness (mm)**	**Fracture Force (N)**	**Deflection at Fracture Force ($\delta_{@fracture}$, mm)**	**Max Deflection (δ_{max}, mm)**	**Elastic Region Slope (m, N/mm)**
BT-SC-02	4.05	1516.65	25.251	31.353	64.098
BT-SC-03	4.27	1828.64	27.314	29.602	70.712
BT-SC-04	4.375	1808.43	25.654	27.245	75.203
BT-SC-05	4.31	1910.43	26.046	28.231	79.459
BT-SC-06	4.05	1494.14	28.445	32.569	57.266

When evaluated together with the data presented in Table 4.1 for the non-channelled (NC) group, the average elastic region slopes of the SC samples are significantly higher than the NC group (approximately 69 N/mm versus 59 N/mm), while the fracture and maximum deflection values are significantly lower than the NC samples. In other words, although the failure loads in the SC group are at the same level as the NC group, and even slightly higher in some samples, these load levels are reached at lower deflection values. These results demonstrate that the square-section microchannel significantly maintains and increases the sectional rigidity under bending, but allows for a more limited deformation capacity compared to laminates without channels. Therefore, it can be said that SC samples exhibit a behaviour that is more rigid under bending loads than the NC group, but with a more limited capacity for deformation.

4.4.4. Statistical Evaluation of SC (Square Channelled) Specimens (SD & COV Analysis)

Table 4.8 presents the statistical parameters (mean F_{max}, mean m, standard deviation, and COV) calculated for the fracture load (F_{max}) and elastic region slope (m) obtained from the three-point bending tests of square-channelled (SC) CFRP specimens. The coefficient of variation (COV) value which obtained from F_{max} values is approximately 11.23% indicates that the fracture load in the SC group has a higher dispersion compared to hexagonal channelled and non-channelled specimens. However, it still offers an acceptable level of repeatability for composite production cured under hand lay-up and hot press conditions. The fact that the COV value for the elastic zone slope is approximately 12.7% suggests that the bending stiffness may be highly sensitive to the square channel geometry and, stress concentrations developing around the channel corners.

Table 4.8. Statistical parameters for the fracture load (F_{max}) and elastic region slope (m) values obtained from the three-point bending tests of square-channel (SC) CFRP test specimens

Parameter	**Unit**	**Mean**	**Standard Deviation (SD)**	**COV (%)**
Fracture Force (F_{max})	N	1711.658	192.290	11.234
Elastic Region Slope	N/mm	69.348	8.830	12.733

When evaluated together with the statistical results given in Table 4.2 for the non-channelled (NC) group, it is seen that the average F_{max} of the SC samples is approximately 2% higher than the NC group, while the average elastic region slope is approximately 18% higher. However, the fact that the COV for the m parameter in the SC group (~12.7%) is significantly higher than the value in the NC group (~1.8%) indicates that the mechanical response has become more sensitive to geometric and microstructural differences and stiffness values show greater variation from sample to sample. During the lay-up and hot press process, production-related effects such as slight rotation of the channels within the laminate, resin accumulation around the channel corners, and fiber waviness cause both F_{max} and m values to exhibit a more pronounced statistical dispersion in the SC group compared to the NC samples. In other words, the square channel cross-section increases the average rigidity and load-bearing capacity in the SC group, but it also increases the sensitivity of the cross-section to local defects, thereby significantly increasing the statistical dispersion compared to NC.

4.5. Flexural Behaviour of StC (Star Channelled) CFRP Test Specimens

In this subsection, the behaviour of star microchannel (StC group) CFRP specimens under three-point bending is investigated. It is thought that the star-shaped channel may affect both stiffness and damage development differently from other channel geometries by irregularly distributing the cross-sectional area. In this context, the load–deflection curves, fracture patterns, and fundamental bending parameters of the StC specimens were evaluated comparatively with the non-channelled and other channelled groups.

4.5.1. Force–Deflection Response of StC (Star Channelled) Test Specimens

In this subsection, the bending behaviour of CFRP laminates with star-shaped (StC) microchannels under a three-point bending test is investigated. Figure 4.5 presents the force–deflection curves for five StC specimens, from which the initial bending stiffness, maximum load-carrying capacity, and total deformation behaviour within the group were evaluated. The results obtained will be compared with the findings from non-channelled test specimens, as in the previous sections, in order to reveal the effect of the star-shaped microchannel on bending performance.

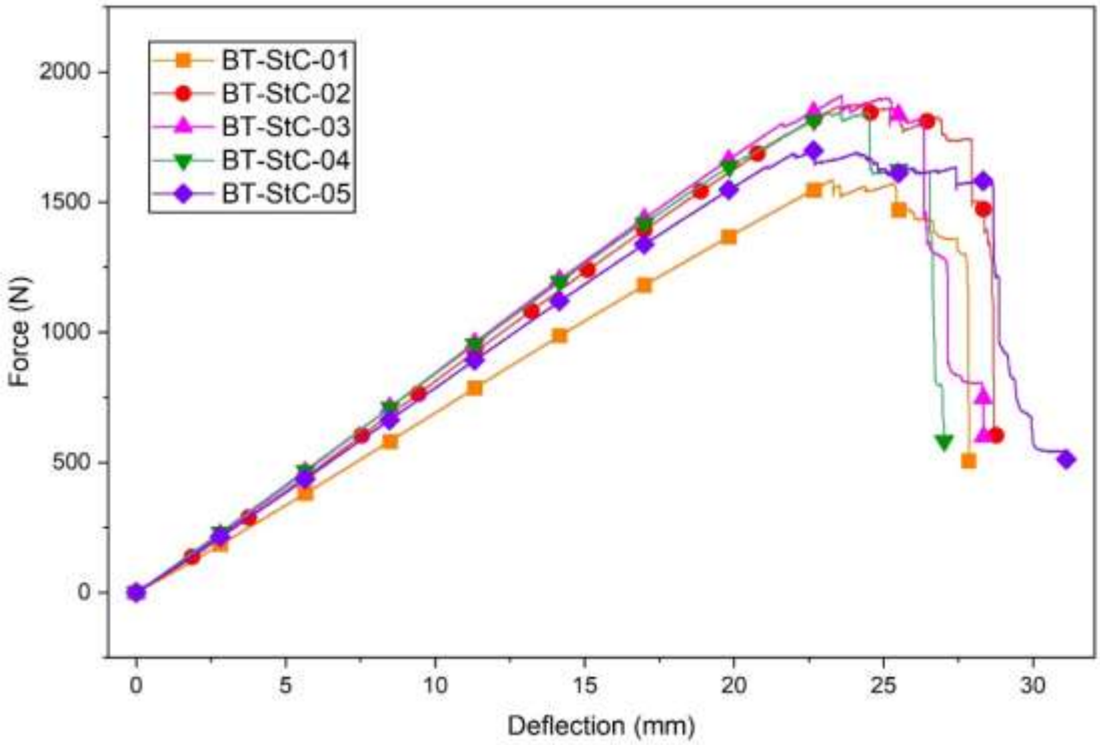

Figure 4.5. Force–deflection curves recorded during the three-point bending test of star-channelled (StC) CFRP test specimens (Nominal channel diameter Ø=3.3 mm)

When examining the curves given in Figure 4.5, it can be seen that all StC samples follow a similar linear trend at the start of the load increase and largely overlap in the elastic region. The fact that the force–deflection curves progress quite closely to each other up to approximately 15–18 mm indicates that the star-shaped channel does not significantly reduce the global bending stiffness of the test specimen during the initial loading phase. The slope of the curves (m) in this range indicates that the samples in the StC group are quite close to each other dimensionally and that the initial bending behaviour is repeatable.

As the end of the elastic region was approached, deviations from linear behaviour began to appear in the curves, and after approximately 20 mm, gradual stress drops were observed in some specimens, while more sudden drops were seen in others. In particular, the BT-StC-01 specimen reached a lower maximum load level compared to the other specimens and exhibited a curve with a more rounded peak structure. In contrast, samples BT-StC-02, BT-StC-03 and BT-StC-05 reached levels of approximately 1800–2000 N and then showed gradual load decreases. In sample BT-StC-04, a sudden load drop occurred after the peak load, indicating a more brittle fracture behaviour characterised by sudden crack propagation.

These different post-peak load drop behaviours observed after the peak point of the force–deflection curves indicate that the damage mechanisms occurring around the star-shaped channel can vary from sample to sample. In some samples, the rapid drop in load suggests that cracks starting in the upper tensile region of the channel quickly combine with delamination, leading to a sudden loss of load-carrying capacity. In other samples, however, the gradual decrease in load indicates that fiber breakage, matrix cracking and interlaminar separation developed in a more widespread and progressive manner. In general, the force–deflection curves belonging to the StC group show that the maximum load level under bending and the residual load level that the specimens can carry after fracture are somewhat reduced compared to specimens without channels. Nevertheless, the fact that the specimens in the elastic region have quite similar slope indicates that they exhibit repeatable bending behaviour within their own group in terms of initial bending rigidity.

4.5.2. StC (Star Channelled) Failure Mechanism and Damage Observation

The damage observed in StC specimens with star-shaped microchannels was observed to initiate predominantly in the tensile region above the channel under bending loading. As the load increased, matrix cracks, separation at the fiber-matrix interface, and local fiber fractures developed in the regions corresponding to the sharp ends of the star channel. It is thought that the sharp geometric discontinuities in these regions increased stress concentrations under tension, facilitating crack initiation. As the damage progresses, it can be said that delamination occurs as the cracks spread towards the interlayer regions, and the load-bearing capacity gradually decreases.

The fact that the cross-sectional area of the star channel is approximately one-third of the cross-sectional areas of the other channel geometries emerges as an additional parameter in interpreting the fracture behaviour. The relatively small cross-section of the channel increases the proportion of carbon fibers that are not interrupted around the channel and causes the level of discontinuity along the cross-section to remain more limited compared to channels with circular, hexagonal or square cross-sections. Since no material is removed in the production method, the channel is defined only by the polyamide monofilament and a certain volume of carrier fiber is maintained around it. This allows some of the surrounding fiber bundles to continue carrying the load for a while longer as the crack propagates, even though the sharp corners initiate the damage relatively early. The gradual load reductions observed in the force–deflection curves indicate that the damage may be characterised not by a sudden fracture occurring at a single moment, but rather by damage accumulating progressively in different regions, with a specific quantity of load-bearing fibers breaking and failing sequentially at each stage.

Generally speaking, the fracture behaviour observed in the StC specimens can be explained by a combined mechanism resulting, on the one hand, from the formation of significant stress concentrations in the channel-top tensile zone due to the sharp edges of the star geometry and, on the other hand, from the relative smaller of the channel cross-sectional area, which allows a certain degree of fiber continuity to be maintained around the channel.

4.5.3. Flexural Test Results of the StC (Star Channelled) Specimens

The fundamental flexural test parameters corresponding to the force–deflection curves presented in Figure 4.5 are summarised in Table 4.9 for star-channelled (StC) CFRP test specimens. The table enables a quantitative evaluation of the flexural performance of the StC group by providing the thickness of each specimen, the force and deflection values at failure, the maximum deflection amount, and the elastic region slope (m) together. The elastic region slope (m) was determined by applying the linear regression method to the linear portion covering approximately 20–30% of the load range of F_{max} on the relevant load–deflection curve, as indicated in the preceding sections. According to Table 4.9, the elastic region slope in the StC samples varies between 69.8 and 86.7 N/mm; the highest stiffness is obtained in the BT-StC-03 sample, while the lowest stiffness is obtained in the BT-StC-01 sample. The fracture forces are in the range of 1585–1910 N, with samples BT-StC-02 and BT-StC-03 representing the highest load-bearing capacity within the group. The fact that the deflection values at the point of failure are in the range of 22.6–24.4 mm, while the maximum deflection values are mostly clustered around 27–29 mm, indicates that the StC group reached damage at similar deformation levels under bending; only the BT-StC-05 specimen deviates somewhat from the group with a higher maximum deflection value, suggesting that this may be related to the possible differences in the local fiber arrangement and damage development around the channel. These results demonstrate that specimens with star-shaped channel geometry are generally consistent within their own group in terms of stiffness and fracture behaviour, but exhibit a certain degree of variation in terms of fracture load and deflection values.

Table 4.9. Basic test parameters obtained from three-point bending tests of star-channelled (StC) CFRP test specimens (Nominal channel diameter Ø=3.3 mm)

Specimen code	**Thickness (mm)**	**Fracture Force (N)**	**Deflection at Fracture Force ($\delta_{@fracture}$ mm)**	**Max Deflection (δ_{max}, mm)**	**Elastic Region Slope (m, N/mm)**
BT-StC-01	3.745	1585.61	23.289	27.849	69.8237
BT-StC-02	3.867	1883.66	24.391	28.762	84.8333
BT-StC-03	3.814	1909.69	23.601	28.344	86.6878
BT-StC-04	3.786	1843.23	24.409	27.027	85.1961
BT-StC-05	3.702	1700.33	22.629	31.119	79.8074

When evaluated together with the data presented in Table 4.1 for the non-channelled (NC) group, the average elastic region slopes of the StC samples are significantly higher than the NC group (approximately 81 N/mm versus 59 N/mm), while the fracture forces are similar, and even slightly higher levels in some StC samples. In interpreting these differences, it should be taken into account that the star channel has a smaller cross-sectional area compared to other channel geometries, so the proportion of uninterrupted carbon fibers around the channel remains relatively high and therefore the sectional rigidity is preserved to a certain extent. Also, it is noteworthy that in the StC group, both the deflection values at the point of failure remained in the range of approximately 22.5–24.5 mm and the maximum deflection values mostly remained in the range of 27–31 mm; whereas in the NC samples, the failure and maximum deflection values generally occurred in the ranges of 31–35 mm and 33–38 mm, respectively. In other words, the StC specimens reach the same level of load as the NC group, and even higher load levels in some places, with much lower bending deformations; this shows that the star-shaped microchannel increases the section stiffness under bending while allowing a more limited deformation capacity compared to the non-channelled laminates.

4.5.4. Statistical Evaluation of StC (Star Channelled) Specimens (SD & COV Analysis)

Table 4.10 presents the statistical parameters (mean F_{max}, mean m, standard deviation, and COV) calculated for the fracture load (F_{max}) and the elastic region slope (m) obtained from three-point bending tests of star channel (StC) CFRP specimens. The coefficient of variation (COV) of approximately 7.70% obtained for the F_{max} values indicates that the fracture load in the StC group has a higher dispersion compared to the non-channelled and some other channel geometries, yet still offers an acceptable level of repeatability for the production of microchannel composites cured under hand lay-up and hot press. The fact that the COV value for the elastic region slope is approximately 8.49% suggests that the bending stiffness may be highly sensitive to the star channel geometry and, in particular, to stress concentrations developing around the sharp edges of the channel.

Table 4.10. Statistical parameters for the fracture load (F_{max}) and elastic region slope (m) values obtained from three-point bending tests on CFRP test specimens with star-shaped (StC) channels

Parameter	Unit	Mean	Standard Deviation (SD)	COV (%)
Fracture Force (F_{max})	N	1784.504	137.473	7.703
Elastic Region Slope	N/mm	81.269	6.903	8.494

When evaluated together with the statistical results given in Table 4.2 for the non-channelled (NC) group, it is seen that the average F_{max} of the StC samples is approximately 6% higher than the NC group. However, the fact that the COV for the m parameter is significantly higher in the StC group (≈8.5%) than in the NC group indicates that the bending stiffness in star-channel specimens is more affected by minor geometric and microstructural differences around the channel, and therefore the stiffness values are distributed over a wider range from specimen to specimen. During the lay-up and hot press process, effects arising from production, such as slight rotation of the star channel within the laminate, resin accumulation around the sharp edge regions, and fiber waviness, may cause both F_{max} and m values to exhibit a more distinct statistical dispersion in the StC group compared to the NC samples. In other words, the star channel section increases the average rigidity and load-bearing capacity in the StC group, but it can be said that it significantly increases statistical dispersion compared to the group without channels by raising its sensitivity to local geometric and microstructural irregularities around the channel.

4.6. Overall Comparison of Flexural Behaviour for Different Channel Geometries

In this section, the three-point bending test results for the NC, CC, SC, HC, and StC groups, presented separately in the previous subheadings, are combined to comprehensively evaluate the overall effect of microchannel cross-section geometry on bending behaviour. To make the comparison between channel geometries more systematic, a representative reference test specimen has been defined for each channel group.

When determining reference samples;

(ı) The force–deflection curve which representing the typical mechanical response within the group,(ıı) The modulus of elacity (E_f) of the reference sample to be selected should have values closest to the group average and,

(ııı) The criteria were based on the observed damage mechanism being consistent with the dominant fracture mechanism described in the relevant subheading.

As a result of this assessment;

- For the non-channelled group: BT-NC-03,
- For the circular channelled group: BT-CC-02,
- For the square channelled group: BT-SC-03,
- For the hexagonal channelled group: BT-HC-04,
- For the star-channelled group: BT-StC-02,

The relevant channel geometries have been accepted as reference bending specimens. Thus, by reducing the effect of experimental dispersion in each channel group, the contribution of the channel cross-section geometry to the bending response can be discussed more accurately.

The cross-sectional properties of the selected reference samples (especially the second moment of area, I) were calculated in the CAD environment. Using these data in equation 3.8, the modulus of elasticity (E_f) were calculated, and using them together with the elastic region slope (m), the flexural rigidity and cross-sectional efficiency of different channel geometries were compared quantitatively. The following subsections first examine the variation of the E_f and m parameters relative to the NC reference, then discuss the load-capacity–ductility balance based on the maximum load (F_{max}) and deflection values at failure. Finally, using a dimensionless bending shape factor defined based on these reference test specimens, the relative performance of different microchannel cross-section geometries compared to the non-channelled laminate is summarised.

4.6.1. Cross-Sectional Properties and Comparative Flexural Response of Reference Specimens

In this subsection, the cross-sectional properties of the reference specimens defined in the previous section are examined in comparison with their mechanical responses under bending loading. Firstly, cross-section areas and the second moment of area (I) values calculated from the cross-sections obtained with the coordinate measuring device (CMM) and reconstructed in the CAD environment based on point clouds representing the cross-sectional geometries are presented in Table 4.11. Thus, the geometric stiffness of different channel geometries around the bending axis can be compared quantitatively.

Following this, the modulus of elasticity (E_f) calculated using the slope (m) obtained from the elastic region of the load–deflection curves and the calculated I values, as well as the maximum load (F_{max}) and the deflection values at the point of failure, are summarised in Table 4.12. These parameters were evaluated together with the force-deflection curves presented in Figure 4.6 and the bending behaviour depending on the channel geometry was discussed comparatively.

Table 4.11. Technical drawings of the cross-sectional areas and second moment of the areas

Specimen Code	**Cross-Sectional Area**	**Minimum-Maximum Edge Thickness**	**Section Area (mm^2)**	**I (mm^4)**
BT-NC-03	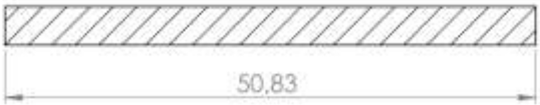	3.68-3.82	187.05	215.5
BT-CC-02		4.01-4.22	195.64	331.81
BT-HC-04	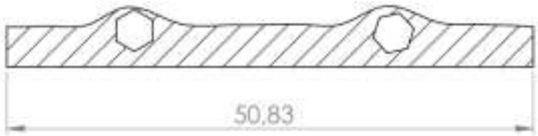	3.81-3.99	202.99	358.05
BT-SC-03	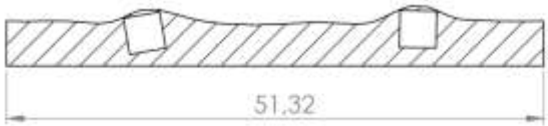	4.17-4.43	202.72	343.41
BT-StC-02	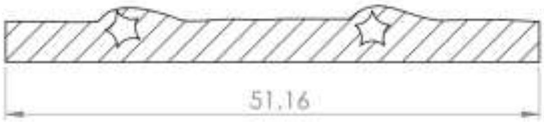	3.75-3.97	206.51	332.57

Table 4.11 shows that the cross-sectional area of the non-channelled reference test specimen (BT-NC-03) is 187.05 mm² and its second moment of area (I = 215.5 mm⁴) represents the lowest values. In microchannel samples, the cross-sectional area increases to a range of 195.64 to 206.51 mm² and shows an increase of approximately 5 to 10% compared to the non-channelled cross-section. In contrast, the second moment of area in the same specimens increases to a range of 331.81–358.05 mm⁴, and the I values increase by approximately 50–65% compared to BT-NC-03. This situation indicates that the positional distribution of the material relative to the neutral axis changes significantly with the formation of microchannels. Especially, the corrugated geometry formed on the upper surface around the channel and the associated local elevation/thickness increases show that the section stiffness around the bending axis has increased much more significantly compared to the limited increase in the section area.

In line with this evaluation, in the next step, the force–deflection curves of the reference samples of each channel group were compared on the same graph in Figure 4.6; the elastic region slope (m), effective modulus of elasticity (E_f), maximum load (F_{max}) and deflection at failure ($\delta_{failure}$) values are summarized in Table 4.12. By evaluating this graph and table together, the comparative bending behaviour of different channel geometries has been examined in detail.

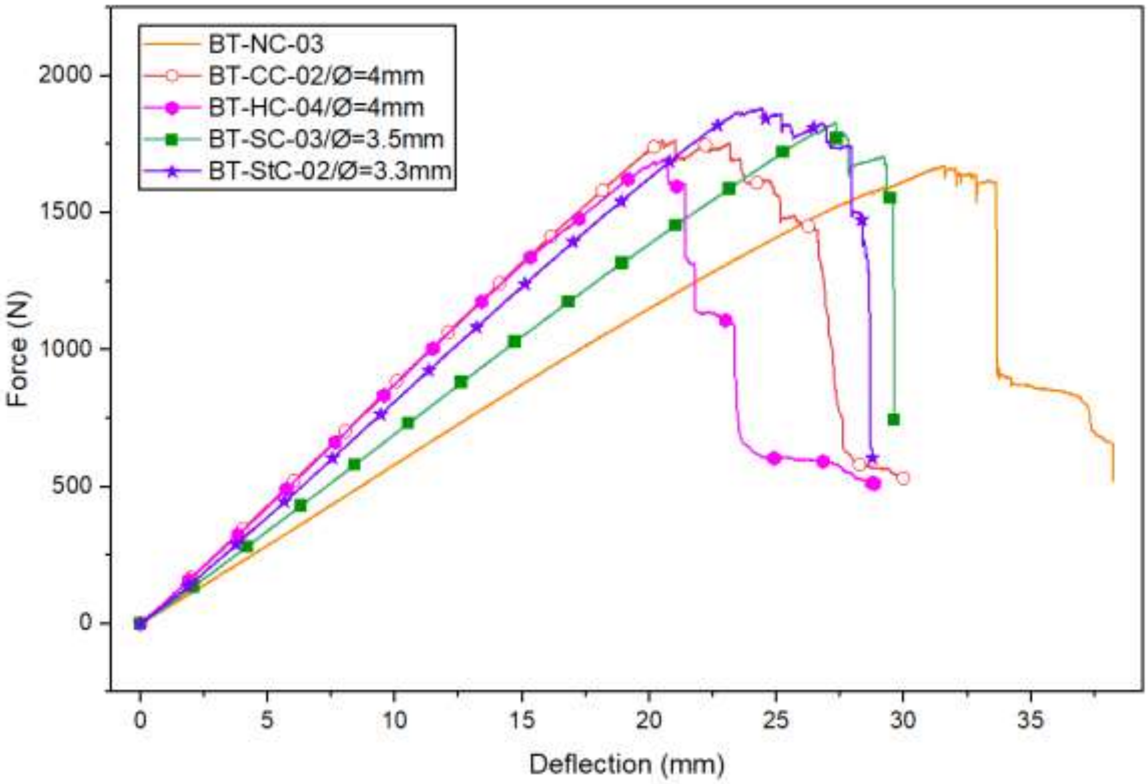

Figure 4.6. Load–deflection curves for the non-channelled reference sample (BT-NC-03) obtained from three-point bending tests and samples with different microchannel geometries (BT-CC-02, BT-HC-04, BT-SC-03, BT-StC-02). The graph illustrates the effect of channel geometry on initial stiffness, maximum load-carrying capacity, and post-peak fracture behaviour

Table 4.12. Fundamental test parameters obtained from three-point bending tests of reference CFRP test specimens

Specimen Code	Average Edge Thickness (mm)	Fracture Force (N)	Deflection at Fracture Force ($\delta_{@fracture}$ mm)	Max Deflection (δ_{max}, mm)	Elastic Region Slope (m, N/mm)	Modulus of Elasticity (E_f, GPa)
BT-NC-03	3.86	1671.61	31.563	38.236	59.39	71.697
BT-CC-02	4.06	1765.88	20.49	27.13	87.38	78.263
BT-HC-04	3.85	1698.84	20.66	28.852	86.69	61.213
BT-SC-03	4.27	1828.64	27.31	29.602	70.71	69.190
BT-StC-02	3.867	1883.66	24.39	28.762	84.83	62.134

When the values for the elastic zone slope (m) and bending modulus (E_f) given in Table 4.12 are evaluated together with the load–deflection curves in Figure 4.6, the effect of the channel geometry on the bending stiffness becomes more clearly apparent. In terms of elastic region slope (m), all microchannel samples exhibited greater value compared to the non-channel reference (BT-NC-03, 59.39 N/mm). In particular, circular and hexagonal channelled specimens (BT-CC-02 and BT-HC-04) exhibited the highest elastic region slope with approximately 45–50 percent higher slope values, while the star-channelled specimen (BT-StC-02) also showed a similarly high slope. To verify the validity of these trends at the group level, the mean and standard deviation of the elastic region slope (m) for each test group are summarised in Figure 4.7.

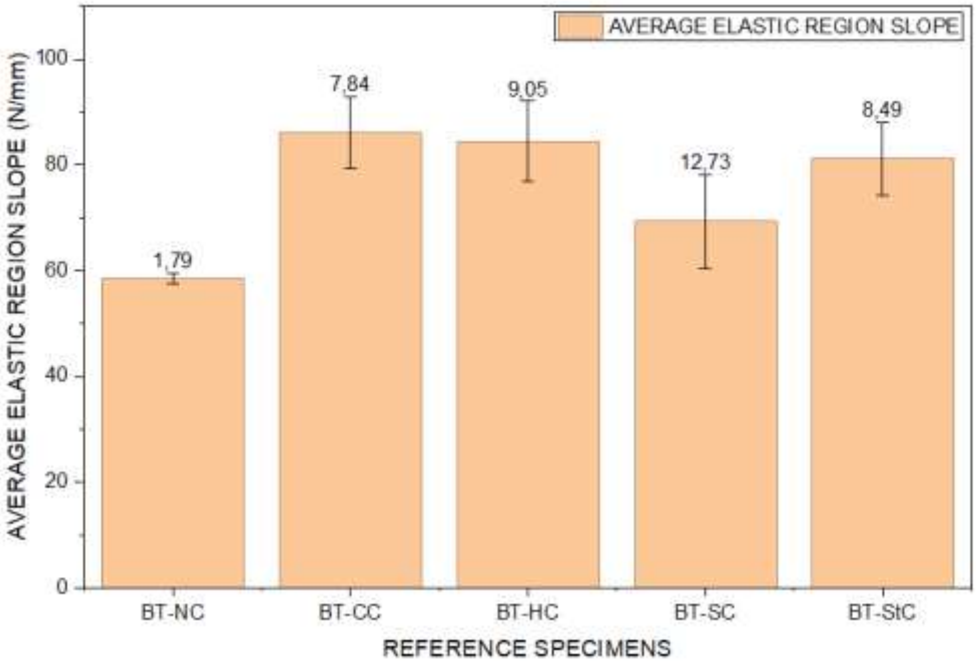

Figure 4.7. Bar chart of the average elastic region slope for each test group, with coefficients of variation (COV)

The elastic modulus of the square-channelled specimen (BT-SC-03) has increased by approximately 20% compared to the non-channelled specimen. However, when the effect of I is evaluated using Equation 3.8 on the bending modulus, a different ranking emerges among the channel geometries (Figure 4.8). The highest value in terms of modulus of elasticity was obtained in the circular-channelled sample (BT-CC-02, ~78 GPa), showing an increase of approximately 9% compared to the non-channelled sample. The flexural modulus of the square-channelled sample (BT-SC-03, ~69 GPa) decreased by a very small amount (4%) compared to the non-channelled sample, while the E_f values of the star- and hexagonal-channelled samples (BT-StC-02 and BT-HC-04, ~62 GPa) E_f values were approximately 13–15% lower than those of the NC. In other words, although hexagonal and star channel geometries increase the cross-sectional moment of inertia, this advantage provided by the cross-sectional geometry is not fully reflected in the effective flexural modulus due to greater disruption of fiber continuity and stress concentrations around the angular channel. On the other hand, the circular channel increases I and also disrupts the fiber arrangement less than other geometries, thus achieving the highest level of rigidity in terms of both m and E_f.

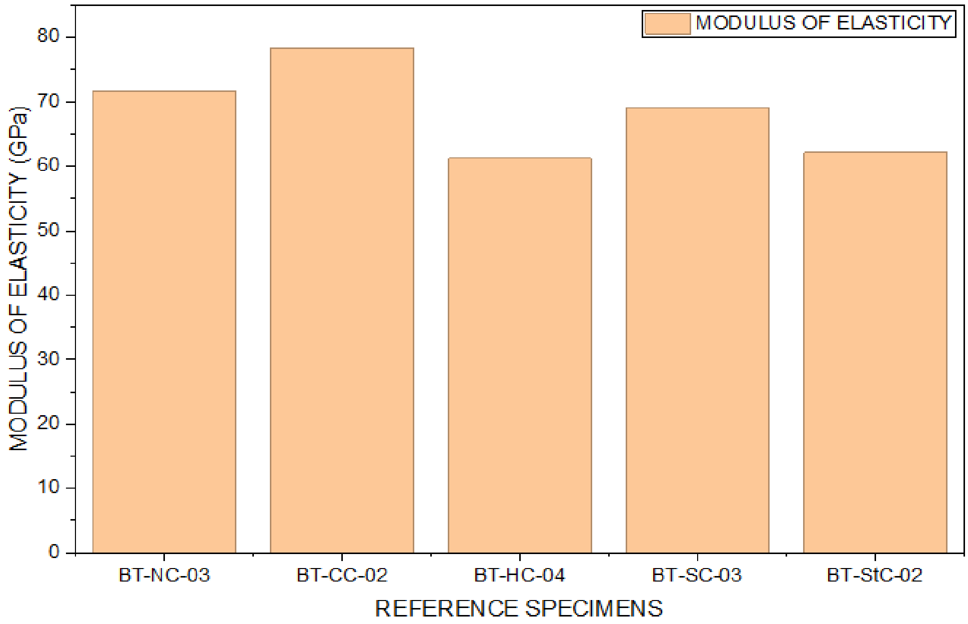

Figure 4.8. Comparison of flexural modulus (E_f) values for the reference specimens of each channel geometry

When focusing on the post-peak load region, the positions of the channel geometries in terms of ductility and brittleness become more pronounced relative to each other. When Figure 4.6 and Table 4.12 are considered together, it can be seen that the deflection range from peak load to final fracture ($\Delta\delta = \delta_{max} - \delta_{fracture}$) varies depending on the channel geometry (Table 4.13).

Table 4.13. Deflection values at failure initiation (δ_f), maximum deflection (δ_{max}), and post-failure deflection ($\delta_{max}-\delta_{failure}$) obtained from three-point bending tests (ASTM D790) for the reference specimens

Specimen Code	Deflection at failure initiation ($\delta_{@failure}$, mm)	Max Deflection (δ_{max}, mm)	Post Failure Deflection ($\delta_{max} - \delta_{@failure, mm}$)
BT-NC-03	31.563	38.236	6.67
BT-CC-02	20.49	27.13	6.64
BT-HC-04	20.66	28.852	8.192
BT-SC-03	27.31	29.602	2.292
BT-StC-02	24.39	28.762	4.372

In the non-channelled reference specimen (BT-NC-03), fracture load occurs at approximately $\delta_{fracture} \approx 31.6$ mm, load-bearing capacity continues to decrease gradually up to $\delta_{max} \approx 38.2$ mm, and a post-peak deformation range of $\Delta\delta \approx 6.7$ mm emerges. In the circular-channel specimen (BT-CC-02), the peak load is obtained at approximately $\delta_{fracture} \approx 20.5$ mm, the curve progresses to a lower load level up to $\delta_{max} \approx 27.1$ mm, and a similar magnitude of post-peak deflection range ($\Delta\delta \approx 6.6$ mm) is observed. In the hexagonal channel specimen (BT-HC-04), $\delta_{fracture} \approx 20.7$ mm and $\delta_{max} \approx 28.9$ mm, reaching the widest post-peak deformation range with $\Delta\delta \approx 8.2$ mm. In these two configurations (circular and hexagonal), the hexagonal channel specimen continues to deform for an additional few millimetres beyond the peak load point before fully settling, suggesting that damage progresses gradually through mechanisms such as fiber breakage, matrix cracking, and delamination, and that the bending behaviour exhibits a relatively ductile character. In contrast, the square-channel specimen (BT-SC-03) exhibits the smallest post-peak deformation range ($\Delta\delta \approx 2.3$ mm), while the star-channel specimen (BT-StC-02) shows a moderate post-peak deformation range ($\Delta\delta \approx 4.4$ mm); this indicates that the square channel geometry has the most brittle fracture character, while the star geometry has a more brittle fracture character in terms of ductility compared to the non-channelled specimens.

When evaluated overall, the non-channelled reference section (BT-NC-03) represents classic three-point bending behaviour; despite having the lowest cross-sectional area and second moment of area (I), it offers a high level of performance in terms of effective bending modulus (E_f) and maximum load (F_{max}). Circular channelled cross-section (BT-CC-02), provides a significant increase in sectional moment of inertia while minimally disrupting fiber continuity and causing the most limited stress concentration around the channel. Therefore, it delivers superior results in most cases compared to NC in terms of elastic region slope (m), E_f (modulus of the elasticity) and F_{max}, and stands out as the most balanced solution among microchannel configurations in terms of bending performance. The square-channel cross-section (BT-SC-03), on the other hand, exceeds the NC by a certain amount in terms of m and I; with its E_f and F_{max} values, it represents a structurally acceptable intermediate solution where the bending performance is generally maintained.

In the hexagonal channel cross-section (BT-HC-04), despite the cross-sectional area and I values reaching their highest levels and the elastic region slope being relatively high, E_f and F_{max} remain significantly lower compared to the NC and CC configurations due to fiber misalignment and early damage development associated with the polygonal geometry around the channel; thus exhibiting limited performance in terms of stiffness efficiency. On the other hand, the fact that it is one of the configurations with the widest deformation range ($\Delta\delta$) from peak load to ultimate failure indicates that the hexagonal cross-section exhibits one of the most pronounced ductile fracture behaviours among the cross-sections within the scope of the study. The star channel cross-section (BT-StC-02), although close to the circular channel in terms of cross-sectional area and I, stands out as the configuration that most disrupts the fiber architecture due to its most complex and polygonal channel geometry; while it forms one of the two groups with the lowest E_f values along with BT-HC-04, its F_{max} value reaches the highest level among the reference samples. At this point, it should also be noted that the cross-sectional area of the star channel is approximately one-third of the cross-sectional areas of the other channel geometries. If the cross-sectional area of the star channel were brought to a similar level with other geometries, both E_f and F_{max} values would be expected to be lower than the current results, as fiber discontinuity and stress concentration would occur over a wider area. Therefore, the results belonging to the StC group should not be directly compared with other configurations that have the same channel area. Instead, it can be considered as a situation representing the upper limit of bending performance that can be achieved with a geometrically complex channel design covering a relatively small area within the cross-section. These findings provide a basis for interpreting the bending shape factor, which will be defined in the next subsection, also provides a basis for discussing the cross-sectional efficiency of different channel geometries compared to a non-channelled reference section.

4.6.2. Shape Factor – Rigidity – Specific Performance Analysis

In the previous sections, the load–deflection response and damage observations of each channel geometry were examined separately. In this section, rigidity, specific performance and cross-section efficiency are evaluated together in order to compare different channel groups within a single framework the F_{max}/δ_{max} ratio represents the average stiffness corresponding to the peak load. However, as damage that may occur when approaching the peak load can affect this ratio, the slope (N/mm) obtained from the elastic (linear) region of the load–deflection curve has been used in comparisons to more accurately represent the elastic behaviour. Additionally, to eliminate the effect of different test spans, the bending stiffness (S_B) was calculated using equation 3.9, and to account for the mass effect, the results were normalised using the mass per unit length (μ, equation 3.10) to obtain specific indicators from equations 3.11 and 3.12. Finally, the bending shape factor (Ψ_B^e) was defined to express the cross-sectional efficiency of the channel geometries relative to the non-channelled reference cross-section (Table 4.14), and all configurations were comprehensively compared using these metrics.

Table 4.14. Comparison of bending stiffness, specific performance and bending shape factor values according to channel geometries

Specimen Code	Shape Factor (Ψ_B^e)	Mass Per Unit Length (μ ,g/mm)	Bending Stiffness (S_B) (×10^5 N.mm^2)	Specific Bending Stiffness (S_B^*) (×10^5 N.mm^3/g)	Failure Load (F_{max}) (N)	Specific F_{max} (F_{max}^*) (N.mm/g)
BT-NC-03	1	0.2985	154.507	517.507	1671.61	5598.886
BT-CC-02	1.680	0.3128	259.687	829.972	1765.88	5643.833
BT-HC-04	1.418	0.2985	219.178	734.153	1698.84	5690.389
BT-SC-03	1.537	0.3083	237.610	770.699	1828.64	5931.279
BT-StC-02	1.337	0.3016	206.642	685.029	1883.66	6244.430

Table 4.14 presents a comparative analysis of the bending performance of channel geometries based on both the elastic region stiffness (S_B) and specific indicators (normalised by mass) S_B^* and F_{max}^*. According to the normalisation performed by assuming Ψ_B^E=1 for the non-channelled reference sample (BT-NC-03), the bending stiffness and the associated shape factor ranking were obtained as BT-CC-02 > BT-SC-03 > BT-HC-04 > BT-StC-02 > BT-NC-03 (Figure 4.9). The circular channel (BT-CC-02) increased the rigidity by approximately 68% compared to the reference (Ψ_B^E=1.680), followed by the square and hexagonal channels with increases of approximately 54% and 42%, respectively. The star channel (BT-StC-02) provided an increase in rigidity (Ψ_B^E = 1.337) but lagged behind the other channel geometries in terms of rigidity-based cross-sectional efficiency.

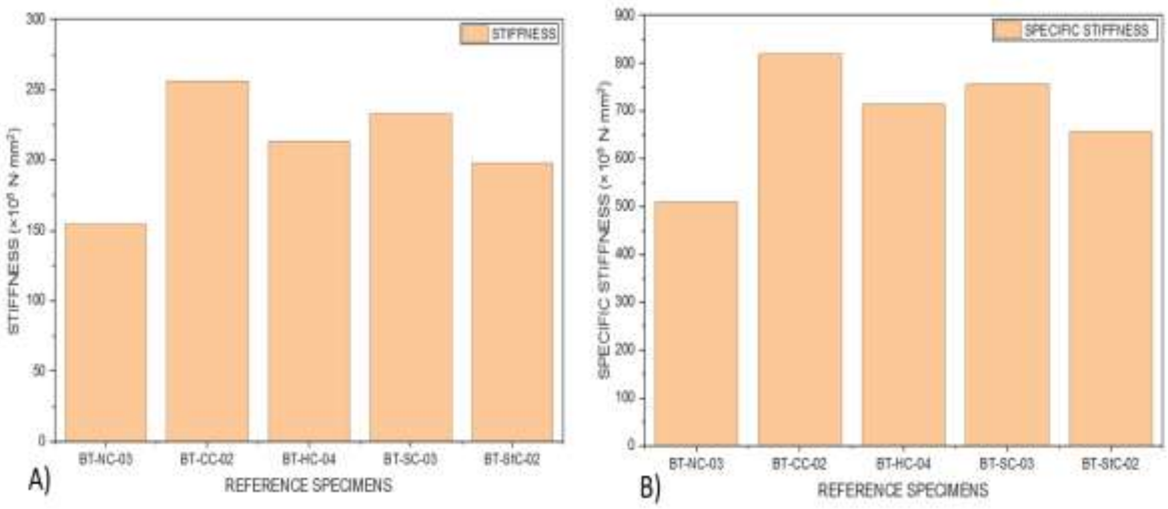

Figure 4.9. Comparative bending performance of the selected reference specimens: (A) bending stiffness (SB) derived from the elastic region slope of the load–deflection response, and (B) specific bending stiffness S_B^* obtained by normalising SB with mass per unit length

The mass per unit length (μ) values remaining within the range of 0.2985–0.3128 g/mm (approximately a 3% variation) does not fundamentally alter the general trend of mass normalisation. Indeed, in terms of specific bending stiffness (S_B^*), the highest value is observed in BT-CC-02, providing an improvement of approximately 60% compared to the non-channelled reference. This finding demonstrates that the circular channel geometry increases not only the absolute stiffness but also the stiffness efficiency per unit mass.

When evaluated from a design perspective, the BT-CC-02 configuration stands out in applications where rigidity and specific rigidity are the primary performance criteria. In situations where load-carrying capacity is critical, BT-StC-02 is noteworthy because it can maintain high F_{max} and F_{max}^* values at the lower channel area/gap ratio level used in this study; however, as the channel area was not equalised for comparison, these results should not be interpreted as a "direct superiority". In an approach that considers both rigidity gain and load-carrying capacity, BT-SC-03 can be considered a more balanced option as it offers high values on both performance axes.

4.7. Drop-Weight Impact Results and Graph-Based Discussion

4.7.1. Test Overview and Data Presentation

In this subsection, the behaviour of samples with different microchannel cross-sectional geometries (Circular, Hexagonal, Square, Star) under drop weight impact loading has been compared with non-channelled (NC) reference test samples under the same experimental conditions. In accordance with the test parameters given in Section 3, experiments were conducted using a hemispherical impact tip and a clamped fixture at a nominal impact energy of 30 J. The test procedure and sample placement were carried out in accordance with the fundamental principles of the ASTM D7136/D7136M standard. Within this scope, five samples measuring 100 × 150 mm were tested for each channel group.

The impact load was applied to the flat outer surfaces of the specimens, not to the surfaces adjacent to the channels. The selected impact direction has been determined according to a recently patented design (PCT/TR2024/050272; TR2024/002940). According to this design, in a representative battery casing configuration, the most likely impact is expected to occur on the surface without channels, as the surface adjacent to the channel is usually in direct contact with the battery cells to ensure effective thermal management.

The aim of this section is to show the effects related to the channel geometry directly to the reader through graphs, rather than identifying numerous samples individually. In this regard, the impact response has been evaluated using two basic sets of graphs: force–displacement curves and force–time and energy–time curves. In this regard, force–displacement curves were first presented; within each channel group, all samples were plotted separately to observe intra-group behaviour, and then a "representative (reference) sample" was selected for each group to simplify inter-group comparisons. Representative samples were selected from among those exhibiting behaviour closest to the average maximum force and average absorbed energy values in the relevant group; these were combined with the selected non-channelled (NC) reference curve on a single graph, enabling direct comparison of the impact responses of different channel geometries. Load-displacement curves showing the deflection amount as a function of impact force are given in Figures 4.10–4.14. Please note that in these graphs, force is expressed in Newtons (N), displacement in millimetres (mm), and time in milliseconds (ms).

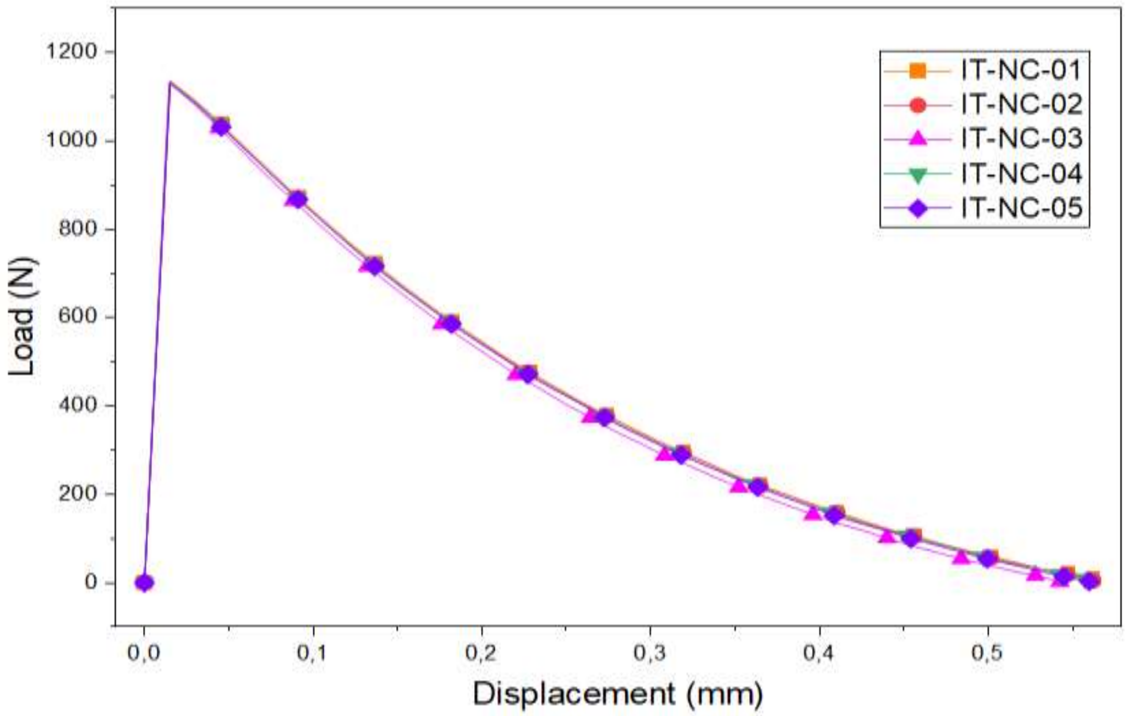

Figure 4.10. Load–Displacement curves of the non-channelled (NC) specimens obtained from drop weight impact (DWI) tests

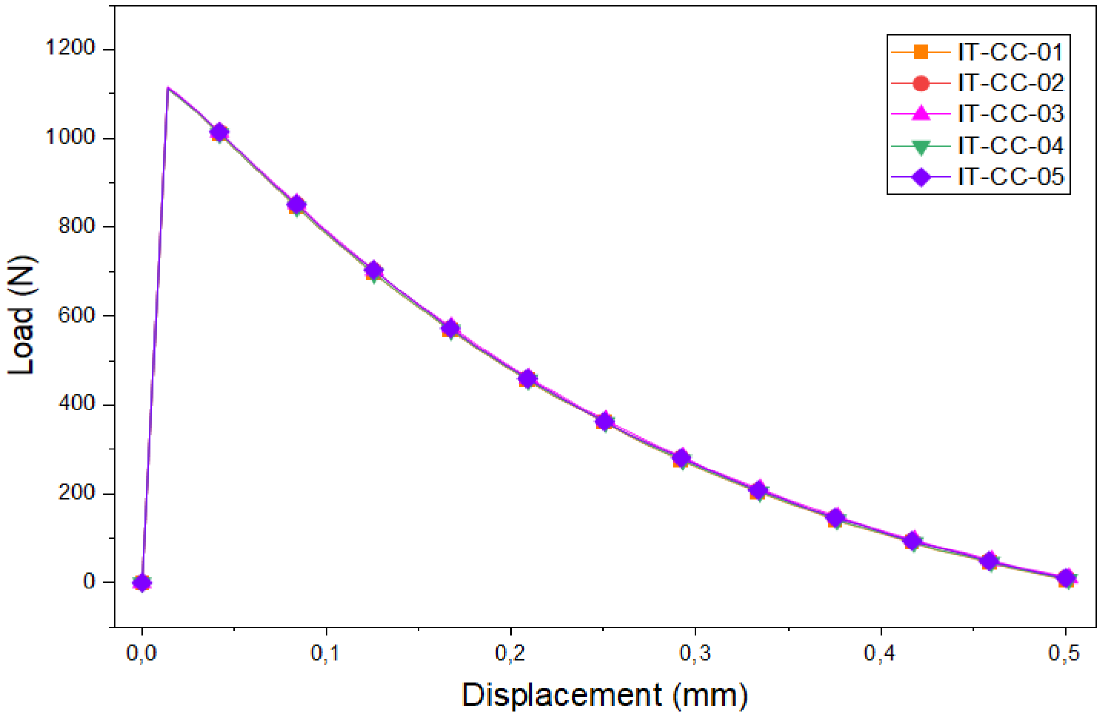

Figure 4.11. Load–Displacement curves of the circular-channelled (CC) specimens obtained from drop weight impact (DWI) tests (Nominal channel diameter Ø=4 mm)

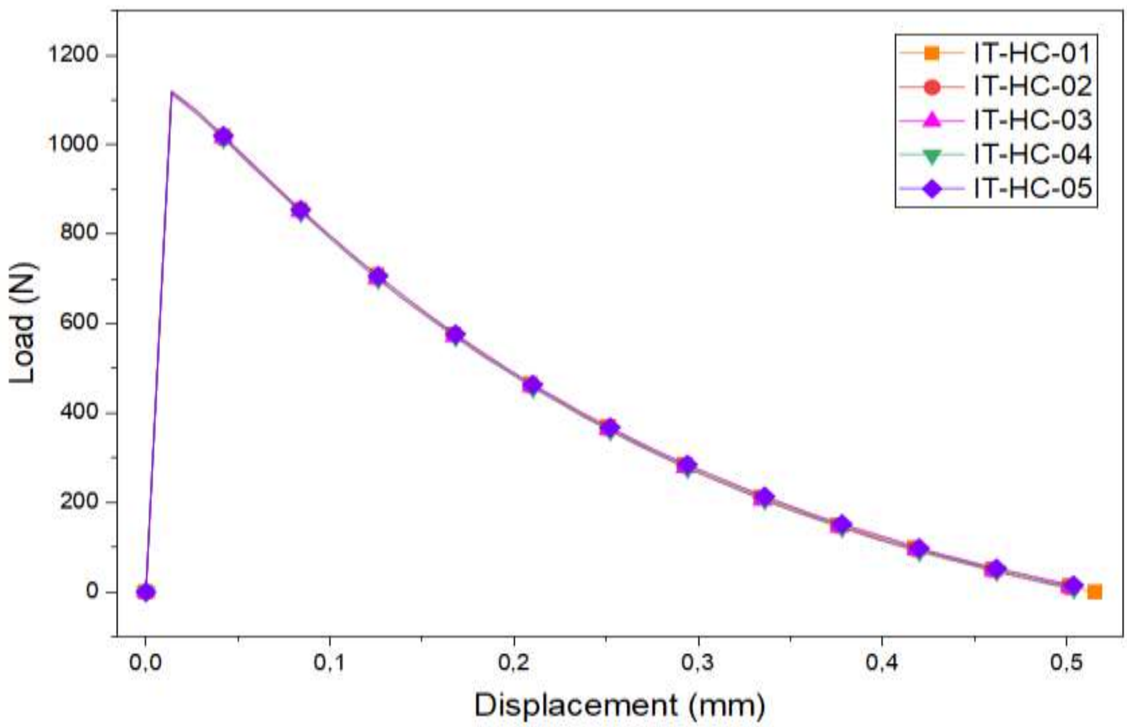

Figure 4.12. Load–Displacement curves of the hexagonal-channelled (HC) specimens obtained from drop weight impact (DWI) tests (Nominal channel diameter Ø=4 mm)

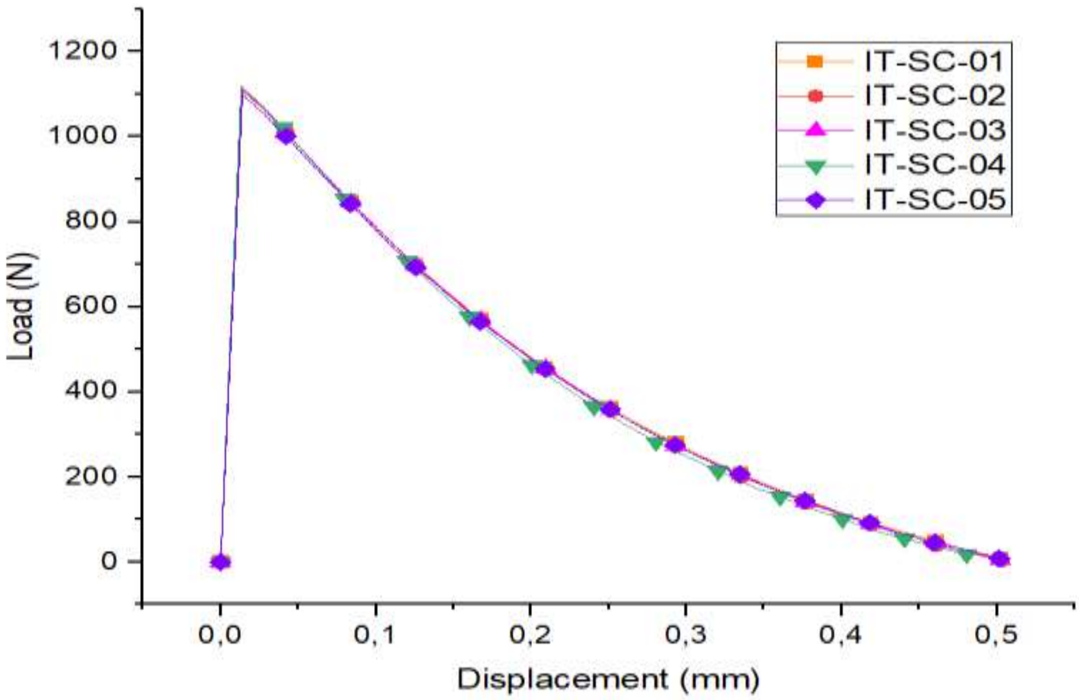

Figure 4.13. Load–Displacement curves of the square-channelled (SC) specimens obtained from drop weight impact (DWI) tests (Nominal channel diameter Ø=3.5 mm)

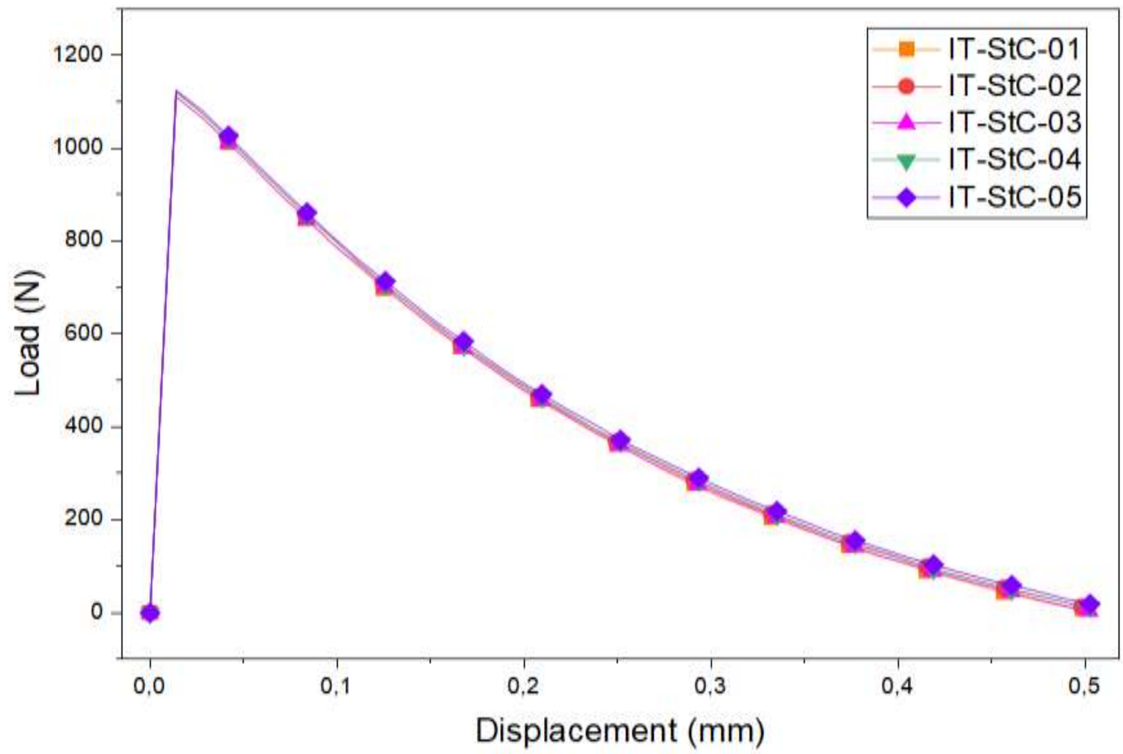

Figure 4.14. Load–Displacement curves of the star-channelled (StC) specimens obtained from drop weight impact (DWI) tests (Nominal channel diameter Ø=3.3 mm)

The load–displacement curves provided on the previous pages illustrate a typical impact response for all configurations. Following the initial contact between the impactor and the sample, the load increases rapidly at very small displacement values to reach a peak value. After the peak load, the load gradually decreases as the displacement increases. The peak region represents the initial effective stiffness and contact hardness of the test specimens, while the decreasing portion after the peak corresponds to a decrease in structural stiffness and greater energy dissipation through damage mechanisms as various types of damage (such as matrix cracking, interlaminar separation/delamination, and local fiber breaks) come into play. In this context, the general form of the curves shows that the impact response reaches its peak value quickly and then gradually decreases during the contact period, exhibiting a rapid peak followed by drop.

The graphs also show that intra-group repeatability is high. The fact that the curves for different samples largely overlap in each channel group indicates that production quality and test conditions are consistent. It is expected that the observed minor deviations will become more pronounced, particularly in the region following peak load. These differences may be due to local microstructural heterogeneities (fiber orientation, resin-rich zones, discontinuities around channels), small thickness/placement variations, or tolerances in boundary conditions. These results are summarized in the following graph (Figure 4.15); they allow for a direct comparison of the effect of different microchannel geometries on impact response using samples representing each group, and provide a solid basis for intergroup evaluation.

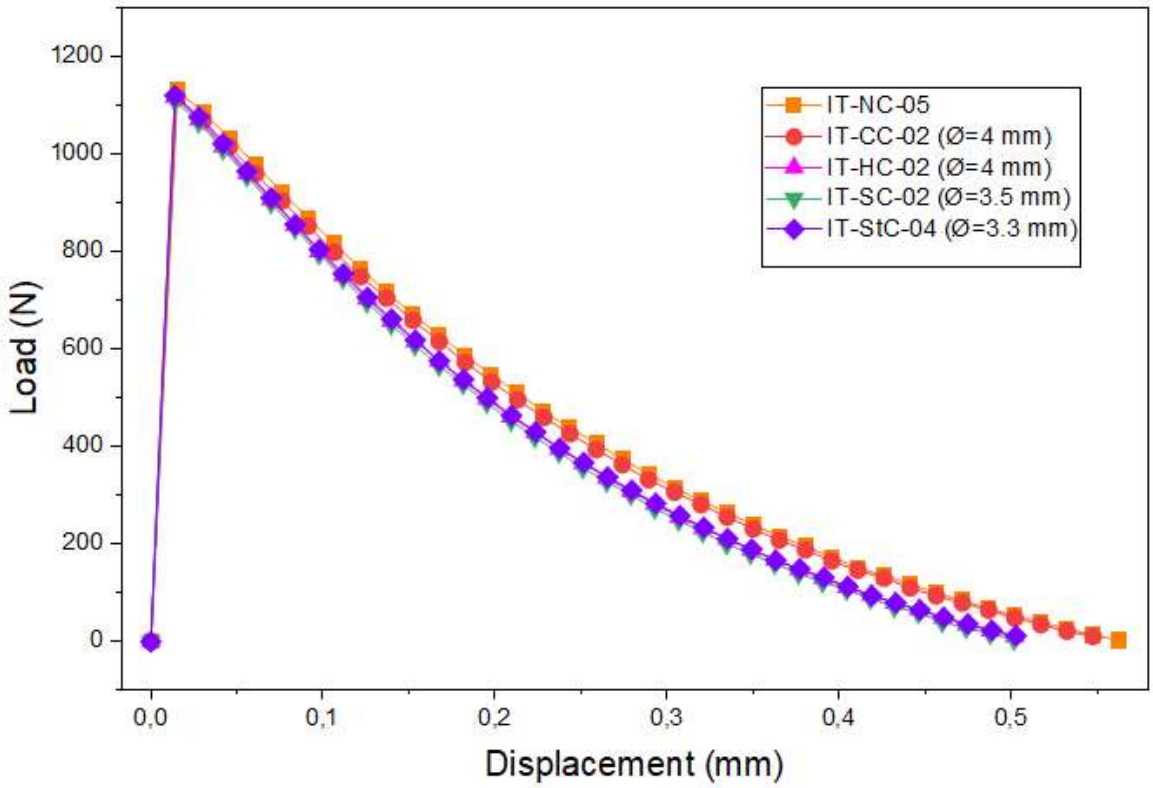

Figure 4.15. Comparison of load–displacement curves for representative samples selected for each channel geometry using a non-channelled (NC) reference sample within the scope of drop weight impact (DWI) tests (Ø represents the nominal channel diameter)

These representative load-displacement curves show that all configurations reach very similar peak load values and the overall curve shape is similar. However, in the post-peak load region, channelled specimens carry lower loads compared to channelless (NC) specimens at the same displacement levels; this difference is particularly pronounced in SC (square channel) and StC (star channel) configurations. This finding suggests that while microchannel geometry has a limited effect on peak load, the decrease in effective rigidity and load-carrying capacity as damage progresses varies slightly depending on the channel geometry. Furthermore, it can be observed from the graph that the curve of the circular channelled (CC) specimen is closest to the non-channelled (NC) specimen; while the curves of the square channelled (SC) and star channelled (StC) specimens show earlier load response loss in the post-peak region.

When examining studies about the low-velocity impact (LVI) on literature, it can be seen that load–energy–time plots are frequently used to describe the impact response of materials. These plots help track how the contact force and the absorbed energy evolve throughout the impact event. The relevant graphs of the present study are presented in Figures 4.16–4.20.

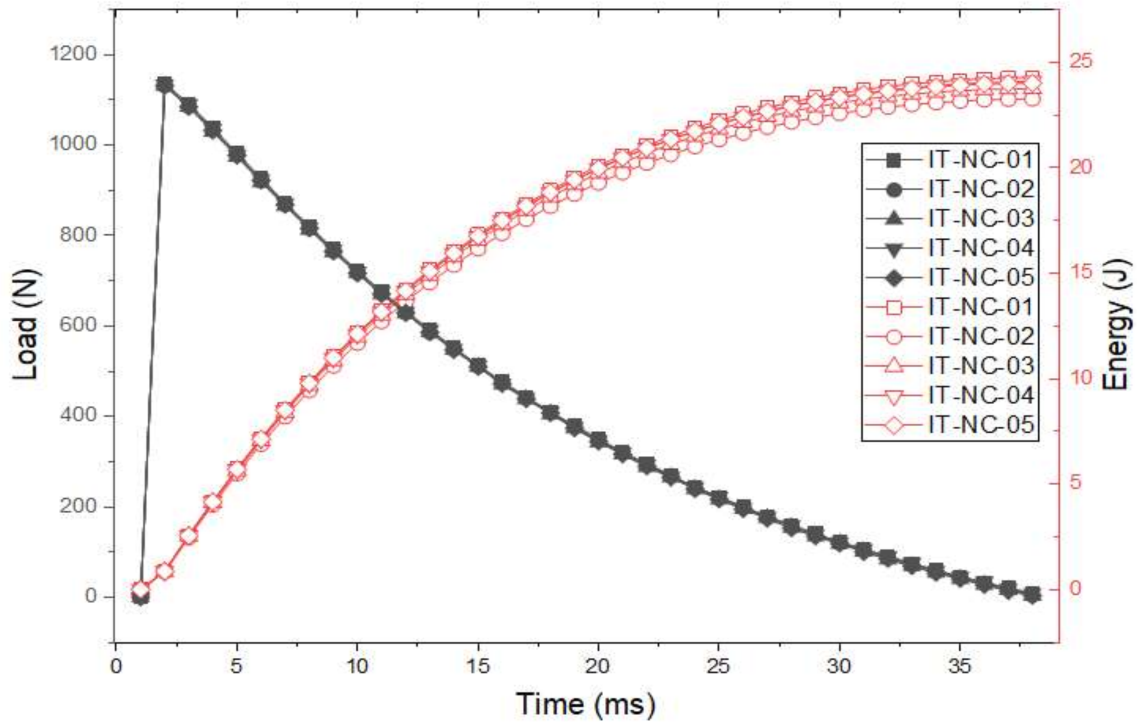

Figure 4.16. Load-Time and Energy-Time curves obtained from drop weight impact (DWI) tests of non-channelled (NC) specimens

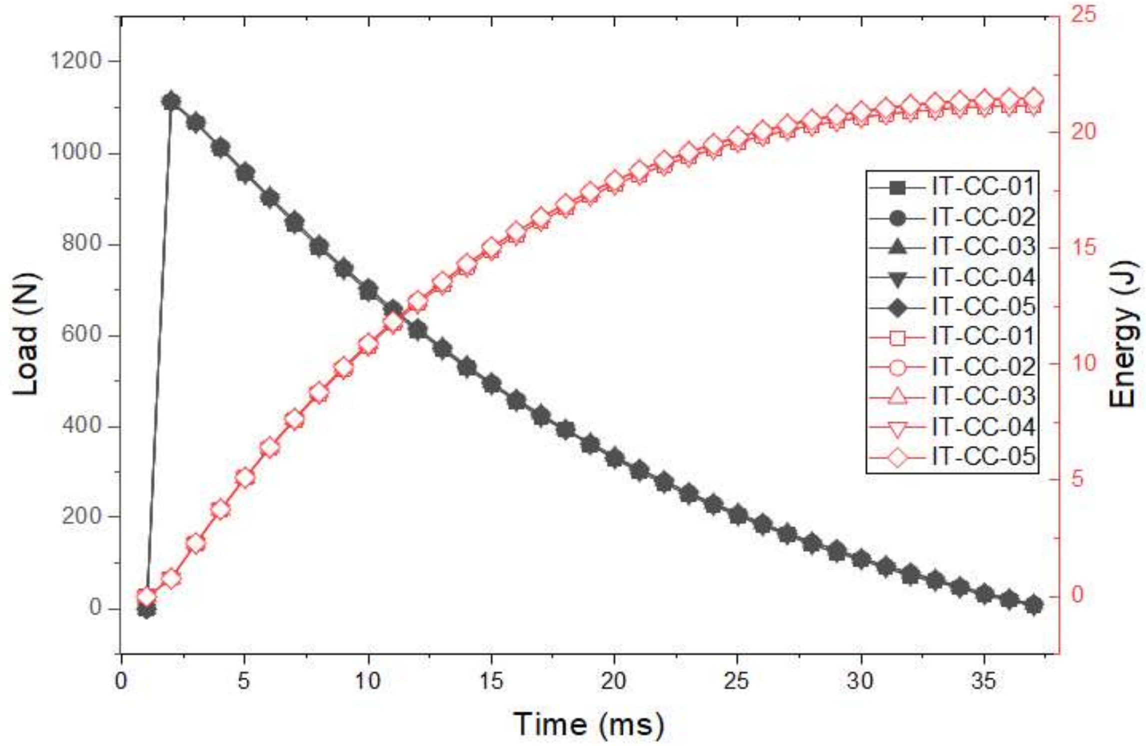

Figure 4.17. Load-Time and Energy-Time curves obtained from drop weight impact (DWI) tests of circular channelled (CC) specimens (Nominal channel diameter Ø=4 mm)

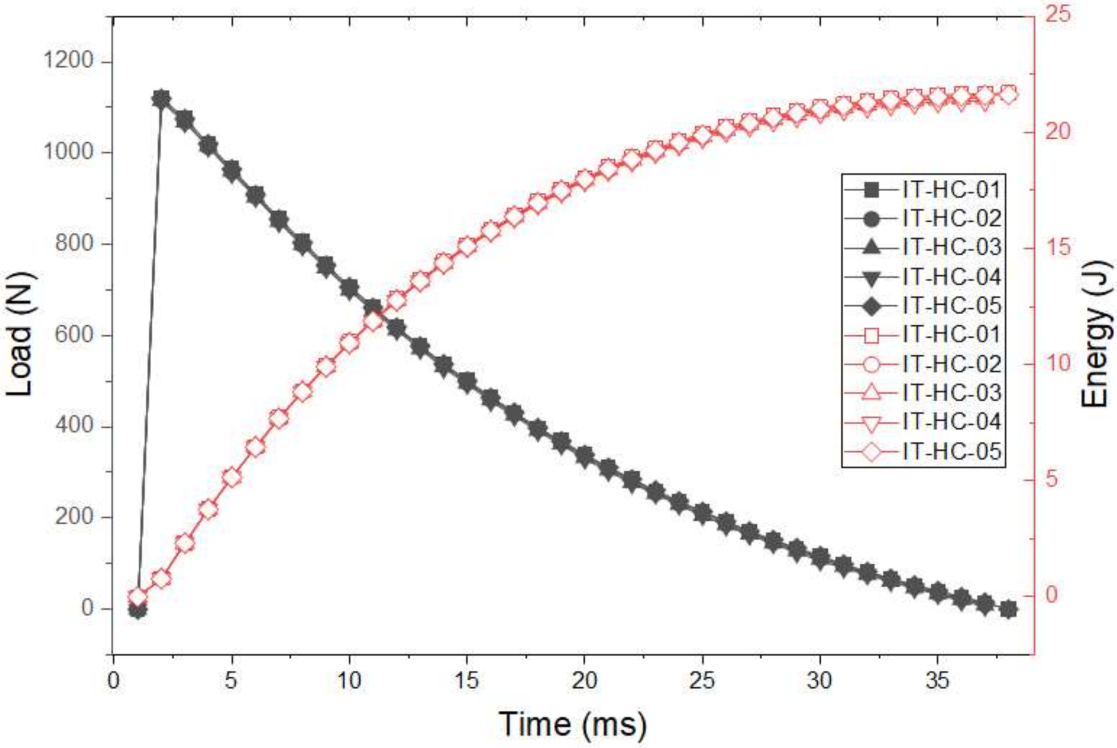

Figure 4.18. Load-Time and Energy-Time curves obtained from drop weight impact (DWI) tests of hexagonal channelled (HC) specimens (Nominal channel diameter Ø=4 mm)

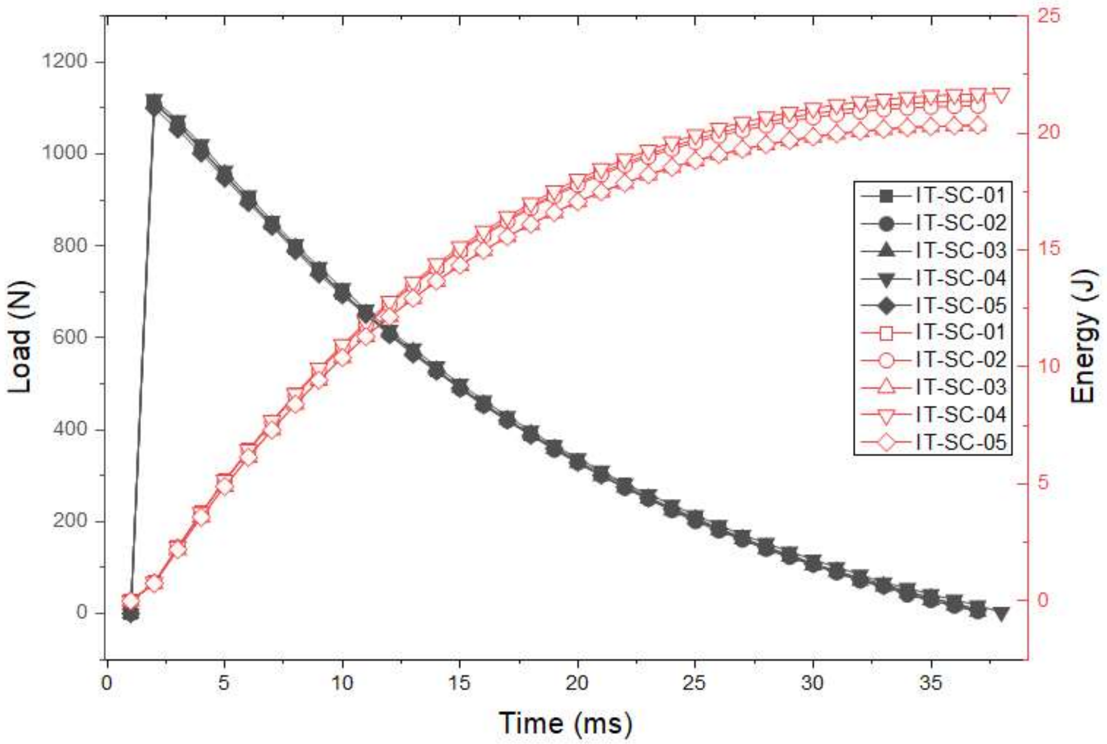

Figure 4.19. Load-Time and Energy-Time curves obtained from drop weight impact (DWI) tests of square channelled (SC) specimens (Nominal channel diameter Ø=3.5 mm)

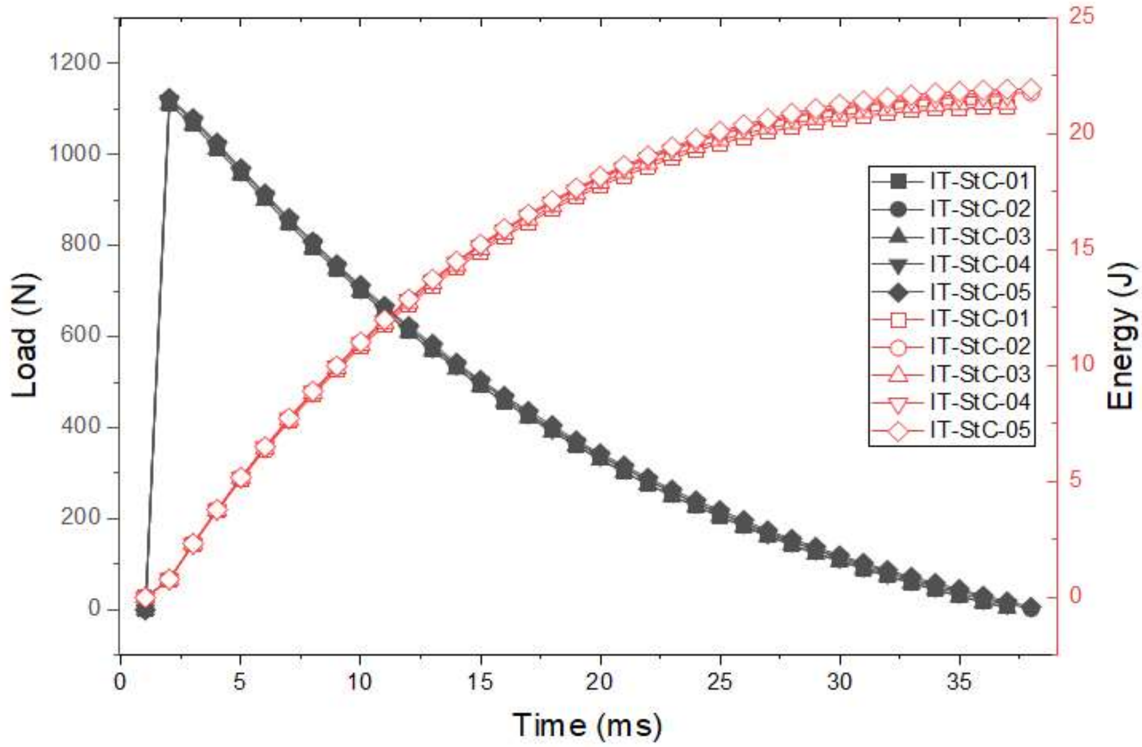

Figure 4.20. Load-Time and Energy-Time curves obtained from drop weight impact (DWI) tests of star channelled (StC) specimens (Nominal channel diameter Ø=3.3 mm)

All of the load–time and energy–time graphs provided on the previous pages indicate that the impact event progressed with a similar character. In all groups, the load increases very rapidly in the first moments of the impact, reaching its peak value within a few milliseconds, then gradually decreases as contact continues, approaching zero at the end of the impact duration. In contrast, the energy-time curves show a continuous increase, approaching a limiting value as the contact ends. This limit represents the total energy absorbed by the relevant sample during the impact; the rate of increase in the first part of the curve provides a direct indication of how quickly the energy was absorbed.

These general trends indicate that a similar impact characteristic is maintained in each channel group. However, in order to show the differences related with microchannel geometry more clearly, load–time and energy–time curves for representative samples which selected for each group accordance to selection criteria defined in the previous section have been combined on a single graph and presented in Figure 4.21. This comparison enables a direct assessment of the effect of different channel geometries on load transfer and energy absorption during impact.

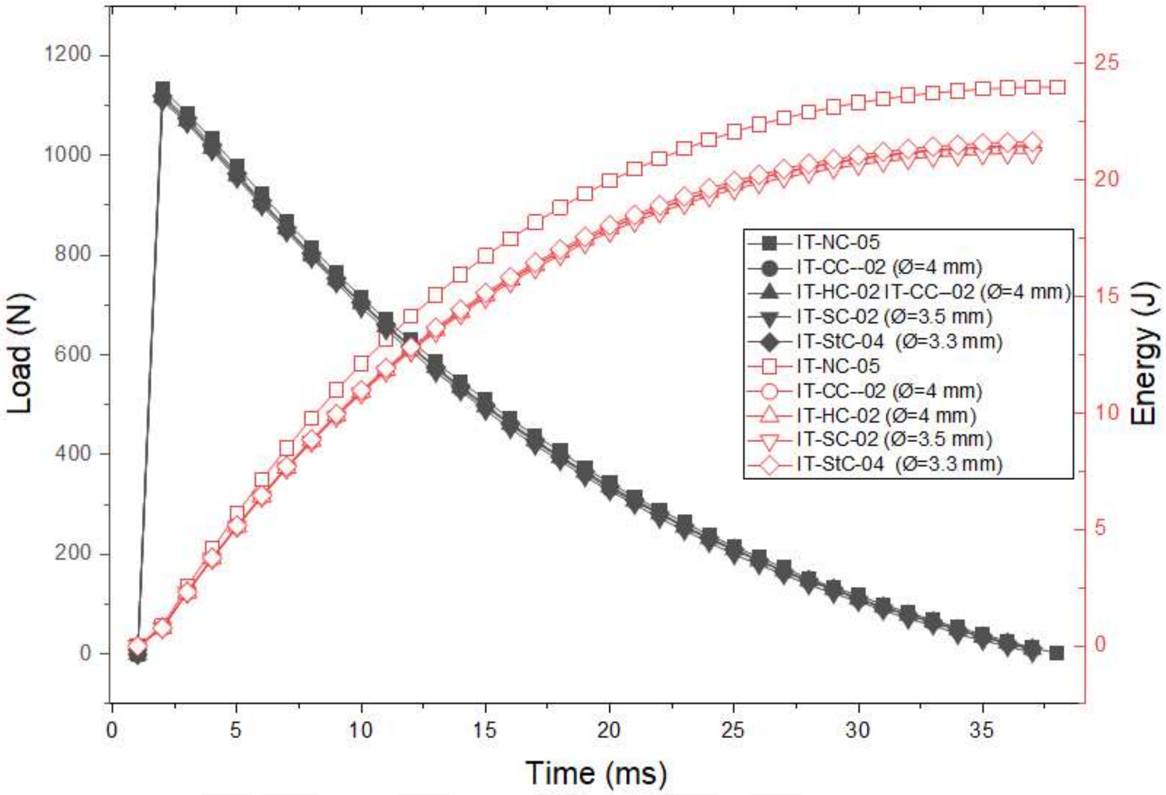

Figure 4.21. Comparison of load-time and energy-time curves of non-channelled (NC) reference specimens and representative specimens selected for each channel geometry within the scope of drop weight impact (DWI) experiments (Ø represents the nominal channel diameter)

Table 4.15. Summary of DWI test results for each specimen group

Specimen Group Name	Drop Energy (J)	Mean Absorbed Energy (J)	Minimum Peak Force (N)	Mean Peak Force (N)	Maximum Peak Force (N)	Mean Total Displacement (mm)
Non Channelled	30	23.93	1131.53	1133.31	1136.90	0.557
Circular Channelled	30	21.32	1111.36	1113.51	1116.74	0.501
Hexagonal Channelled	30	21.53	1112.71	1117.01	1120.77	0.507
Square Channelled	30	21.14	1100.02	1110.44	1119.43	0.500
Star Channelled	30	21.57	1110.02	1117.55	1124.80	0.507

Figure 4.21 presents the load–time and energy–time responses of representative samples selected for each channel geometry in a comparative manner on the same axis. When examining the load-time curves, it is observed that all configurations rapidly reach peak load in the first milliseconds of the impact and then gradually decrease during the contact period, approaching zero at the end of the event. The significant overlap of the curves indicates that load transfer and contact duration during impact exhibit similar characteristics regardless of the channel geometry.

When the energy-time curves and Table 4.15, which summarizes the data related to these curves, are examined together, the differences between the groups become more apparent. It is observed that the non-channelled (NC) reference sample reaches a higher limit energy level, while the channelled samples stabilise at lower and closer limit values. This finding indicates that the channel geometry can affect the total absorbed energy during the impact and the final level of energy absorption without significantly altering the peak load level.

4.8. Damage Characterization and Failure Mechanisms

In order to interpret the test results presented in the previous sections more accurately, it is necessary to examine the damage that occurred on the test specimens after the test qualitatively. In this subsection, the damage areas observed on the tensile and compressive surfaces of the specimens following the three-point bending tests are first presented comparatively (Table 4.16). Subsequently, the damage areas formed on the impact surface of the specimens and on the surface opposite the impact surface (around the channel) following the DWI tests are evaluated according to Table 4.17 and Table 4.18 . Thus, the possible effects of microchannel geometry on damage development have been supported by visual findings.

Table 4.16. Observed damage regions on the tensile and compressive surfaces of the bending test specimens

Specimen Code	Damage Areas at the surface which exposure to tension loading	Damage areas at the surface which exposure to compression loading
BT-NC-03		
BT-CC-02		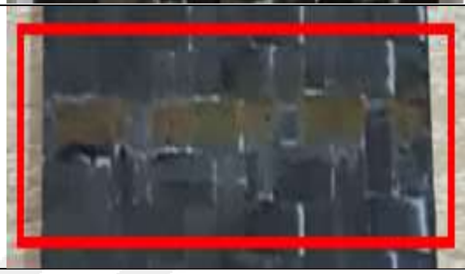
BT-HC-04		
BT-SC-03		
BT-StC-02	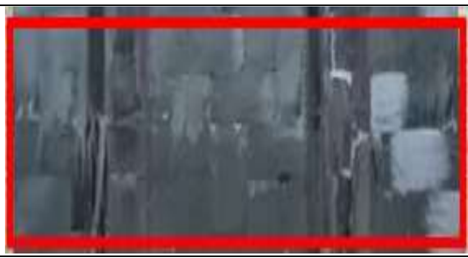	

Table 4.17. Damage areas of the tested reference test specimens on the DWI test

Specimen Code	Damage Areas at the surface which is far from the channels (Impact Surface)	Damage Areas at the surface which is close to the channels
IT-NC-05		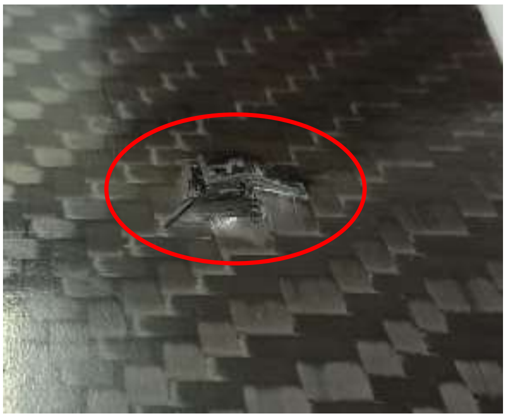
IT-CC-02	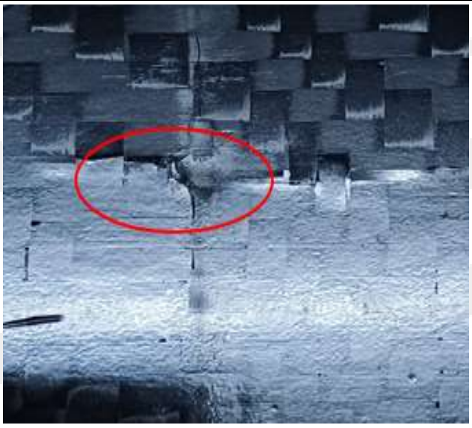	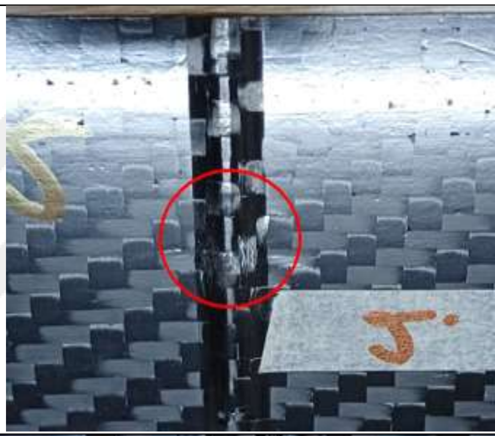
IT-HC-02		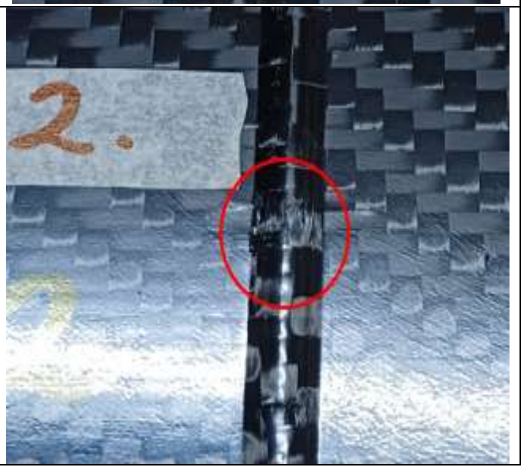

Table 4.18. (Continued) Damage areas of the tested reference test specimens on the DWI test

Specimen Code	**Damage Areas at the surface which is far from the channels (Impact Surface)**	**Damage Areas at the surface which is close to the channels**
IT-SC-02		
IT-StC-04		

The damage zones observed in the bending specimens after testing exhibit a damage progression character consistent with the load-deflection curves obtained for each test group. During the three-point bending test, compressive stresses develop on the upper surface (beneath the loading nose), while tensile stresses develop on the lower surface. In this study, the microchannels are positioned along the longitudinal direction of the sample and close to the tensile surface. In circular channel (CC) specimens, delamination and matrix cracks were observed around the channel on the surface exposed to tensile force; however, no significant fiber breakage/fracture was detected. In samples with other channel geometries (hexagonal, square, star), more pronounced fiber breakage was observed on the surface exposed to tensile force, in addition to delamination and matrix cracks around the channel. It is considered that this difference may be related to the channel geometry altering the magnitude and distribution of stress concentrations around the channel and, consequently, the damage mechanism (particularly fiber damage) developing earlier or more distinctly. On the surfaces of the specimens exposed to compressive loads, delamination, matrix cracks and fiber breakage were observed to exhibit a similar damage mechanism independent of the channel geometry. Furthermore, similar fiber breaks were observed on both sides of the non-channelled samples.

When examining the damage to the samples subjected to impact testing, no significant difference was found between the damage areas formed on the surface where the impact tip made contact in the channelled samples. When examining the surface opposite the impact surface of the channelled samples, it was observed that the damage did not extend to this surface and did not cause any significant distortion in the channel geometry. In contrast, in non-channelled (NC) samples, distinct damage marks have formed on both surfaces of the samples. In samples with channels, it is noteworthy that the damage remains more limited, especially on the surface where the channels are located, and this finding is consistent with the results reported in the literature. Kousourakis et al. (Kousourakis et al., 2006) reported that as the channel diameter increases, the damaged area decreases and that the channels within the structure reduce the spread of damage by blunting or diverting the damage/crack propagation paths. In this study, it is also assessed that the discontinuities created by the channels blunt the crack tips advancing within the material and, as a result, significantly limit the damage observed on the opposite side of the impact surface, on the channel line/in areas close to the channel.

5. CONCLUSION

In this master's thesis study, the mechanical response of CFRP laminates containing microchannels with circular, square, hexagonal, and star cross-sectional geometries, as well as non-channelled (NC) reference laminates, was experimentally investigated under three-point bending (ASTM D790) and low-velocity drop weight impact (ASTM D7136) loads. The main objective of this study is to determine the effect of microchannel cross-sectional geometry on load-carrying capacity, rigidity, cross-sectional efficiency, and damage initiation and propagation behaviour (especially under impact load) within a measurable and comparable experimental framework through direct comparisons with NC reference specimens.

In order to properly evaluate the effect of geometry, the test specimens were produced based on a single material system and laminate architecture. CFRP laminates were prepared using 400 g/m² twill-woven carbon fabric and the MGS LR160/LH160 epoxy system (100:25 by weight) in a 10-layer, symmetrical $[(0/90)]_{5s}$ stacking sequence. In the comparison, only the microchannel cross-sectional geometry was altered, while the layer sequence, resin system, channel position and curing conditions were kept constant. MDF moulds special for the geometry were used to integrate the monofilament geometry into the laminate at the targeted position and in the desired geometric form; the curing process was carried out at 60 °C for 4 hours, applying hot press at an effective pressure of approximately 3 bar on the laminate. A total of 50 samples were produced and tested in accordance with ASTM D790 and ASTM D7136 standards. In this regard, the effect of the channel cross-section geometry on bending and impact response has been analysed through comparisons between different cross-section geometries and comparisons with the non-channelled (NC) reference group. The findings obtained within this framework are presented in the following subheadings as bending and impact results; the effect of the channel cross-section geometry has been comprehensively evaluated in terms of cross-section efficiency and damage behaviour.

Three-Point Bending Test (ASTM D790)

Three-point bending tests were performed in accordance with ASTM D790 standard and the results which obtained were analysed. To make intergroup comparisons more understandable, specimens giving the closest mechanical response to the group mean in each test group were selected as representative (reference) specimens, and comparisons were presented using these specimens. The cross-sectional geometry of the representative samples was obtained using a coordinate measuring machine (CMM); the relevant cross-sectional properties (e.g. cross-sectional area, second moment of area, etc.) were calculated using these geometric data with the CATIA V5 R20 programme. The effect of microchannel cross-section geometry on bending behaviour has been evaluated in terms of elastic region response (initial stiffness), maximum load-carrying capacity (F_{max}), modulus of elasticity (E_f), cross-section efficiency, and deformation characteristics after peak load. In this context, stiffness is represented by the slope (m) obtained from the elastic region of the load–deflection curve and the equivalent bending stiffness (S_B) derived from this slope. In the comparison of section efficiency, the bending shape factor defined by assuming $\Psi_B^E = 1$ for the non-channelled (NC) reference was used.

The overall effect of microchannel integration: Under the production conditions applied in this study, it was observed that microchannel integration did not have a significant negative effect on the bending performance of CFRP laminates. In addition, differences related to the channel cross-section geometry showed significant variations, particularly in terms of stiffness/cross-section efficiency indicators (m, S_B and Ψ_B^E), bending modulus (E_f) and deformation capacity after maximum load ($\Delta\delta$).

Circular Channelled (CC) Cross-Section: It has emerged as the geometry that provides the most balanced bending response. It results in less distortion in the fiber architecture, a more stable response in the elastic region, and high cross-section efficiency. Therefore, CC demonstrated the highest performance in terms of cross-sectional efficiency and equivalent stiffness ($\Psi_B^E = 1.680$; S_B highest group). Furthermore, the highest value in terms of elastic region slope was obtained in the CC group (m = 87.38 N/mm). CC also gave the highest value in terms of flexural modulus (E_f = 78.26 GPa).

Square Channelled (SC) Cross-Section: While demonstrating strong performance in terms of stiffness/cross-section efficiency ($\Psi_B^E = 1.537$), the distinctly limited post-peak load deformation range ($\Delta\delta$ = 2.29 mm) indicates a tendency towards more brittle/sudden fracture. Therefore, although the SC (Square Channelled) group has a satisfactory load-carrying capacity, it exhibits a more limited deformation capacity in terms of post-peak load behaviour and should be carefully evaluated in terms of damage tolerance. In terms of the flexural modulus, SC remains at a slightly lower level than NC (E_f = 69.19 GPa).

Hexagonal Channelled (HC) Cross-Section: The cross-sectional efficiency has remained at a moderate level ($\Psi_B^E = 1.418$). However, it exhibited a more ductile fracture behaviour by demonstrating the highest amount of post-peak load deformation capacity ($\Delta\delta$ = 8.192 mm). This finding suggests that damage can progress more gradually in the HC section and deformation tolerance after fracture can be higher. In terms of elastic region slope (m), HC (Hexagonal Channelled) has reached a value very close to CC (Circular Channelled) (m = 86.69 N/mm). However, the flexural modulus remained at a lower level in the HC group (E_f = 61.213 GPa).

Star Channelled (StC) Section: This complex geometry has further affected the fiber architecture and resulted in lower performance in terms of cross-sectional efficiency ($\Psi_B^E = 1.337$). Furthermore, the fact that the cross-sectional area of the star channel is significantly smaller than other geometries requires that the effect of the channel area be taken into account alongside the "geometry effect" in direct comparisons. The deformation capacity after peak load remains at an intermediate level ($\Delta\delta$ = 4.372 mm). In terms of elastic region slope, StC (Star Channelled) reference test specimen has shown a relatively high value within angular geometries (m = 84.83 N/mm). The flexural modulus is similar to that of HC (E_f = 62.134 GPa), indicating that flexural modulus values can remain at lower levels in complex cross-section geometries.

Overall assessment: The ranking based on Ψ_B^E values representing cross-sectional efficiency was obtained as CC (1.680) > SC (1.537) > HC (1.418) > StC (1.337) > NC (1.0). Equivalent bending stiffness (SB) values also confirmed the same trend; CC (259.687) > SC (237.610) > HC (219.178) > StC (206.642) > NC (154.507) ($\times 10^5$ N·mm²). The initial stiffness ranking in terms of elastic region slope (m) is CC (87.38) ≈ HC (86.69) > StC (84.83) > SC (70.71) > NC (59.39) (N/mm). The ranking in terms of flexural modulus (E_f) was found to be CC (78.263) > NC (71.697) > SC (69.190) > StC (62.134) > HC (61.213) (GPa). In terms of post-peak deformation capacity (Δδ), the following order was obtained: HC (8.192) > NC (6.673) ≈ CC (6.640) > StC (4.372) > SC (2.292); this result supports the idea that the square section exhibits a more brittle post-peak behavior, while the hexagonal section exhibits a more ductile post-peak behaviour.

Low-Velocity Drop Weight Impact (DWI) Test (ASTM D7136)

Low velocity drop weight impact tests (DWI) were conducted in accordance with ASTM D7136 standard at an impact energy of 30 J, and the results were analysed using Load–Time, Energy–Time and Load–Displacement curves, as well as numerical summary parameters. To facilitate intergroup comparisons, the specimens that provided the response closest to the group average in each test group were selected as representative (reference) specimens.

The general character of the impact test: It was observed that in all groups, the load rapidly increased in the first milliseconds to reach a peak value and then decreased during contact to approach zero; the energy–time curves approached a limit value at the end of contact. This limit value represents the total energy absorbed by the specimen.

Peak load (F_{max}) assessment: Average peak load values were similar across groups, and the ranking obtained was NC (1133.31) > StC (1117.55) ≈ HC (1117.01) > CC (1113.51) > SC (1110.44) (N). This finding indicates that the channel cross-section geometry has a limited effect on the peak load level.

Evaluation of absorbed energy quantities: The average absorbed energy values showed more pronounced differences depending on the geometry, and the ranking was found to be NC (23.93) > StC (21.57) ≈ HC (21.53) > CC (21.32) > SC (21.14) (J). The fact that the energy values absorbed in channelled groups occur at lower levels compared to NC indicates that channel integration can affect the total energy absorption capacity under impact.

Post-peak behaviour (Load–Displacement curves): Reference load–displacement curves revealed that all configurations reached similar peak load levels; however, in the post-peak region, the channelled reference specimens exhibited a lower load-carrying tendency compared to the NC (Non-Channelled). It was observed that this difference was particularly pronounced in the SC

(Square Channelled) and StC (Star Channelled) sections, while the CC (Circular Channelled) section exhibited the closest response to NC.

Damage characterisation: In this study, it was reported that while the damage areas formed on the surface contacted by the impact tip (surface which far from channels) in the channelled samples were similar in character, the damage was more limited on the opposite side of the impact surface (on the surface close to the channel line) and no significant distortion occurred in the channel geometry. In NC (Non-Channelled) specimens, more pronounced damage traces were observed on both surfaces. This situation suggests that the discontinuities created by the microchannel divert or blunt the crack/damage propagation paths, thereby reducing the spread of damage along the thickness to a certain extent.

Engineering Conclusions

From an engineering applications perspective, the results obtained from this study provide important guidance for selecting channel cross-sections in the design of smart/multi-functional composite structures. In designs where mechanical performance is paramount, the safest and most balanced option is a circular channel cross-section. For larger flow areas or special functional requirements, square or hexagonal cross-sections may be considered; however, in this case, the effects of sharp corner-induced stress concentration and loss of rigidity must be taken into account in the design. While complex cross-sections, such as star, can offer the advantage of increasing the functional surface area, they are more risky in terms of structural integrity.

When targeting similar channel cross-sectional areas (flow areas), one of the fundamental differences between geometries is the amount of surface area in contact with the fluid (flow surface). Although the circular cross-section tends to offer a lower flow surface within the same flow area, its cornerless structure limits stress concentrations by causing less disruption to the fiber architecture; it therefore stands out as the most mechanically secure and balanced option. In contrast, angular cross-sections such as square and hexagon may offer potential advantages in terms of heat transfer/multifunctionality by providing a higher flow surface within the same flow section area; however, the risk of loss of rigidity and reduced damage tolerance due to stress concentrations that may occur in the corner regions must be considered in the design. Star-shaped, complex cross-sections may further increase the flow-contact surface area; however, due to the effects of multiple/sharp corners, their suitability may be more limited in designs where structural performance is prioritized.

__Future Studies__

- The effect of changing the size and location of the channels on the bending behavior can be investigated.
- Experimental studies can be conducted to evaluate the mechanical-functional balance for the targeted functions of microchannels (e.g., thermal management via fluid circulation, transport of self-healing agents).
- The effects of local reinforcement on stiffness and F_{max} can be evaluated by applying a small additional layer to the area surrounding the channel along its length and comparing reinforced and unreinforced specimens.
- The effect of using special monofilament with fillets (rounded corners) for square and star channels to reduce the corner effect on the onset of damage can be examined.
- The delamination propagation area, damage growth tendency and penetration limits can be examined using different impact energies (e.g. increasing energy levels) without being restricted to a single energy level.

  In order to identify the damaged area and delamination more reliably, damage mapping studies can be carried out using non-destructive testing methods such as ultrasonic C-scan/thermography.

6. REFERENCES

Abrate, S. (2001). Modeling of impacts on composite structures. *Composite Structures, 51*(2), 129-138. doi:10.1016/s0263-8223(00)00138-0

Ahmed, H. E., & Ahmed, M. I. (2015). Optimum thermal design of triangular, trapezoidal and rectangular grooved microchannel heat sinks. *International Communications in Heat and Mass Transfer, 66*, 47-57. doi:10.1016/j.icheatmasstransfer.2015.05.009

An, Z., Cheng, X., Ma, Y., Zhao, D., Guo, X., & Cheng, Y. (2025). Low-velocity impact performances of CFRP laminates containing 3D microvascular channels. *International Journal of Impact Engineering, 202*, 105308. doi:10.1016/j.ijimpeng.2025.105308

Ashby, M. F. (1997). Material property charts *Materials Selection and Design* (pp. 266-280): ASM international.

Bakis, C. E., Bank, L. C., Brown, V., Cosenza, E., Davalos, J., Lesko, J., . . . Triantafillou, T. (2002). Fiber-reinforced polymer composites for construction—State-of-the-art review. *Journal of composites for construction, 6*(2), 73-87.

Balasubramanian, M. (2014). *Composite Materials and Processing*: Taylor & Francis Group.

Barbero, E., & GangaRao, H. (2005). APPLICATIONS OF COMPOSITES IN.

Bhong, M., Khan, T. K. H., Devade, K., Vijay Krishna, B., Sura, S., Eftikhaar, H. K., . . . Gupta, N. (2023). Review of composite materials and applications. *Materials Today: Proceedings*. doi:10.1016/j.matpr.2023.10.026

Biron, M. (2007). *Thermoplastics and thermoplastic composites: technical information for plastics users*: Elsevier.

Blaiszik, B. J., Kramer, S. L. B., Olugebefola, S. C., Moore, J. S., Sottos, N. R., & White, S. R. (2010). Self-Healing Polymers and Composites. *Annual Review of Materials Research, 40*(1), 179-211. doi:10.1146/annurev-matsci-070909-104532

Chen, J., Yu, Z., & Jin, H. (2022). Nondestructive testing and evaluation techniques of defects in fiber-reinforced polymer composites: A review. *Frontiers in Materials, 9*, 986645.

Chung, D. D. (2002). Composites get smart. *Materials today, 5*(1), 30-35.

Clyne, T. W., & Hull, D. (2019). *An introduction to composite materials*: Cambridge university press.

Cole, J. (2020). <Active Thermal Management in FRP
Composites via Embedded Vascular
Networks>.

Dixit, T., & Ghosh, I. (2015). Review of micro- and mini-channel heat sinks and heat exchangers for single phase fluids. *Renewable and Sustainable Energy Reviews, 41*, 1298-1311. doi:10.1016/j.rser.2014.09.024

Dry, C. (1996). Procedures developed for self-repair of polymer matrix composite materials. *Composite Structures, 35*(3), 263-269.

Dry, C. M., & Sottos, N. R. (1993). *Passive smart self-repair in polymer matrix composite materials.* Paper presented at the Smart Structures and Materials 1993: Smart Materials.

Elaldi, F. (2005). *An overview for structural health monitoring of composites in aerospace applications.* Paper presented at the Proceedings of 2nd International Conference on Recent Advances in Space Technologies, 2005. RAST 2005.

Ersoy, H., & Malzeme, K. (2001). Literatür yayıncılık: İstanbul.

Ersoy, H. Y. (2001). *Kompozit malzeme*: Literatür Yayınları.

Froes, F. (1994). Advanced metals for aerospace and automotive use. *Materials Science and Engineering: A, 184*(2), 119-133.

Geren N, K. E. (2024). Weaving of filament yarns to form microvascular channels in fiber fabric for fiber reinforced polymer composite production. (Patent No. PCT/TR2023/051362). Türkiye:

Geren N., B. M., Özkan G. M., Uzay Ç., Çetin A., Acer D. C. (2024). Composite Battery Containment Box with Thermal Management and Self-Healing (Repair) (Patent No. PCT/TR2024/050272). Türkiye:

Hart, K. R., Lankford, S. M., Freund, I. A., Patrick, J. F., Krull, B. P., Wetzel, E. D., . . . White, S. R. (2017). Repeated healing of delamination damage in vascular composites by pressurized delivery of reactive agents. *Composites Science and Technology, 151*, 1-9. doi:10.1016/j.compscitech.2017.07.027

Hengeveld, D. W., Mathison, M. M., Braun, J. E., Groll, E. A., & Williams, A. D. (2011). Review of Modern Spacecraft Thermal Control Technologies. *HVAC&R Research, 16*(2), 189-220. doi:10.1080/10789669.2010.10390900

Hull, D. (1998). An Introduction to Composite Materials.

Hull D, S. Y. (1993). <Damage mechanism characterization in composite damage tolerance investigations.pdf>.

Hung, J.-C., Chang, D.-H., & Chuang, Y. (2012). The fabrication of high-aspect-ratio micro-flow channels on metallic bipolar plates using die-sinking micro-electrical discharge machining. *Journal of Power Sources, 198*, 158-163. doi:10.1016/j.jpowsour.2011.09.065

International, A. (2015). *Standard Test Methods for Flexural Properties of Unreinforced and Reinforced Plastics and Electrical Insulating Materials* (ASTM D790–15). Retrieved from West Conshohocken, PA, United States:

International, A. (2020). *Standard Test Method for Measuring the Damage Resistance of a Fiber-Reinforced Polymer Matrix Composite to a Drop-Weight Impact Event* (ASTM-D7136-D7136M-20). Retrieved from West Conshohocken, PA, United States:

Johnson, R. W., Evans, J. L., Jacobsen, P., Thompson, J. R. R., & Christopher, M. (2004). The Changing Automotive Environment: High-Temperature Electronics. *IEEE Transactions on Electronics Packaging Manufacturing, 27*(3), 164-176. doi:10.1109/tepm.2004.843109

Karbhari, V. M. (2007). Introduction: The use of composites in civil structural applications *Durability of composites for civil structural applications* (pp. 1-10): Elsevier.

Kharabati, S., & Saedodin, S. (2024). A systematic review of thermal management techniques for electric vehicle batteries. *Journal of Energy Storage, 75*, 109586.

Koştur, E., Geren, N., & Demirel, M. Ö. (2025). Novel microvascular channel method for developing self-healing functions of composite structures. *Composites Part A: Applied Science and Manufacturing*, 109226.

Kousourakis, A., Mouritz, A. P., & Bannister, M. K. (2006). Interlaminar properties of polymer laminates containing internal sensor cavities. *Composite Structures, 75*(1-4), 610-618. doi:10.1016/j.compstruct.2006.04.086

Lewis, J. A. (2006). Direct Ink Writing of 3D Functional Materials. *Advanced Functional Materials, 16*(17), 2193-2204. doi:10.1002/adfm.200600434

Lima, M. S. F., Sakamoto, J. M. S., Simoes, J. G. A., & Riva, R. (2013). Laser Processing of Carbon Fiber Reinforced Polymer Composite for Optical Fiber Guidelines. *Physics Procedia, 41*, 572-580. doi:10.1016/j.phpro.2013.03.118

Livingston, R., & Koohbor, B. (2022). Characterizing fiber-matrix debond and fiber interaction mechanisms by full-field measurements. *Composites Part C: Open Access, 7*, 100229.

Mangalgiri, P. (1999). Composite materials for aerospace applications. *Bulletin of Materials Science, 22*(3), 657-664.

McCombe, G. P., Rouse, J., Trask, R. S., Withers, P. J., & Bond, I. P. (2012). X-ray damage characterisation in self-healing fibre reinforced polymers. *Composites Part A: Applied Science and Manufacturing, 43*(4), 613-620. doi:10.1016/j.compositesa.2011.12.020

Meese, E. A., & Nørstrud, H. (2001). <Simulation of convective heat flux and heat penetration for a spacecraft at re-entry>.

Meetham, G. (1991). High-temperature materials—a general review. *journal of Materials Science, 26*(4), 853-860.

N., G. (2024). Production Method of Self-Repairing, Polymer Matrix, Fibre Reinforced Composite Pressure Vessel/Tank and Wind Turbine Blades (Patent No. PCT/TR2024/050885). Türkiye:

Nanni, A. (1993). Flexural behavior and design of RC members using FRP reinforcement. *Journal of structural engineering, 119*(11), 3344-3359.

Niu, M. C.-Y., & CHUN, Y. (1988). Airframe structural design–Practical design information and data on aircrafts structures. *Aufl. Hong Kong: Conmilit Pr*.

Pang, J. W. C., & Bond, I. P. (2005). 'Bleeding composites'—damage detection and self-repair using a biomimetic approach. *Composites Part A: Applied Science and Manufacturing, 36*(2), 183-188. doi:10.1016/s1359-835x(04)00166-6

Patrick, J. F., Hart, K. R., Krull, B. P., Diesendruck, C. E., Moore, J. S., White, S. R., & Sottos, N. R. (2014). Continuous self-healing life cycle in vascularized structural composites. *Adv Mater, 26*(25), 4302-4308. doi:10.1002/adma.201400248

Pety, S. J., , P. X. L. C., , S. M. C. a., & White, S. R. (2017). <Active cooling of microvascular composites>. doi:10.1088/1361-665X/aa84e7

Pety, S. J., Tan, M. H. Y., Najafi, A. R., Barnett, P. R., Geubelle, P. H., & White, S. R. (2017). Carbon fiber composites with 2D microvascular networks for battery cooling. *International Journal of Heat and Mass Transfer, 115*, 513-522.

Phillips, D. M., Ryan Pierce, M., & Baur, J. W. (2011). Mechanical and thermal analysis of microvascular networks in structural composite panels. *Composites Part A: Applied Science and Manufacturing, 42*(11), 1609-1619. doi:10.1016/j.compositesa.2011.07.008

Quilter, A. (2001). Composites in aerospace applications. *IHS White Paper, 444*(1), 264.

Richardson, M. O. W., & Wisheart, M. J. (1996). Review of low-velocity impact properties of composite materials. *Composites Part A: Applied Science and Manufacturing, 27*(12), 1123-1131. doi:10.1016/1359-835x(96)00074-7

Saadatmanesh, H. (1994). Fiber composites for new and existing structures. *Structural Journal, 91*(3), 346-354.

Saeed, M.-U., Chen, Z., & Li, B. (2015). Manufacturing strategies for microvascular polymeric composites: A review. *Composites Part A: Applied Science and Manufacturing, 78*, 327-340. doi:10.1016/j.compositesa.2015.08.028

Safri, S. N. A. B., Sultan, M., & Jawaid, M. (2019). Damage analysis of glass fiber reinforced composites *Durability and life prediction in biocomposites, fibre-reinforced composites and hybrid composites* (pp. 133-147): Elsevier.

Scwartz, M. (1997). Composite Materials: Properties, non destructive testing and repair, polymer, ceramic, metal matrices: Prentice Hall Inc, USA.

Siddique, A. R. M., Mahmud, S., & Van Heyst, B. (2018). A comprehensive review on a passive (phase change materials) and an active (thermoelectric cooler) battery thermal management system and their limitations. *Journal of Power Sources, 401*, 224-237.

Sonsino, C., & Moosbrugger, E. (2008). Fatigue design of highly loaded short-glass-fibre reinforced polyamide parts in engine compartments. *International Journal of Fatigue, 30*(7), 1279-1288. doi:10.1016/j.ijfatigue.2007.08.017

Soutis, C. (2005). Fibre reinforced composites in aircraft construction. *Progress in aerospace sciences, 41*(2), 143-151.

Sönmez, M., & Şatır, S. (2009). Polimer Matrisli Kompozitlerin Endüstri Ürünleri Tasarımında Önemi ve Geleceği: Türkiye'den Dört Örnek Firma Üzerine Bir İnceleme, 502041960. *Fen Bilimleri Enstitüsü, İstanbul Teknik Üniversitesi, İstanbul*.

Swait, T. J., Rauf, A., Grainger, R., Bailey, P. B. S., Lafferty, A. D., Fleet, E. J., . . . Hayes, S. A. (2013). Smart composite materials for self-sensing and self-healing. *Plastics, Rubber and Composites, 41*(4-5), 215-224. doi:10.1179/1743289811y.0000000039

Şahin, Y. (2000). *Kompozit malzemelere giriş*: Gazi Kitabevi.

Therriault, D., White, S. R., & Lewis, J. A. (2003). Chaotic mixing in three-dimensional microvascular networks fabricated by direct-write assembly. *Nat Mater, 2*(4), 265-271. doi:10.1038/nmat863

Therriault, D., White, S. R., & Lewis, J. A. (2003). Chaotic mixing in three-dimensional microvascular networks fabricated by direct-write assembly. *Nature materials, 2*(4), 265-271.

Trask, R., & Bond, I. (2010). Bioinspired engineering study of Plantae vascules for self-healing composite structures. *Journal of The Royal Society Interface, 7*(47), 921-931.

Trask, R. S., Williams, G. J., & Bond, I. P. (2006). Bioinspired self-healing of advanced composite structures using hollow glass fibres. *Journal of The Royal Society Interface, 4*(13), 363-371. doi:10.1098/rsif.2006.0194

Van Den Einde, L., Zhao, L., & Seible, F. (2003). Use of FRP composites in civil structural applications. *Construction and Building Materials, 17*(6-7), 389-403. doi:10.1016/s0950-0618(03)00040-0

Vieille, B., Casado, V. M., & Bouvet, C. (2013). About the impact behavior of woven-ply carbon fiber-reinforced thermoplastic-and thermosetting-composites: a comparative study. *Composite Structures, 101*, 9-21.

Wang, Y., Pham, D. T., Ji, C., & Harkin-Jones, E. (2015). Self-healing composites: A review. *Cogent Engineering, 2*(1), 1075686. doi:10.1080/23311916.2015.1075686

White, S. R., Sottos, N. R., Moore, J. S., Lewis, J. A., Geubelle, P. H., Freund, J. S., . . . URBANA-CHAMPAIGN, I. U. A. (2006). Microvascular autonomic composites. *MURI annual report, AFOSR Grant# FA9550-05-1-0346*.

William D. Callister, J., David G. Rethwish. (2018). *Materials Science and Engineering* (10 ed.).

Williams, G., Trask, R., & Bond, I. (2007). A self-healing carbon fibre reinforced polymer for aerospace applications. *Composites Part A: Applied Science and Manufacturing, 38*(6), 1525-1532. doi:10.1016/j.compositesa.2007.01.013

Williams, H. R., Trask, R., & Bond, I. (2007). Self-healing composite sandwich structures. *Smart Materials and Structures, 16*(4), 1198.

Williams, H. R., Trask, R. S., & Bond, I. P. (2007). Self-healing composite sandwich structures. *Smart Materials and Structures, 16*(4), 1198-1207. doi:10.1088/0964-1726/16/4/031

Woias, P., Andrews, J. R., Papautsky, I., & Gerner, B. (2004). Laser processes for prototyping and production of novel microfluidic structures. *5345*, 147. doi:10.1117/12.524547

Zhao, N., Wang, Z., Cai, C., Shen, H., Liang, F., Wang, D., . . . Xu, J. (2014). Bioinspired materials: from low to high dimensional structure. *Adv Mater*, *26*(41), 6994-7017. doi:10.1002/adma.201401718

CURRICULUM VITAE

Oğuzhan TÜRKGENÇ. degree in Mechanical Engineering from Çukurova University (2017–2022) with a GPA of 2.46/4.00. From July to October 2023, he worked as a Production Engineer at Üçgül Machine, participating in steel-structure manufacturing and assembly processes. Between July 2024 and August 2025, he worked at Ateks Engineering on production planning, assembly control, and production tracking activities. Since March 2023, he has pursued an M.Sc. degree at Çukurova University; he prepared his thesis entitled "Determination of Impact and Flexural Behaviours of Carbon Fiber Reinforced Composites with Various Micro Channel Section Geometries" and defended it on 25 December 2025.